

FLOW CHARACTERIZATION OF COMPRESSIBLE PARTICULATE BIOMASS MATERIALS

A Dissertation
Presented to
The Academic Faculty

By

Yimin Lu

In Partial Fulfillment
of the Requirements for the Degree
Doctor of Philosophy in the
School of Civil and Environmental Engineering

Georgia Institute of Technology

Nov 2022

© Yimin Lu 2022

FLOW CHARACTERIZATION OF COMPRESSIBLE PARTICULATE BIOMASS MATERIALS

Thesis committee:

Dr. Alexander Alexeev
George W. Woodruff School of Mechanical Engineering
Georgia Institute of Technology

Dr. J. David Frost
School of Civil and Environmental Engineering
Georgia Institute of Technology

Dr. Susan E. Burns
School of Civil and Environmental Engineering
Georgia Institute of Technology

Dr. Wencheng Jin
Energy and Environment Science and Technology Directorate
Idaho National Laboratory

Dr. Sheng Dai, Advisor
School of Civil and Environmental Engineering
Georgia Institute of Technology

Dr. Jorge Macedo
School of Civil and Environmental Engineering
Georgia Institute of Technology

Date approved: December 12, 2022

ACKNOWLEDGMENTS

I would like to express my sincere appreciation to my advisor, Dr. Sheng Dai, for his guidance, patience, encouragement, and continuous support through my journey at the Georgia Institute of Technology. It is a great privilege to spend the years learning from such an extraordinary scientist full of knowledge, passion, curiosity, and dedication. What I learned is far more than doing research, but also the way of thinking, viewing, doing, and the attitude of work and life. I feel lucky to be one of his graduate students.

I would also like to appreciate my thesis committee members, Dr. Alexander Alexeev, Dr. Susan Burns, Dr. David Frost, and Dr. Jorge Macedo, for their insightful comments on my Ph.D. study, illuminating guidance on academic learning, and helpful suggestions on career development. Special thanks to Dr. Wencheng Jin, for his guidance of every detailed numerical schemes, generous support of my learning of biomass modeling, and valuable mentoring on research and career development. In addition, I would like to take this opportunity to thank all other Geosystems faculty members, Dr. Chloe Arson, Dr. Haiying Huang, Dr. Paul Mayne, for their help in both academic learning and life.

This thesis could not be completed without the help and experimental support from Dr. Jordan Klinger, Dr. Yidong Xia, and Dr. Nepu Saha from the Idaho National Laboratory. I would also like to thank Dr. Douglas Cortes from New Mexico State University for his help and encouragement during my early Ph.D. study. Acknowledgements will also be given to my former advisors Dr. Junwu Xia and Dr. Hongfei Chang from the China University of Mining and Technology, for their advice and encouragement during my Ph.D. study.

Moreover, I would like to thank all the members of the Subsurface Processes Laboratory, Jongchan Kim, Wilson Espinoza, Boyoung Jeong, Yumeng Zhao, Imgenur Tepcik, Savannah Howard, Abdallah Ikbarieh, and Aryong Yun, as well as visiting scholars Zhichao Liu, Guangyao Li, Daxin Geng, Lele Liu, Liuxiang Zhang, Haitao Zhang, Jiazuo Zhou, Bozhi Deng, Zhilin Cheng, Feng Zhu, and Dong Hun Kang. I am grateful for your

help, encouragement, discussions, and joyful moments we shared. Additionally, I would like to thank all my colleagues and friends in the Geotechnical Society for the lovely days we spent together.

Last but not least, I am greatly indebted to my parents, Binghua Lu and Ling Jiang, and my wife, Beili Li, for your unceasing love and daily encouragement. I could never complete this work without your endless support.

TABLE OF CONTENTS

Acknowledgments	iii
List of Tables	x
List of Figures	xi
Chapter 1: Introduction	1
1.1 Motivation	1
1.2 Thesis Organization	2
Chapter 2: Flow characterization and modeling using multiscale experiments and a hypoplastic model	4
2.1 Introduction	4
2.2 Gudehus-Bauer hypoplastic model	7
2.2.1 Model outline	7
2.2.2 Model implementation and validation	9
2.3 Material parameters calibration	11
2.3.1 Loblolly pine samples	11
2.3.2 Parameters determined from physical measurements	12
2.3.3 Modeling assisted calibration	15
2.3.4 Discussion on the material parameters	20

2.4	Flowability in quasi-static regime	21
2.4.1	Customized axial shear test	22
2.4.2	Physical experiments	23
2.4.3	Numerical model setup and results	24
2.4.4	Discussion on particle stiffness	28
2.5	Flowability in dense regime	29
2.5.1	Numerical modeling and validation	29
2.5.2	Effects of outlet size and wall friction	32
2.6	Conclusions	34
Chapter 3: Flow and arching in Wedge-shaped Hoppers		36
3.1	Introduction	36
3.2	Methods	39
3.2.1	Granular pine samples	39
3.2.2	Experimental setup	39
3.2.3	Numerical modeling	40
3.2.4	Model validation	43
3.3	Results	44
3.3.1	Flow response	44
3.3.2	Arching	45
3.4	Analyses and discussion	47
3.4.1	Hopper outlet width	47
3.4.2	Hopper inclination	47

3.4.3	Initial packing	50
3.4.4	Particle density variability	52
3.4.5	Surcharge	54
3.5	Conclusions	57
Chapter 4: Wedge-shaped hopper design for milled woody biomass flow		59
4.1	Introduction	59
4.2	Methods	61
4.2.1	Woody granular biomass materials	61
4.2.2	Experimental setup	62
4.2.3	Numerical modeling and validation	63
4.3	Results & Discussion	65
4.3.1	Flow patterns	65
4.3.2	Arching	71
4.3.3	Flow throughput prediction	73
4.3.4	Design guide	76
4.4	Conclusions	77
Chapter 5: Characterization and modeling on the multi-regime flow behavior		79
5.1	Introduction	79
5.2	Methods	81
5.2.1	Inclined plane experiment	81
5.2.2	Numerical modeling	82
5.2.3	Constitutive models	85

5.3	Multi-regime flow behavior	90
5.3.1	Typical flow response	90
5.3.2	DP- $\mu(I)$ model calibration and validation	91
5.3.3	Model comparison	93
5.3.4	Flow profile	94
5.3.5	Scaling law	96
5.3.6	Limitations of DP- $\mu(I)$ model	98
5.4	Conclusions	99
Chapter 6: Effects of moisture content on flow behavior		101
6.1	Introduction	101
6.2	Methods	102
6.2.1	Biomass sample	102
6.2.2	Experimental methods and setups	103
6.3	Results	104
6.3.1	Fiber saturation point	104
6.3.2	Compressibility	106
6.3.3	Static friction	106
6.4	Analyses and discussion	108
6.4.1	Particle swelling	108
6.4.2	Flow behavior in wedge-shaped hoppers	109
6.5	Conclusions	114
Chapter 7: Conclusions and future work		115

7.1	Conclusions	115
7.2	Future work	118
	References	120

LIST OF TABLES

2.1	Fomulation of G-B hypoplastic model.	8
2.2	G-B model parameters of Karlsruhe sand used for the oedometer test simulations	10
2.3	Calibrated G-B-hypoplastic model parameters for the two pine samples. . .	21
3.1	G-B-hypoplastic model parameters for the pine samples with different particle density.	53
4.1	Mean particle size and internal friction angle of the woody biomass samples.	75
5.1	Fomulation of DP- $\mu(I)$ model.	87
5.2	Calibrated DP- $\mu(I)$ model parameters for the loblolly pine sample.	89
6.1	Calibrated G-B-hypoplastic model parameters of pine chips at different moisture contents.	110

LIST OF FIGURES

2.1	Comparison between numerical predictions and experimental measurements [46] of oedometer tests.	11
2.2	(a) The particle size distribution of two investigated samples with the corresponding photographs demonstrating particle morphology. The blue dashed line is extrapolated due to the limitation of the particle size characterization using the sieving method. (b) Semi-logarithmic relation between void ratio e and mean stress p of the two samples as measured using oedometer tests. Three replicate oedometer tests were performed for each sample, then h_s and n were calculated from Equation 2.3 and averaged. Moreover, different pairs of points on the $e - \ln(p)$ curve are used to calculate h_s and n . The variations caused by different tests and different pairs of points on the $e - \ln(p)$ curve are found negligible.	13
2.3	The obtained relation of minimum void ratio e_{min} with applied compression σ_v from vibration test.	14
2.4	Numerical calibration process to determine the exponent β : (1) simulation of a suite of oedometer tests using a single axial symmetrical element model (a) with different input β ; (2) calibration of β by finding the best match of bulk density ρ_b evolution under different level of compression σ_v between numerical prediction and experimental measurements using least-square method (b).	16
2.5	Shear behavior from the Schulze ring shear test. (a) A typical shear response where numerical (green dashed line) and experimental (blue line) shear stress τ , as well as experimental bulk density ρ_b (red dot-dashed line) are plotted versus strain $\Delta x/h$ for the <i>as-ground</i> sample. The applied vertical stress σ_v at the pre-shear step and the second step is 10 kPa, and 5 kPa, respectively. The peak shear stress (shear strength) τ_p and critical state shear stress τ_c are obtained. (b-c) The relation of the critical state shear stress τ_c against the normal stress σ_v from the ring shear test for the two samples. The red 'x's are obtained from the experiment. Other dots and lines stand for the numerical results obtained by assuming the Lode angle θ of the ring shear at critical stress state are 10° , 20° and 30° , respectively.	18

2.6	The relation of the peak shear stress τ_p against the vertical pressure σ_v from the ring shear test for the two samples. The red 'x's are experimental data, and the blue circles are numerical predictions using the calibrated α	20
2.7	Geometry and boundary conditions of the axial shear test. (a) A schematic view of the test setup. (b) The boundary condition for the compaction step. (c) The boundary condition for the piston intruder.	22
2.8	Comparison of time-lapse measured force on the intruder for the numerical simulation (lines) and physical experiments (dots). F_i denotes the intruding force and u_y denotes the intruder travel distance. For clarity, Only the data of the <i>as-ground</i> sample with height $H=95$ mm with vertical pressures $\sigma = 0$ and 7.5 kPa are presented. The gray dashed line represents the force of gravity from the material that is directly above the intruder.	24
2.9	Modeling predicted shear zone development for the case of $H = 95$ mm and $\sigma_v = 7.5/0$ kPa. (a,c) Bulk density distribution during the intrusion step with and without pre-loading ($\sigma_v = 7.5$ kPa and $\sigma_v = 0$ kPa, respectively). The shear zones are manifested as local low-density regions. (b,d) Sketch of shear zone migrations for the case with and without pre-loading.	25
2.10	Comparison of peak force on the intruder F_i^p with different pre-loading pressures σ_v for the simulations and the physical measurements for the <i>as-ground</i> sample (a) and the <i>engineered</i> sample (b). H represents the initial sample height before compaction.	27
2.11	(a) Geometry of the wedge-shaped hopper with an upper bin for both the numerical simulation and the physical tests. The outlet size is controlled by sliding the hopper walls. (b) Normalized representative flow rate q_m , bulk density ρ_b , and velocity v profiles along the width of outlet. (c) Comparison of predicted cumulative mass discharged m_t from the G-B model (dot-dashed lines) and the M-C model (dashed lines) against experimental measurements (red 'x's) for $W = 60$ mm and $\mu = 30^\circ$	31
2.12	(a) Comparison of predicted average mass flow rates (blue circles) for different hopper outlet widths W to physical measurements (red 'x's). The dot-dashed lines in red represent $\pm 20\%$ -error boundaries. (b) Predicted average mass flow rate from the numerical model as a function of wall friction angle. Uncertainty bars on the numerical results represent the standard deviation due to a reasonable range of time increment sizes Δt	33
2.13	Predicted flow pattern with wall friction angle $\phi_w = 8.5^\circ$ (a), and with wall friction angle $\phi_w = 30^\circ$ (b).	34

3.1	(a) A biomass material Process Development Unit at Idaho National Laboratory, Idaho Falls, ID, USA. Hoppers are marked out in the yellow boxes. (b) An example of woody biomass material arching in a wedge-shaped hopper.	36
3.2	(a) Particle size distribution of the sample and a photograph presenting particle size and shape. The dashed line is empirically extrapolated due to the lower limit of the sieve screen to measure the particle size. (b) A schematic view of the experimental set-up: a wedge-shaped hopper extended with an upper cuboid bin. The numerical model is constructed using a slice with a finite thickness of 25 mm based on the plane strain condition. (c) The geometry and boundary conditions of the pseudo-3D numerical model. Note the outlet size is adjusted by sliding the hopper walls.	39
3.3	Numerical model validation and predicted flow response for a hopper (low inclination angle) and a silo (high inclination angle). (a) Comparison of simulation predicted cumulative mass discharged m_t against experimental measurements for outlet width $W = 57.7$ mm and hopper inclination $\mu = 24.4^\circ$. (b) Flow pattern demonstration superposed with density distribution for the case in (a). (c-d) Typical flow response of a silo (flat-bottom hopper) with outlet width $W = 70$ mm and inclination $\mu = 90^\circ$	41
3.4	Numerical demonstration of hopper arching. (a) The predicted cumulative mass discharged m_t against time for a hopper with fixed inclination $\mu = 24.4^\circ$ and three outlet width $W = 19, 20, 21$ mm. Free flowing is predicted for $W = 21$ mm while hopper arching is realized for $W = 19, 20$ mm. Note the continuum mechanics-based model cannot model the complete stop of material flow as shown in the small zoomed-in figure, yet, the over one magnitude of difference in predicted flow rate indicates material arching is realized. (b-d) Comparison of the contours of the density (b), the vertical velocity (c), and the normalized friction ratio (d) between the arching hopper case with $W = 19$ mm and the free-flow hopper case with $W = 21$ mm.	46
3.5	Effect of hopper outlet width W on the mass flow rate q_m with hopper inclination angle of (a) 24.4° , (b) 30° and (c) 36° . For each case, the yellow '×'s stand for experimental measurements, the filled diamonds represent numerical predictions, and the dashed line is fitted from numerical results. The filled triangles located on the W -axes W_{cr}^d are the critical outlet widths obtained from the Dichotomy method for each hopper inclination case. . . .	48

3.6	Effect of the hopper inclination angle μ on the mass flow rate q_m and the critical outlet width W_{cr} . (a) The plot of the mass flow rate q_m against the hopper outlet width W at different inclination angle μ . Markers represent experimental measurements, and lines stand for simulation predicted results. Different hopper inclination angles μ are color-coded. (b) The influence of hopper inclination angle μ on the critical outlet width W_{cr} . The green '×'s with error bars are measurements from experiments. The brown '+'s are extrapolated as the intersections of the experiments measured $q_m - W$ fitting lines (Figure 3.6(a)) and the W -axis. The dark circles represent numerically obtained W_{cr} from the Dichotomy method and the extrapolating method, note the two methods obtained W_{cr} are close to each other. The yellow triangles are calculated from the classic Jenike design guide. The axis of inclination angle is in log-scale.	49
3.7	Effect of the initial packing on the mass flow rate q_m and the critical outlet width W_{cr} . (a, c) Predicted cumulative discharged mass m_t versus time t for a slender hopper with $\mu = 30^\circ$ and a flat-bottom hopper with $\mu = 90^\circ$, respectively. (b, d) Predicted critical outlet width W_{cr} at different initial packing conditions ρ_i in the slender hopper and in the flat-bottom hopper.	51
3.8	Effect of particle density variability on flow performance. (a, c) Predicted mass flow rate q_m of pine chips with different particle density against hopper outlet width W for a slender hopper ($\mu = 30^\circ$) and a flat-bottom hopper ($\mu = 90^\circ$). (b, d) The critical outlet width W_{cr} predicted at different particle density ρ_p for hoppers with inclination angle of 30° and 90°	54
3.9	Effect of filling height on the flow response. (a, d) Predicted cumulative discharged mass m_t against time with different initial amount of materials for a slender hopper ($\mu = 24.4^\circ$ and $W = 70$ mm) and a flat-bottom hopper ($\mu = 90^\circ$ and $W = 50$ mm). Two stages of the flow rate (i.e., the slope of the $m_t - t$ response) are observed for the slender hopper (a). Note the case with material mass $M = 22.2$ kg does not have enough material inside the upper bin, only a straight line is predicted for $m_t - t$. (b) The mass flow rate q_m variation with the initial amount of material M obtained from the two stages. (c) Mass flow rate q_m variation against hopper outlet width W for different initial amounts of material and different stages. (e, f) The critical outlet width W_{cr} predicted for the flat-bottom hopper and the slender hopper against the initial filled material mass M	55

4.1	Particle size distribution of the 6 woody biomass samples used in this study with photos showing their size and shape. Note the unit of the ruler is an inch. The left two photos are as-ground and engineered loblolly pine samples, and the right three photos are Douglas fir samples generated from a crumbler with a head of 1, 2, and 4 mm, respectively. Note that the as-ground pine-1 and pine-2 samples originated from the same parent loblolly pine chips, and the difference of particle size distribution results from the biomass material variability.	63
4.2	(a) Experimental setup for the hopper test. A wedge-shaped hopper is equipped with adjustable hopper inclination angle via rotating hand-wheels and outlet width controlled with step motors. The vertical steel plates inside the hopper are to control the length along the axial direction. A cuboid bin can be equipped above the hopper. A scale is placed below the hopper to measure the time-lapse discharged weight. (b) Numerical setup simulating a slice of the hopper-bin system based on the plane strain condition. (c) Validation of the numerical modeling by comparing the numerical prediction of discharge responses (lines) against the experimental measurements (dots) at different hopper outlet width W	64
4.3	(a) Demonstration of the two flow patterns with the color representing velocity magnitude. Mass flow: $\mu = 24.4^\circ$, $\phi_w = 8.5^\circ$, $W = 52$ mm; Funnel flow: $\mu = 45^\circ$, $\phi_w = 30^\circ$, $W = 75$ mm. (b) The distribution of bulk density ρ_b at time $t = 3$ s, 5s, and 10s inside a simulated mass-flow hopper ($\mu = 30^\circ$, $\phi_w = 8.5^\circ$, $W = 60$ mm). Sections with different Mass Flow Index (MFI) are denoted as: A) no-flow zone, B) an arch-shaped layer between flow and no-flow zones, C) flow zone, and D) zone with material at the centerline already discharged. (c) The MFI map for a funnel flow simulation ($\mu = 30^\circ$, $\phi_w = 45^\circ$, $W = 60$ mm). (d) The MFI map for the mass flow simulation shown in (b) with the four MFI regions marked.	67
4.4	(a) Three-dimensional flow pattern design chart with the boundary (gray surface), which represents the MFI equal to 0.3, separating the two flow patterns. The color-coded slice represents the simulated MFI distribution for flowing the <i>as-ground</i> pine sample ($\phi_c = 47.3^\circ$) with different hopper configurations. (b) The two-dimensional MFI contour with a fixed internal friction angle of $\phi_c = 47.3^\circ$ representing the <i>as-ground</i> pine sample.	70
4.5	(a) Time-lapse responses of the cumulative discharged mass m_t with a hopper inclination of $\mu = 24^\circ$. The two hopper cases with $W = 19$ and 20 mm yield arching, while the two cases with $W = 21$ and 42 mm result in flowing. The color-coded profiles in the upper left of the plot present the density configuration at the time $t = 6$ s for all cases. (b) The predicted critical outlet width contour in the space of the hopper inclination angle μ and the wall friction angle ϕ_w	72

4.6	(a) Mass flow rate q_m of a fixed hopper inclination angle $\mu = 24^\circ$ for flowing pine materials (artificial and as-ground) with different friction angle $\phi_c = 30, 40$, and 47.3° . (b) Mass flow rate q_m variation with hopper inclination μ and outlet width W for different pine materials. Note that the dots here are used for fitting the equation. (c) Mass flow rate q_m of flowing the as-ground pine-1 sample with different hopper inclination $\mu = 24^\circ, 30^\circ$, and 36° . Note that “ \times ”s represent experimental measurements, circles stand for numerical results, and the lines and surfaces are predicted by the empirical equation in all plots here.	74
4.7	Validation of the empirical equation using Douglas fir flow data: mass flow rate q_m changing with hopper inclination μ and outlet width W , where “ \times ”s represent experimental measurements, circles stand for numerical results, and the surfaces are prediction of the fitting equation.	76
5.1	(a) The experimental inclined plane setup with a local coordinate system. A layer of biomass particles was glued on the ramp to realize the no-slip boundary condition. (b) Schematic view of the numerical model. Note the “Gate” was opened by releasing boundary constraints in modeling instead of sliding the side wall as in experiments. The dimensions of the experiment setup and the numerical model are the same except that the material height H in experiments is limited by the height of the storage box (0.915 m) while the H in numerical models can surpass the limit. (c) Particle size distribution of the loblolly pine chips used in this chapter and a photo demonstrating particle size and shape. (d) A velocity profile at the symmetric middle surface shows the variables measured in simulations, where h represents the thickness of the material and v stands for the flow velocity along the x direction. Both variables are spatially distributed and evolve with time.	83
5.2	Experimental and numerical results showing the flow of milled biomass. (a) A demonstration of experimental steps of the inclined plane flow tests and the region of material thickness measurement. (b) Modeling predicted velocity distribution of a flow test with an inclined angle of $\theta = 29.5^\circ$ and a gate opening of $h_0^0 = 0.35$ m. Note the 6 layers along the ramp were used to extract quantitative modeling results.	84

- 5.3 Sketch of DP- $\mu(I)$ model. (a) Yield surface in the principal stress space with demonstration of the π -plane and the friction angle in quasi-static regime ϕ_c^s . (b) Comparison of yield surfaces between G-B hypoplastic model and the DP- $\mu(I)$ model on the π -plane. Note the size of circular shaped yield surface in the π -plane for the DP- $\mu(I)$ model varies according to the value of dimensionless inertial number I , which is a function of shear rate. (c) A demonstration of friction coefficient μ evolving with the inertia number I at $\mu_s = \tan \phi_c^s = \tan 39.2^\circ$, $\mu_2 = \tan 56^\circ$, and $I_0 = 0.008$. The subplot presents that the inertia number I is a function of the pressure p with a fixed shear rate of 10 s^{-1} . (d) Elastic modulus E as a function of mean stress p 88
- 5.4 Demonstration of the flow responses ($\theta = 34^\circ$, $h_0^0 = 0.31 \text{ m}$) calculated by G-B hypoplastic model. (a,d) Predicted velocity and material thickness at the middle symmetric surface evolving with time, where different colors represent different layers. Note the velocity across the thickness of the flowing material is not a constant, only the velocity at the top flow surface is presented. (b,e) The steady-flow thickness h_{std} and the stopping thickness h_{stop} profiles along the width of the ramp, where \hat{y} is the normalized length along the y direction. Note that the color in (b) quantifies the velocity magnitude and the color in (e) stands for different layers. (c,f) The steady-flow velocity v_{std}^m , the steady-flow thickness h_{std} , and the stopping thickness h_{stop} along the length of the ramp, where $x = 0$ and $x = 1.22 \text{ m}$ are the start and the end of the ramp, respectively. 91
- 5.5 (a) The stopping thickness h_{stop} along the length of the ramp x for the inclined angle $\theta = 29.5^\circ, 34^\circ$, and 37° . Error bars represent the variation from cases with different gate opening heights h_0^0 . The error bars predicted from the G-B hypoplastic model are omitted because the predicted variations are negligible. (b) Steady flow velocity at the top symmetric surface v^m from various inclined angles θ and gate opening heights h_0^0 . Note that the experimental v^m are the run-out velocities. The marker “ \times ” stands for experimental measurements, “ \circ ” represents results from the DP- $\mu(I)$ model, and “ \triangle ” means predictions from the G-B hypoplastic model. 92
- 5.6 Flow profiles with various inclined angles θ predicted from the G-B hypoplastic model. (a,b) The stopping thickness h_{stop} and the steady flow thickness h_{std} distributed along the ramp x at different inclined angles θ . (c) Material thickness at the middle ramp as a function of inclined angle θ . The error bars of different steady flow thickness stem from the different gate opening heights h_0^0 . (d) Angle between the material top surface and the horizontal surface ω for varied inclined plane angle θ 95

5.7	Scaling law and inertial number distributions. (a) The Froude number Fr against the normalized thickness h_{std}/h_{stop} of pine chips obtained from the G-B Hypoplastic model and the DP- $\mu(I)$ model with different inclined angles θ . (b) The relation of the Froude number Fr and the normalized thickness h_{std}/h_{stop} for different granular materials: pine chips (this study), angular sand [148], glass beads-1 [148], and glass beads-2 [125]. (c) Inertial number distribution obtained during steady flow from Point ① ($\theta = 29.5^\circ$, $h_0^0 = 0.25$ m), Point ② ($\theta = 34^\circ$, $h_0^0 = 0.35$ m), and Point ③ ($\theta = 37^\circ$, $h_0^0 = 0.35$ m). Note that the 3 points are marked in (b) as “•”s.	97
5.8	Limitations of the DP- $\mu(I)$ model. (a) Material parameter I_0 is a function of θ . (b) Stopping thickness h_{stop} profile along the ramp x predicted from a fixed $I_0 = 9 \times 10^{-4}$. Error bars represent the variation from different gate opening heights h_0^0 . (c) Steady flow velocity at the symmetric surface top v^m with a fixed $I_0 = 9 \times 10^{-4}$. The symbol “×” stands for experimental measurements and “o” represents results from the DP- $\mu(I)$ model with a fixed I_0	99
6.1	Particle characterization results. (a) Results from the Thermogravimetric Analysis (TGA) showing the evolution of mass and its derivative by raising temperature. (b) Results from the Differential Scanning Calorimetry (DSC) tests presenting the heat flow as a function of temperature. (c) Determined Fiber Saturation Point (FSP) by direct calculation from each test with different starting moisture content shown as the horizontal axis. (d) Heat of fusion as a function of initial moisture content computed from the DSC tests.	105
6.2	Experimental results demonstrating the material compressibility. (a) The minimum density ρ_b^{min} as a function of the moisture content. (b) The maximum density ρ_b^{max} determined after vibration at different surcharge loads and different moisture contents. (c) Bulk density response changing with compressive pressure at different moisture contents determined from oedometer tests.	107
6.3	Angle of Repose (AoR) determined by funnel method as a function of the moisture content, where each point were averaged from 10 data points and the error bars represent the standard deviation.	107
6.4	(a) The maximum bulk density of samples after vibration at different moisture contents, where the lines from bottom to the top represent compressive pressure from zero to 10 kPa. (b) Particle skeleton density ρ_{sk} , defined as the bulk density of particle skeleton (solids), as a function of the moisture content.	108

6.5	Numerical model of the hopper flow test. (a) A 3D wedge-shaped hopper with a cuboid bin above it. The numerical model simulated a plane-strain slice of 0.025 m thickness. (b) The 2D cross section of the model. No-slip boundary condition was applied on both hopper walls by fixing all 6 degrees of freedom of the boundary nodes. The flow rate was measured by extracting the density and flow velocity of the outlet elements and nodes, respectively.	110
6.6	Hopper flow response with respect to discharged mass m_t and mass flow rate q_m . (a) Time lapse discharged mass m_t at different moisture contents, where the slope stands for the mass flow rate q_m , q_m is plotted in (c) against moisture content. (b) Effective discharged mass m_t^s , defined as the discharged total mass of solid (with water removed), changing with time. The effective mass flow rate q_m^s is plotted in (d) against moisture content.	111
6.7	Hopper flow response with respect to discharged volume V_t and volumetric flow rate q_V . (a,b) Discharged volume V_t and effective discharged volume V_t^s , defined as the discharged total volume subtracting the volume of water, evolving with time t . (c,d) Volumetric flow rate q_V and effective volumetric flow rate q_V^s changing against moisture content.	112

SUMMARY

Biomass has been considered as one of the most promising alternatives for fossil fuels for its abundance and easy access. However, the commercialization of bioenergy has been significantly limited by various material handling issues, manifested in jamming or poor flowability of milled biomass materials in various industry equipment. The development of safe and efficient feedstock handling equipment centers on the fundamental understanding of the constitutive and rheological behavior of milled biomass materials, which remain largely unknown. To fill these knowledge gaps, this study combines experimental and numerical methods to understand the mechanical and rheological properties of milled woody particles across particle, meso, and industry scales at both quasi-static and dynamic regimes, and uses the findings to guide and optimize the design of the next-generation biomass handling equipment.

Comparing with sands and glassbeads, woody biomass particles have high angularity, high aspect ratio, and considerable particle deformability due to pores inside particles. These characteristics make biomass materials highly compressible and difficult to flow. Calibrated against a series of laboratory experiments, the Gudehus-Bauer hypoplastic model is implemented to predict the flow of milled woody particles through industry hoppers. Material properties and hopper geometries that govern the jamming, mass flow, or funnel flow patterns are identified, which can guide the design of the hopper for improved flowability of milled biomass materials. To capture the material behavior at high particle flow rates, i.e., at the dynamic dense flow regime, a multi-regime $DP-\mu(I)$ model is formulated, implemented, and validated against laboratory inclined plane tests. With this new constitutive model, the multi-regime flow physics and the scaling law of flowing milled biomass are established for milled woody particles. In the end, the effects of moisture content on the compressibility and frictional behavior of milled woody biomass are studied and their impacts to the hopper flow behavior are evaluated. The overall flowability of milled

woody particles decreases with increasing moisture content up to its fiber saturation point, beyond which moisture has no impacts to the flowability.

CHAPTER 1

INTRODUCTION

1.1 Motivation

There are over three trillion trees in the world [1]. Trees, crops, and some municipal solid wastes can be all categorized as biomass materials and can be converted to energy, which is called bioenergy [2]. The U.S. Department of Energy has envisioned over one billion tons of non-food biomass to be produced annually by 2040, which could replace 30% of the U.S. petroleum consumption based on the 2005 consumption level [2]. However, the biomass-derived energy currently accounts only less than 5% in U.S. energy consumption by source [3].

One of the biggest challenges in bioenergy industry is the unreliable operations during feedstock handling [4], which are manifested as unstable flows, jamming, or even failures of handling equipment like hoppers, screw feeders, and conveyors [5, 6, 7, 8, 9]. Fundamentally, these handling upsets are caused by the poor flowability of particulate biomass materials. Up to date, we still lack the scientific understanding of the flow physics of milled biomass, as well as high-fidelity models to characterize and predict their flow behavior going through various industrial equipment.

To address these challenges, this study aims to promote the understanding of the flow physics of milled biomass materials focusing on the following four aspects: 1) macro-scale granular flow patterns in industry hoppers and modeling-assisted design guide of the hoppers, 2) meso-scale flow characterization and high-fidelity numerical prediction, 3) micro-scale mechanisms of particle-water interaction their effects on the larger scale flow behavior, and 4) granular flow characterization and modeling at both quasi-static and dense-flow (dynamic) flow regimes.

1.2 Thesis Organization

The work in this dissertation is organized in the following six chapters:

- Chapter 2 reports the flow characterization of milled biomass materials with laboratory experiments and FEM simulations. A numerical model has been developed and validated to simulate the flow of biomass particles in both quasi-static and dynamic flow regimes.
- Chapter 3 numerically investigates the flow and jamming physics of milled woody biomass in wedge-shaped hoppers. The effects of hopper geometry, particle density, material packing, and hopper filling height have been evaluated.
- Chapter 4 bridges the gap between state-of-the-art understanding of flow behavior and the industrial equipment design by providing a modeling-assisted design guide for wedge-shaped hoppers. Specifically, the critical material attributes and critical hopper processing parameters are identified for hopper flow performance with respect to flow patterns, arching, and flow throughput.
- Chapter 5 studies the multi-regime flow behavior of biomass particles flowing on an inclined plane. A multi-regime constitutive model is formulated and compared with the conventional model on simulating the flow of milled biomass materials.
- Chapter 6 explores the flow behavior of biomass particles affected by moisture content by particle characterization and laboratory tests. The moisture-induced effects on hopper flow are also evaluated.
- Finally, Chapter 7 summarizes the key findings and contributions of this dissertation as well as future studies.

The research in this work has resulted in the following journal manuscripts published or in preparation:

- Chapter 2: Lu, Y., Jin, W., Klinger, J., Westover, T. L., & Dai, S. (2021). Flow characterization of compressible biomass particles using multiscale experiments and a hypoplastic model. *Powder Technology*, 383, 396-409.
- Chapter 3: Lu, Y., Jin, W., Klinger, J., & Dai, S. (2021). Flow and arching of biomass particles in wedge-shaped hoppers. *ACS Sustainable Chemistry & Engineering*, 9(45), 15303-15314.
- Chapter 4: Lu, Y., Jin, W., Saha, N., Klinger, J., Xia, Y., & Dai, S., Wedge-shaped hopper design for milled woody biomass flow, *ACS Sustainable Chemistry & Engineering*, accepted.
- Chapter 5: Lu, Y., Jin, W., Klinger, J., Saha, N., Xia, Y., & Dai, S., Characterization and modeling on the multi-regime flow behavior of particulate biomass, in preparation.
- Chapter 6: Lu, Y. & Dai, S., Effects of moisture content on flow behavior of milled biomass, in preparation.

CHAPTER 2

FLOW CHARACTERIZATION AND MODELING USING MULTISCALE EXPERIMENTS AND A HYPOPLASTIC MODEL

2.1 Introduction

According to a workshop organized by the U.S. DOE Bioenergy Technologies Office (BETO) [4], handling the milled biomass feedstock through storage, transport, and feeding processes contribute most to the overall downtime of biorefineries [10, 8]. Fundamentally, all these process upsets, which are manifested as hopper arching and rat-holing, screw feeder jamming and plugging [9], are caused by the poor flowability of the biomass feedstocks [4, 11]. The design and operation of the current handling equipment are either based on trial-and-error experience or on the assumption that the flow behavior of the granular material is well-captured by the Mohr-Coulomb (M-C) model [12]. The M-C model assumes a linear relationship between material shear strength and effective confining stress, which works well for conventional granular materials (e.g. sand, agriculture grains, pharmaceutical pills). However, it is highly inaccurate for biomass feedstocks due to their high compressibility and other factors, such as complex particle morphology.

Physical characterization of the flowability of biomass feedstock can be broadly categorized into three groups based on experimental scales: (1) particle-scale characterization of moisture content, particle shape/size and their corresponding distributions from traditional sieve test or novel image analysis [13, 14, 15, 16]; (2) meso-scale characterization of bulk properties, such as bulk density and bulk elasticity tested by the Carr test or the oedometer test [17, 12], friction angle/shear strength from the angle of repose test [18], Schulze/Peschl shear tests [13, 17], Jenike/direct shear tests [18, 19], or the triaxial shear test [20, 21, 22]; (3) pilot-scale characterization of flow performances, such as the hop-

per arching test [7, 17], silo/hopper flow tests [23, 24], and auger/screw feeding tests [17, 6]. Analysis of these characterization results has been focused on connecting particle-scale properties (e.g., shape, size) to meso-scale bulk properties (e.g., unconfined yield strength, Carr or Hausner indices)[25], and subsequently utilizing bulk properties to predict the flow performance in silos/hoppers using statistic methods[6]. A common practice, proposed by Jenike [26], is to construct a flow function in terms of unconfined yield strength and major principle stress, which can then be used to optimize the hopper design [27, 23]. Limited success has been reported in the literature for biomass granulate material due to the invalid assumption (i.e., the M-C model) associated with the shear tests and the Jenike procedure. In addition, the successful match between prediction and measurements are limited for a handful of samples and at small scales.

Modeling and simulation have played a significant role in the design and operation of other industrial processes, such as food and pharmaceutical handling. With a robust computational model to capture the flow behavior of biomass, we can decipher the complex relationship between bulk properties and flow metrics (e.g., flow rate, minimum hopper outlet size, etc.) at the industrial scale.

Given the capability to explicitly consider the complex particle morphology and particle compressibility, the Discrete Element Model (DEM) is well suited to understand the granular interaction of biomass feedstock [28, 29, 30, 31]. However, DEM faces substantial computational cost limits for large scale modeling even with supercomputer capability.

Continuum mechanics models that assume a continuous material can greatly reduce the computational burden to enable industry-scale simulations. Nevertheless, the successful modeling of the flow of milled biomass or granular materials in general, faces several major challenges [32]. The first challenge is the incompetence of existing models to handle simultaneously quasi-static small deformation when the material is in storage and large deformation when the material is in feeding and transportation. The mesh-based Arbitrary Lagrangian-Eulerian (ALE) method [33, 34], the Coupled Eulerian-Lagrangian

(CEL) method [35, 36], and the Material Point Method [37, 38], as well as the mesh-less based smoothed-particle hydrodynamics (SPH) [39] have being used to address this challenge with mixed success. The second challenge is to formulate a constitutive law that can capture the complex mechanical behavior of milled biomass material throughout both quasi-static and dynamic regimes. Jin et al. [12] adopted the density dependent modified Drucker-Prager/Cap (MDPC) model to simulate the quasi-static ring shear test for pine chips and found that the MDPC model can mimic the high compressibility of pine chips during the initial shear step, yet fails to manifest the dilation of the real material when the shear zone is fully mobilized. The third challenge is to establish procedures to calibrate constitutive parameters from physical experiments. For conventional granular materials, constitutive parameters can be extracted from standard tests directly. For biomass feed-stock, the suitability of those standard tests is dubious for a variety of reasons, not the least of which is the compressibility of the particles that greatly complicates measuring the full stress state during critical flow.

In this chapter, the suitability of a hypoplastic model to capture both the quasi-static shear behavior and the dynamic flow behavior of ground loblolly pine is investigated. The outline of the hypoplastic model with robust implementation is firstly introduced and validated in the Abaqus Finite Element Package in section 2.2. The calibration process combining experimental data extraction and simulation-based fitting in section 2.3 are then presented. The capabilities and the limitations of the hypoplastic model to capture the quasi-static shear behavior and the dynamic flow behavior are evaluated by comparing numerical prediction against experimental measurements of a customized axial shear test in section 2.4 and a pilot-scale hopper flow test in section 2.5, respectively. Conclusions are provided in section 2.6. ¹

¹The experimental work in this chapter were conducted by the Idaho National Laboratory.

2.2 Gudehus-Bauer hypoplastic model

2.2.1 Model outline

Constitutive models to simulate the inelastic nonlinear shear behavior of granular material can be grouped into three categories: rheological models, hyperplastic models, and hypoplastic models [32]. They are distinguished from each other by their mathematical frameworks and suitability for modeling different flow regimes. The rheological models are formulated to have shear-rate dependent behavior, a concept from fluid mechanics, and they are suited for modeling granular shear in rapid flow regime. The hyperplastic models, also known as elastoplastic models, assume elastic deformation within a specified yield criteria (surface) and plastic shear deformation on the yield surface. The hyperplastic models do not consider shear rate dependence, and they are mostly suitable for modeling quasi-static shear flow [12]. The hypoplastic models are also formulated to characterize quasi-static shear behavior of granular material; however, they do not have explicit expressions to define the yield surface. Instead, the constitutive stress-strain relationship is incrementally nonlinear for all stresses in all directions of strain. This nonlinear feature makes hypoplastic models particularly attractive to simulate the flow of materials that exhibit nonlinear compressibility, such as biomass [40, 41] and soils [42, 43, 44].

Granular biomass material handled by various equipment exhibits complex shear flow behavior, such as stress hardening/softening accompanied by contraction/dilation, critical state shear flow, and nonlinear elasticity. The advanced hypoplastic model, proposed by Gudehus [45] and Bauer [46] (termed as the G-B model hereafter), can capture most of these behaviors and is used for characterizing the shear flow behavior of ground pine in this study. The constitutive law for the G-B model is expressed in rate-type evolutionary equation

$$\dot{\sigma}_{ij} = F(e, \sigma_{kl}, d_{kl}), \quad (2.1)$$

where $\dot{\sigma}_{ij} = \dot{\sigma}_{ij} - \omega_{ik}\sigma_{kj} + \sigma_{ik}\omega_{kj}$ is the objective (Jaumann) stress-rate tensor, and ω_{ij}

Table 2.1: Fomulation of G-B hypoplastic model.

Jaumann stress rate	$\dot{\sigma}_{ij} = f_s \left[L_{ij}(\hat{\sigma}_{kl}, d_{kl}) + f_d N_{ij}(\hat{\sigma}_{ij}) \sqrt{d_{kl} d_{kl}} \right]$
Linear contribution	$L_{ij} = a_1^2 d_{ij} + \hat{\sigma}_{ij}(\hat{\sigma}_{kl} d_{kl})$
Nonlinear contribution	$N_{ij} = a_1(\hat{\sigma}_{ij} + \hat{\sigma}_{ij}^*)$
	$a_1^{-1} = c_1 + c_2 \sqrt{\hat{\sigma}_{kl}^* \hat{\sigma}_{lk}^*} [1 + \cos(3\theta)]$
	$c_1 = \sqrt{\frac{3}{8}} \left(\frac{3 - \sin \phi_c}{\sin \phi_c} \right), \quad c_2 = \frac{3}{8} \left(\frac{3 + \sin \phi_c}{\sin \phi_c} \right)$
Lode angle	$\cos(3\theta) = -\sqrt{6} \hat{\sigma}_{kl}^* \hat{\sigma}_{lm}^* \hat{\sigma}_{mk}^* / (\hat{\sigma}_{kl}^* \hat{\sigma}_{lk}^*)^{1.5}$
Pycnotropy factors	$f_d = \left(\frac{e - e_d}{e_c - e_d} \right)^\alpha, \quad f_e = \left(\frac{e_c}{e} \right)^\beta$
Barotropy factor	$f_b = \left(\frac{e_{i0}}{e_{c0}} \right)^\beta \frac{h_s}{n h_i} \left(\frac{1 + e_i}{e_i} \right) \left(-\frac{\sigma_{kk}}{h_s} \right)^{1-n}$
Stiffness factor	$f_s = f_b f_e$
	$h_i = \frac{1}{c_1^2} + \frac{1}{3} \left(\frac{e_{i0} + e_{d0}}{e_{c0} - e_{d0}} \right)^\alpha \frac{1}{c_1 \sqrt{3}}$
Void ratio evolution	$\frac{e_i}{e_{i0}} = \frac{e_d}{e_{d0}} = \frac{e_c}{e_{c0}} = \exp \left[- \left(\frac{-\sigma_{kk}}{h_s} \right)^n \right]$
	$\dot{e} = (1 + e) d_{kk}$
e_c : critical void ratio	$\hat{\sigma}_{ij} = \sigma_{ij} / \sigma_{kk}$: normalized stress tensor
e_i : maximum void ratio	$\hat{\sigma}_{ij}^* = \hat{\sigma}_{ij} - \frac{1}{3} \delta_{ij}$: normalized deviatoric stress tensor
e_d : minimum void ratio	α : peak-critical stress transition exponent
ϕ_c : critical friction angle	β : stiffness variation exponent
h_s : granulate hardness	n : pressure-sensitive exponent

is the anti-symmetrical spin tensor. The Jaumann stress-rate is defined as a function of the current void ratio e , the Cauchy stress tensor σ_{kl} and the strain rate (stretching) tensor d_{kl} . Its explicit formulation is summarized in Table 2.1. References [45] and [46] contain detailed explanations on the formulation. A few remarks can be made:

- The Cauchy stress σ_{ij} and the void ratio e sufficiently characterize the state of the granular material.
- The critical state theory, defined as the state of stress and the void ratio (density) upon which material can shear/flow infinitely with no change in volumetric strain (i.e. constant e_c) [47], is incorporated in the formulation.
- The critical stress surface (characterized by the friction angle) at the principle stress space depends on the deviatoric stress direction (i.e. the Lode angle).
- In addition to the critical state void ratio e_c , there is an upper bound e_i and a lower

bound e_d for void ratio at a given mean stress ($-\sigma_{kk}/3$). The bounds are the loosest and the densest states that granular material can achieve through particle rearrangement.

- The maximum, the minimum, and the critical void ratios (e_i, e_d, e_c) all decrease with increasing mean pressure ($-\sigma_{kk}/3$) [46].
- The G-B model is strain rate independent although the constitutive equations are expressed in rate form.

2.2.2 Model implementation and validation

The G-B model was implemented in the Abaqus/Explicit Finite Element package through the user-defined material subroutine VUMAT. The rate form of the G-B model makes its implementation straightforward, especially when a forward Euler integration is adopted. The unknown stress and void ratio at the end of each time increment is updated directly from the solution at the start of the time increment without iteration. However, this simplification is at the price of conditional stability. Numerical stability is achieved by limiting the time step to less than a critical time step Δt_{crit} , which is defined by the ratio of the characteristic element length l_e over the stress wave speed c_d . Mathematically, $\Delta t \leq \Delta t_{crit} = l_e/c_d$. It is worth noting that the Abaqus VUMAT uses the corotational coordinate system, and the stress and strain increment tensors provided at the start of the increment are already in the rotated frame attached to the material. In addition, the objective stress rate is also frame indifferent. Therefore, rotating the updated stress is not needed. However, Abaqus VUMAT asks the user to provide the Green-Naghdi stress rate ($\hat{\sigma}_{ij}$) while the G-B model is formulated to yield the Jaumann stress rate ($\dot{\sigma}_{ij}$). At the end of integration, The relative spin tensor ($\Omega_{ij} - \omega_{ij}$) was used to accommodate the difference

Table 2.2: G-B model parameters of Karlsruhe sand used for the oedometer test simulations

ϕ_c [°]	h_s [MPa]	n [-]	e_{d0} [-]	e_{c0} [-]	e_{i0} [-]	α [-]	β [-]
30	5800	0.28	0.53	0.84	1.0	0.13	1.0

between the Jaumann and the Green-Naghdi stress rates through:

$$\begin{aligned}\hat{\sigma}_{ij} &= \dot{\sigma}_{ij} - \Omega_{ik}\sigma_{kj} + \sigma_{ik}\Omega_{kj} - \omega_{ik}\sigma_{kj} + \sigma_{ik}\omega_{kj} - (-\omega_{ik}\sigma_{kj} + \sigma_{ik}\omega_{kj}) \\ &= \overset{\circ}{\sigma}_{ij} - (\Omega_{ik} - \omega_{ik})\sigma_{kj} + \sigma_{ik}(\Omega_{kj} - \omega_{kj}),\end{aligned}\quad (2.2)$$

where Ω_{ij} is another Abaqus built-in spin tensor.

In order to validate the implementation, two oedometer tests were simulated using known G-B model parameters for Karlsruhe sand (Table 2.2) and compared model predictions against experimental data [48]. As shown in Figure 2.1, an axially symmetric single element is constructed in Abaqus with a fixed radial displacement. An axial stress of 300 kPa (σ_z) is applied and then unloaded in accordance with experimental procedures. The computational framework of hypoplastic models cannot proceed with zero initial stress, and thus, a hydrostatic pressure $-\sigma_{kk}/3 = 10$ Pa was assigned as the initial stress in the absence of gravity. As discussed previously, the G-B model is rate independent given the load increment is small enough to satisfy the critical time step.

Figure 2.1 presents the model predicted radial stress (σ_r), axial stress (σ_z) and axial strain (ϵ_z) against the corresponding experimental data [46] from two oedometer tests. It can be seen that in general, the numerical predictions agree well with the experimental data. The axial tangential stiffness increases and then decreases as the load is applied and then relaxed, respectively. Also, the compressibility varies with the initial void ratio: the densely packed sample ($e_0 = 0.55$) has less axial strain in comparison with the loosely packed sample ($e_0 = 0.77$). The agreement between the prediction and the measurement is better in the loading step than in the unloading step. The prediction in the unloading step can be improved by developing a set of more calibrated constitutive model parameters.

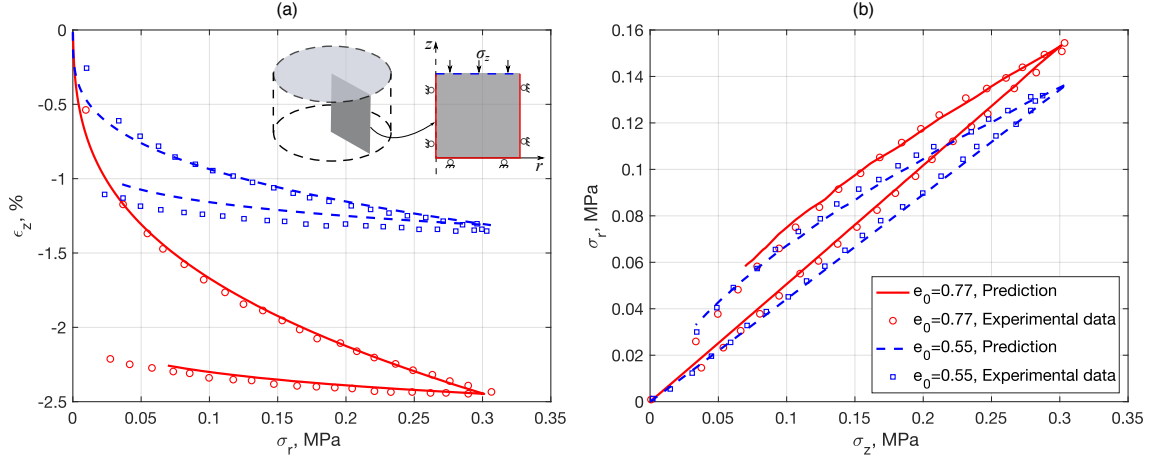


Figure 2.1: Comparison between numerical predictions and experimental measurements [46] of oedometer tests.

2.3 Material parameters calibration

The G-B model has eight constitutive parameters to fully characterize the mechanical behavior of granular material [46]. As shown in Table 2.1, the parameters e_{d0} , e_{c0} and e_{i0} are the minimum, the critical, and the maximum void ratios at zero pressure; the parameter ϕ_c characterizes the shear behavior at critical state; the parameter α describes the peak state shear behavior; and the parameters h_s , n and β are closely related to material compressibility. Following the proposed procedures by Herle and Gudehus [48], all these material parameters were calibrated directly from index tests and compression tests, and indirectly from comparing the numerical simulation of ring shear tests against experiments.

2.3.1 Loblolly pine samples

Loblolly pines used in this study were grown in a Georgia pine plantation and harvested at 24 years of maturity. Complete details of the prepared pine feedstock were given previously [12]. Briefly, the trees were processed through a flail chain to remove most of the bark, limbs and needles, and then fed into a chipper. The pine chips were then ground and dried in a rotary drum to obtain a granular sample with a final moisture content of approximately 6%. The ground particles passed through the sieve with 6mm in size constitute a

representative sample that would be used in a thermochemical conversion biorefinery and is denoted *as-ground*. The fines content has a significant influence on the mechanical behavior of the granular material. To quantify this influence, the SWECO sieve system was used with a 0.85mm screen to separate out the majority of fines from the *as-ground* sample, and the remaining sample with particle size above 0.85mm is denoted as *engineered*. The SWECO system is made of motor feet with an eccentric weight to cause screen vibration, and it can continuously operate to make large sample volumes. The particle size distribution of the two samples is presented in Figure 2.2(a) with photographs demonstrating their morphology. Note that the sieve system is not capable of characterizing fine particles, the blue dashed line in Figure 2.2(a)) is extrapolated.

2.3.2 Parameters determined from physical measurements

Parameters: granulate hardness h_s and exponent n These two parameters mainly control the compressibility at bulk scale, and are determined via cyclic oedometer tests using initially very loosely packed specimens. Details of the experiments used to determine these parameters have been published previously [12]. Figure 2.2(b) shows representative curves of void ratio e plotted as a function of mean stress p for the two samples. Note that the formula $e = \rho_s / \rho_b - 1$ was used to transform the bulk density ρ_b into void ratio using particle density ρ_s . The value of particle density ρ_s from direct measurement is challenging since pores exist within pine particles and the current technologies cannot distinguish the inner pores from the exterior pores (void space among particles) [29]. Variability within the samples resulting from differences in tree age and height [49], plantation location [50], and particle grain direction from the major axis [51, 52] adds another layer of complexity in determining particle density. With information on tree age and plantation location of the studied pine, a particle density ρ_s of 430 kg/m³ is used throughout this chapter based on the prior studies [49, 50, 29].

Given the the semi-logarithmic relation of $e - \log p$ plot (Figure 2.2(b)), the granular

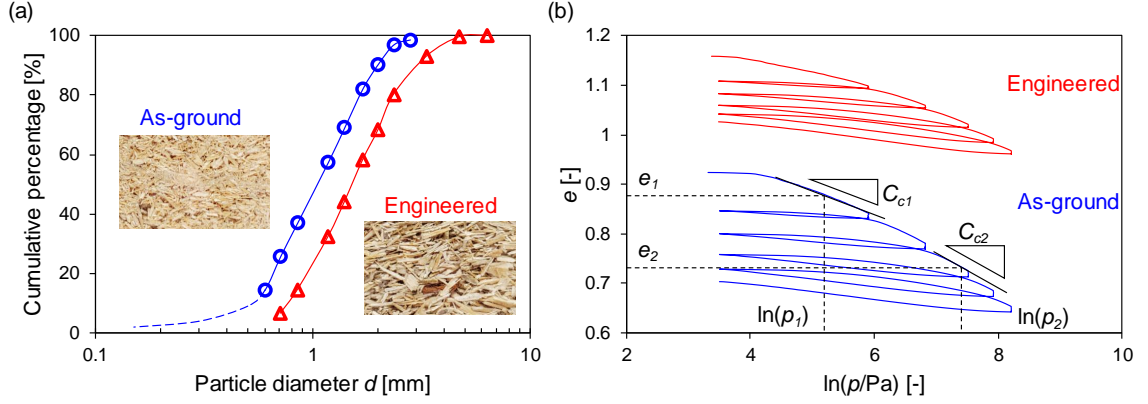


Figure 2.2: (a) The particle size distribution of two investigated samples with the corresponding photographs demonstrating particle morphology. The blue dashed line is extrapolated due to the limitation of the particle size characterization using the sieving method. (b) Semi-logarithmic relation between void ratio e and mean stress p of the two samples as measured using oedometer tests. Three replicate oedometer tests were performed for each sample, then h_s and n were calculated from Equation 2.3 and averaged. Moreover, different pairs of points on the $e - \ln(p)$ curve are used to calculate h_s and n . The variations caused by different tests and different pairs of points on the $e - \ln(p)$ curve are found negligible.

hardness h_s and the exponent n can be obtained using the following equations [48]:

$$h_s = 3p \left(\frac{ne}{C_c} \right)^{\frac{1}{n}}, \quad n = \frac{\ln\left(\frac{e_1 C_{c2}}{e_2 C_{c1}}\right)}{\ln\left(\frac{p_2}{p_1}\right)}, \quad (2.3)$$

where $p = -\sigma_{kk}/3$, $C_c = -e/\ln p$. Importantly, only the vertical compressive stress is measured during the oedometer test, such that the lateral stress is unknown. Based on the extremely small Poisson's ratio of the material [12], the ratio of lateral stress to vertical stress, denoted as K_0 , is assumed 0.05. With this assumption, the granulate hardness $h_s = 187.6$ kPa and exponent $n = 0.30$ were calculated for the *as-ground* sample, and $h_s = 1034.6$ kPa, $n = 0.35$ for the *engineered* sample.

Parameter: minimum void ratio at zero pressure e_{d0} The minimum void ratio e_{min} corresponds to the maximum bulk density according to $e_{min} = \rho_s/\rho_{b,max} - 1$. To obtain the the maximum bulk density $\rho_{b,max}$, vibratory table tests were performed at fixed pressure following the ASTM standard test [53]. Figure 2.3 shows the results for the two samples.

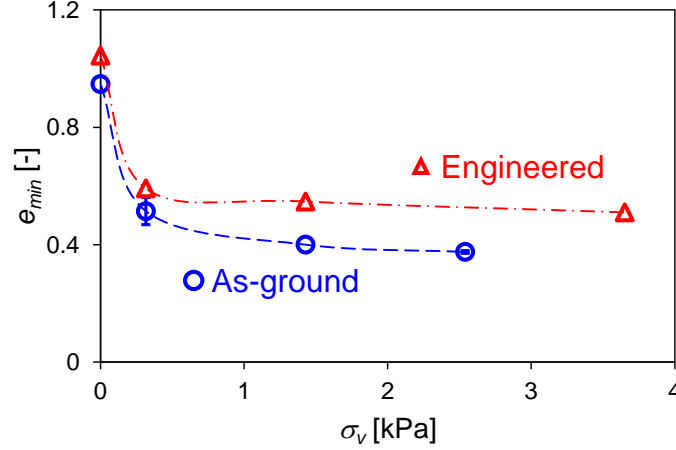


Figure 2.3: The obtained relation of minimum void ratio e_{min} with applied compression σ_v from vibration test.

The measured data is very consistent at the same level of applied force (shown as the error bars in Figure 2.3), thereafter, only one test at each condition was conducted. The parameter of minimum void ratio at zero pressure e_{d0} is obtained from the void ratio evolution equation (Table 2.1):

$$\frac{e_d}{e_{d0}} = \exp \left[- \left(\frac{-\sigma_{kk}}{h_s} \right)^n \right], \quad (2.4)$$

where $e_d = e_{min}$ is the minimum void ratio at the corresponding pressure $p = -\sigma_{kk}/3$. According to Bauer [46], Equation 2.4 is not valid when the mean stress approaches the extremes ($-\sigma_{kk} \rightarrow 0/\infty$). Therefore, the maximum mean stress vs. the minimum e_{min} tested in experiments were used, and the obtained minimum void ratio at zero pressure $e_{d0} = 0.50$ for the *as-ground* sample, and $e_{d0} = 0.59$ for the *engineered* sample, respectively. In this calculation, the values previously determined for h_s and n are used.

Parameter: critical void ratio at zero pressure e_{c0} The assumption is adopted here that the critical void ratio at zero pressure is equal to its maximum void ratio (i.e. $e_{c0} \approx e_{max}$) at zero pressure [54, 48]. Following the ASTM standard [55], several sample preparation methods were used, including funnel pouring [53], tubing [55] and “rainfall”, to obtain the minimum bulk density, which corresponds to the maximum void ratio. The rainfall

approach in which all particles are dropped freely and randomly into the container from a height of 0.4 m above the container is not included in the standard. Results show that the rainfall approach is stable and generates the loosest packing for pine chips. It is due to the low particle density and the sheet-like particle shape, which induce higher air drag force comparing to conventional granular material. The funnel pouring method and the tubing method resulted in the most aligned particles with the highest bulk density. The determined value of e_{c0} is 1.06 for the *as-ground* sample, and 1.19 for the *engineered* sample, respectively.

2.3.3 Modeling assisted calibration

Parameter: maximum void ratio at zero pressure e_{i0} Measuring the maximum void ratio at zero pressure e_{i0} is experimentally challenging [48] due to the requirement of gravity-free condition. Following Herle and Gudehus [48], the ratio e_{i0}/e_{max} can be estimated in the range of 1.2-1.3. Sensitivity analysis was conducted to quantify the influence of e_{i0} on the compaction and shear behavior by simulating single-element oedometer and simple-shear tests. it is found that the compressibility and shear behavior of pine chips are not sensitive in e_{i0} . Given e_{i0} is used to bound the void ratio, the maximum ratio of $e_{i0}/e_{max} = 1.3$ is adopted for the *as-ground* sample, which results in $e_{i0} = 1.38$; $e_{i0}/e_{max} = 1.2$ is adopted for the *engineered* sample, which results in $e_{i0} = 1.42$.

Parameter: exponent β In addition to the granulate hardness h_s and exponents n , the exponent β also controls material bulk compressibility. β was calibrated indirectly via a single-element oedometer model (Figure 2.4(a)) by matching numerical prediction of density evolution against experimental measurements as shown in Figure 2.4(b). Note the parameters calibrated in previous sections (h_s , n , e_{d0} , e_{c0} and e_{i0}) are used in simulation, along with the friction angle ϕ_c and the exponent α determined in the next section. The value of ϕ_c and α have negligible effects on the material compressibility, and the deter-

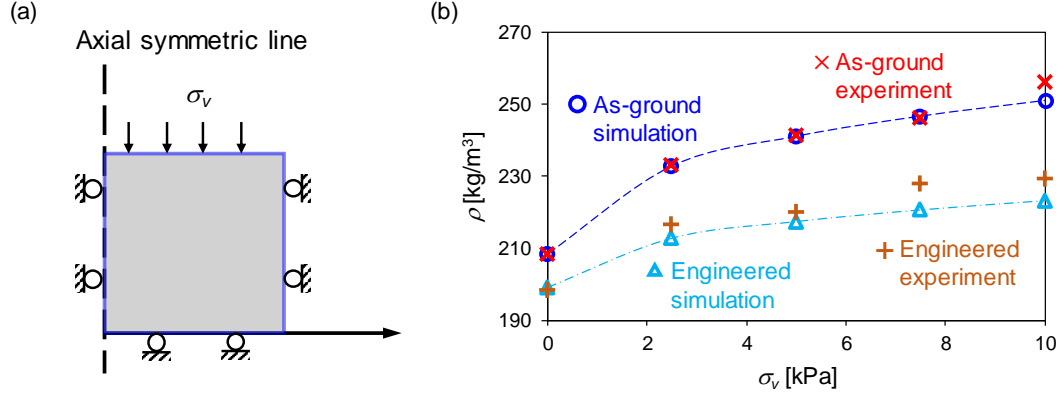


Figure 2.4: Numerical calibration process to determine the exponent β : (1) simulation of a suite of oedometer tests using a single axial symmetrical element model (a) with different input β ; (2) calibration of β by finding the best match of bulk density ρ_b evolution under different level of compression σ_v between numerical prediction and experimental measurements using least-square method (b).

mination of β is not sensitive to ϕ_c and α . The least-square method was used to find the best fitted $\beta = 1.0$ for the *as-ground* sample, and $\beta = 0.5$ for the *engineered* sample, respectively.

Parameter: friction angle at critical state ϕ_c The G-B hypoplastic model uses the friction angle ϕ_c to determine shear behavior of the material at the critical state. The critical state of the loblolly pine is not typically achieved using the standard ASTM procedures of the Schulze ring shear test [56]. The procedure was modified by continuously shearing the material until both the shear stress and the density reach their steady-state values to achieve the critical state [12]. This modification allows the critical state to be achieved in the shear zone, where the friction is fully mobilized upon sufficient shear.

Figure 2.5(a) shows the typical shear response from the modified Schulze ring shear test. The blue line and green dashed line stand for the experimental and numerical shear stress τ , respectively, and the red dot-dashed line represents the experimental bulk density ρ_b . In the modified shear procedure, the sample was first pre-sheared under a constant vertical stress σ_v (10 kPa in this case) until its critical state was achieved, then the shear stress was fully unloaded. Next, the sample was sheared again under a reduced level of

normal stress ($\sigma_v = 5$ kPa in this case) to reach the critical state ($\tau = \tau_c$ at critical state). A peak shear stress (shear strength) τ_p is observed during the second shear step.

The measured critical shear stress τ_c against the corresponding vertical stress σ_v is plotted in Figure 2.5(b-c) as red dots. Through the linearization of the critical state points (σ_v, τ_c) according to the classical Mohr-Coulomb law $\tau_c = \sigma_v \tan \phi_c$, we can obtain that the critical state friction angle ϕ_c for the *as-ground* (respectively, *engineered*) sample is 39.2° (respectively, 40.8°). It is well understood that the friction angle is stress state-dependent [12, 32]. The value measured from the modified Schulze ring shear test using the M-C approximation, denoted as ϕ_c^{rs} , is different from triaxial compression test, denoted as ϕ_c^{tc} , and the G-B model uses ϕ_c^{tc} . This discrepancy between definitions of the different stress states can be corrected using the Lode angle, which is defined as:

$$\theta = \frac{1}{3} \cos^{-1} \left[\frac{J_3}{2} \left(\frac{3}{J_2} \right)^{3/2} \right], \quad (2.5)$$

where $J_2 = \frac{1}{2} \mathbf{s} : \mathbf{s}$ and $J_3 = \frac{1}{3} \mathbf{s} : \mathbf{s} \cdot \mathbf{s}$ are the second and third deviatoric stress invariants, respectively, and the deviatoric stress is defined as $\mathbf{s} = \boldsymbol{\sigma} - \frac{1}{3} \text{Tr}(\boldsymbol{\sigma}) \mathbf{I}$. With Lode angle θ , the relation between the critical state friction angle for triaxial compression ϕ_c^{tc} and for the ring shear ϕ_c^{rs} can be expressed [57] as

$$\tan(\phi_c^{rs}) = \tan(\phi_c^{tc}) - \frac{\tan^2(\phi_c^{tc})}{3 + \tan(\phi_c^{tc})} \cos \left(\frac{3\theta^{rs}}{2} + \frac{\pi}{4} \right). \quad (2.6)$$

Equation 2.6 is supported by experimental data [58], and critical state friction angle has the largest value under triaxial compression stress state ($\sigma_1 = \sigma_2 \geq \sigma_3$) where $\theta = 30^\circ$, and gradually decreases to pure shear stress state ($\sigma_2 = (\sigma_1 + \sigma_3)/2$) where $\theta = 0^\circ$, eventually has the lowest value at triaxial extension stress state ($\sigma_1 \geq \sigma_2 = \sigma_3$) where $\theta = -30^\circ$.

As discussed in Jin et al. [12], the Schulze ring shear tester cannot capture the full stress state, which results in an unknown value of the Loge angle θ^{rs} . We cannot use the Equation 2.6 to directly obtain ϕ_c^{tc} from ϕ_c^{rs} . Instead, a series of numerical simulations of ring

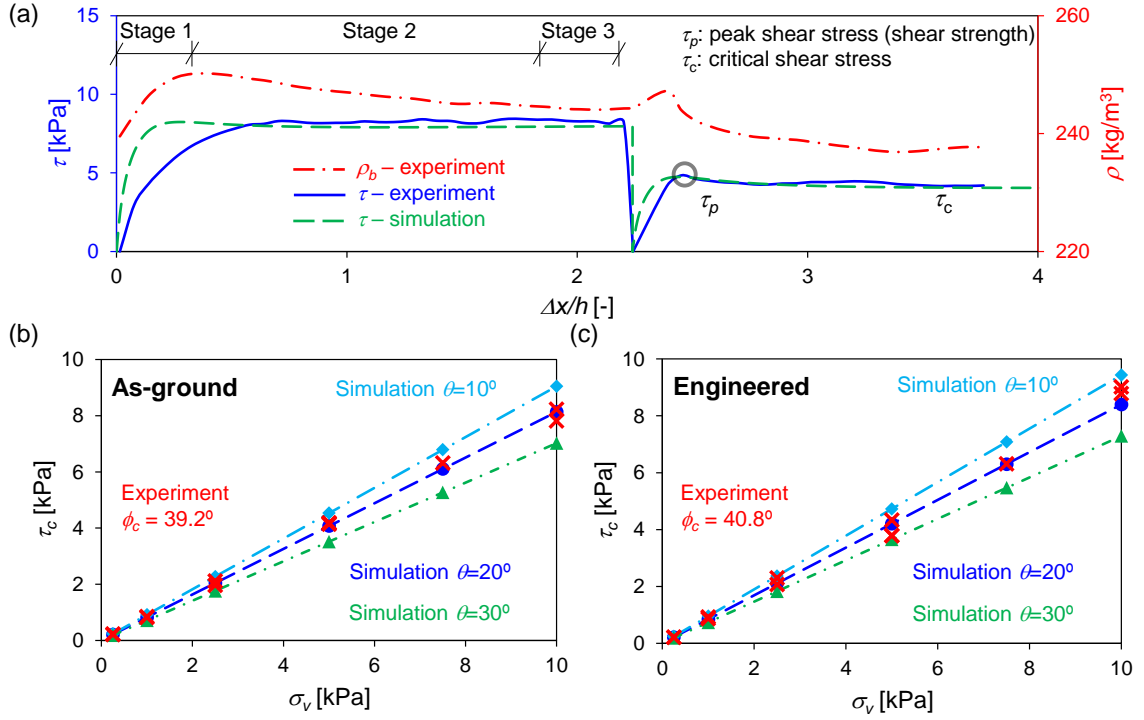


Figure 2.5: Shear behavior from the Schulze ring shear test. (a) A typical shear response where numerical (green dashed line) and experimental (blue line) shear stress τ , as well as experimental bulk density ρ_b (red dot-dashed line) are plotted versus strain $\Delta x/h$ for the *as-ground* sample. The applied vertical stress σ_v at the pre-shear step and the second step is 10 kPa, and 5 kPa, respectively. The peak shear stress (shear strength) τ_p and critical state shear stress τ_c are obtained. (b-c) The relation of the critical state shear stress τ_c against the normal stress σ_v from the ring shear test for the two samples. The red 'x's' are obtained from the experiment. Other dots and lines stand for the numerical results obtained by assuming the Lode angle θ of the ring shear at critical stress state are 10° , 20° and 30° , respectively.

shear tests were conducted to search for the correct Lode angle. With assumed Lode angle of 10° , 20° and 30° , the experiments obtained ϕ_c^{rs} was mapped to the corresponding ϕ_c^{tc} at $\theta = 30^\circ$. Note the calibrated parameters in previous sections are used for all simulations except the yet-to-be-calibrated exponent α . However, the exponent α only governs the peak stress state and has a trivial influence on the critical shear state used for calibration. A full 3D ring shear model was built with the same geometry and the same initial and boundary conditions in Abaqus. The stress state evolution was extracted at the shear zone and it was found their values matched with the stress state simulated from a simple shear test using a single element under plane strain condition. For the sake of computational efficiency, the single-element 2D simple shear model was used to perform all the numerical calibration simulations in this section. Note that this approach has already been utilized by Peng et al. [39] and yields reliable results. Figure 2.5 shows the predicted stress strength with different values of the Lode angle. For both samples, the numerical prediction (marked as blue circles) with the assumption of $\theta^{rs} = 20^\circ$ provides the best agreement with experimental measurements (marked as red 'x's). This agrees with the related study using the Modified Drucker-Prager/Cap model [12]. Using Equation 2.6, the mapped friction angle at triaxial compression stress state from the Schulze ring shear measured friction angle is $\phi_c^{tc} = 47.3^\circ$ for the *as-ground* sample and $\phi_c^{tc} = 49.6^\circ$ for the *engineered* sample, respectively.

Parameter: exponent α As explained previously, the G-B model uses the exponent α to govern the peak shear stress (i.e., shear strength), if the sample is densely packed at the initial state. Similar to the procedure of determining the Lode angle, the exponent α is also calibrated by trial-and-error using numerical simulations. The single-element 2D simple shear simulations were conducted with a suite values of α , over a physically reasonable range and compared the predicted peak shear stress to experimental data. Using the least-squares fitting method, it is found that $\alpha = 0.3$ provides the best fit for the *as-ground* sample while $\alpha = 0.4$ produces the best fit for the *engineered* sample, as shown in

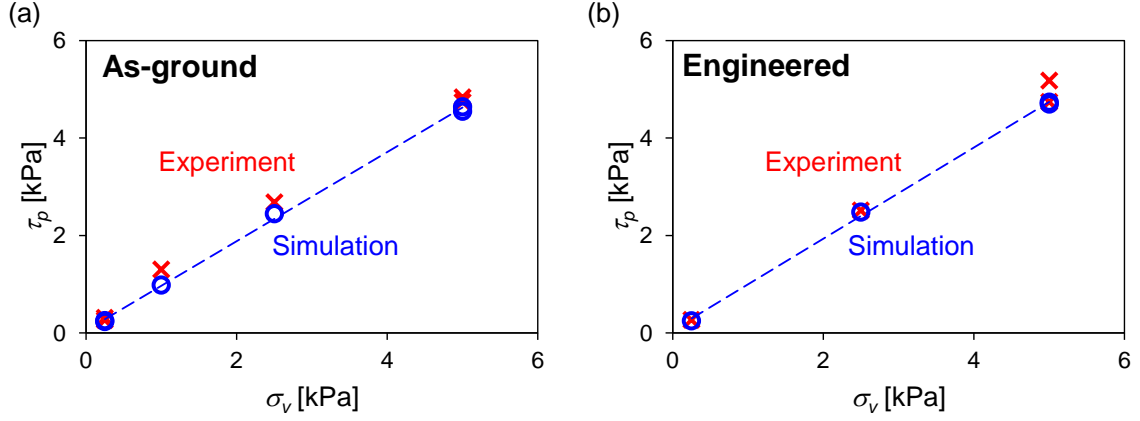


Figure 2.6: The relation of the peak shear stress τ_p against the vertical pressure σ_v from the ring shear test for the two samples. The red ‘x’s are experimental data, and the blue circles are numerical predictions using the calibrated α .

Figure 2.6.

2.3.4 Discussion on the material parameters

The calibrated material parameters for the G-B model are based directly on experimental measurements and indirectly on numerical simulations as summarized in Table 2.3. The large difference between the maximum and the minimum void ratios at zero pressure ($e_{i0} - e_{d0}$) in Table 2.3 indicates the high compressibility of the pine samples. The granulate hardness h_s for the ground pine samples is much smaller than that of granular soils (kilopascals compared to mega-pascals) and is also a reflection of the high compressibility of the ground pine samples.

The significant shear resistance of pine samples, which stems from the particle surface friction and inter-particle geometrical locking, is indicated by the high friction angle at the critical state, indicating shear strength is highly sensitive to compression. This phenomenon is partly because the coordination number (i.e., the number of contact points of each particle with neighboring particles) increases with increasing compression. More importantly, the high aspect ratio of the particles, as well as the compression-induced particle deformation, dramatically increases the cumulative area of the particle contacts. These two

Table 2.3: Calibrated G-B-hypoplastic model parameters for the two pine samples.

Pine sample	ϕ_c [°]	h_s [kPa]	n [-]	e_{d0} [-]	e_{c0} [-]	e_{i0} [-]	α [-]	β [-]
<i>As-ground</i>	47.3	187.6	0.30	0.50	1.06	1.38	0.3	1.0
<i>Engineered</i>	49.6	1034.6	0.35	0.59	1.19	1.42	0.4	0.5

factors combined with high surface roughness results in a high degree of inter-particle friction. These unique features result in the high shear strength of the ground pine chips and significantly influences the material flowability.

The void ratios (e_{d0} , e_{c0} and e_{i0}) of the *as-ground* sample are all smaller than those of the *engineered* sample due to the existence of fines. Similar phenomena have been observed by Youd [59]. In addition, the *as-ground* sample has a higher compressibility, reflected as a smaller value of granulate hardness h_s and a larger void ratio change due to compression (shown in Figure 2.2(b)), in comparison with the *engineered* sample. This phenomenon is also due to the existence of fine particles, which can move easily to fill in voids. Interestingly, the shear strength of the two samples is remarkably similar, despite the fact that fine particles have been removed from the *engineered* sample. A logical conclusion is that the fine particles likely have similar surface properties as the larger particles. The slightly lower shear resistance of the *as-ground* sample (as manifested by a slightly lower friction angle) is likely within experimental error, although a high content of fine particles could also slightly decrease the shear strength because shearing action tends to occur across fine particles.

2.4 Flowability in quasi-static regime

Campbell classifies granular flow into two broad flow regimes, elastic and inertial regimes, according to the existence (or lack) of force chains among the grains during the flow process [60, 61]. The elastic regime is further divided into two sub-regimes: quasi-static and inertial, based on whether the flow/no-flow boundary depends on the shear rate or not. The elastic-inertial regime is also known as the dense flow regime according to the solid

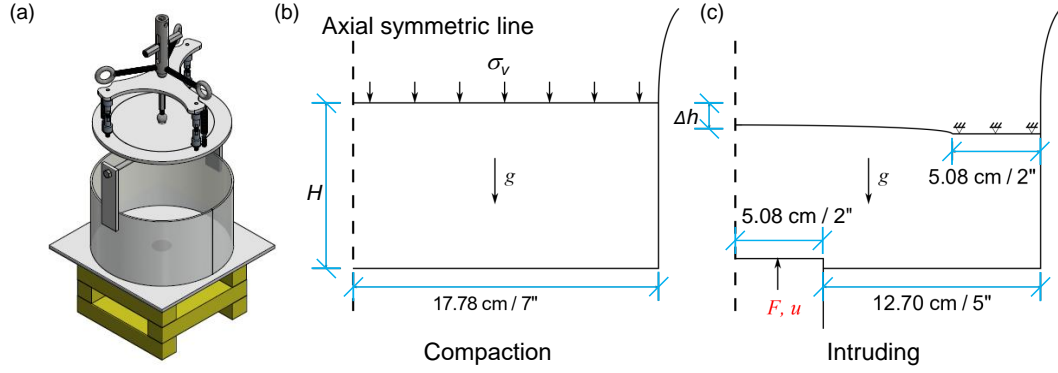


Figure 2.7: Geometry and boundary conditions of the axial shear test. (a) A schematic view of the test setup. (b) The boundary condition for the compaction step. (c) The boundary condition for the piston intruder.

volume fraction. For the material handling processes in biorefineries, the quasi-static and dense flow regimes are more common and are thus investigated in more detail below. To understand the shear behavior of the ground loblolly pine in the quasi-static flow regime, an axial shear tester was customized, and a suite of experimental measurements were conducted, and numerical simulations were performed to understand the shear pattern and to validate the G-B model with parameters calibrated in section 2.3.

2.4.1 Customized axial shear test

The customized axial shear tester is modified from the Johanson indicizer [62], and Figure 2.7(a) shows its schematic view. A fixed cylindrical container with a radius of 177.8 mm (7 inches) is designed with a hole at the center of the bottom plate. The hole has a radius of 50.8 mm (2 inches), which allows a piston intruder to be forced into the tester to deform the material. A lid is designed for applying vertical load and consists of two parts: an inner lid with a radius of 127.0 mm (5 inches) and an outer ring that fits loosely inside the cylindrical container. The experiment is performed by depositing pine chips into the container using the previously described “rain fall” method for a height H , followed by applying a uniform stress σ_v to the complete lid assembly to compact the material (Figure 2.7(b)). The outer ring is then fixed relative to the container, while the inner lid is

removed to unload a part of the material. During the final step, the entire test apparatus is fixed, except for the piston intruder, which moves upwards at a speed of 10 mm/min until a final intruding distance of 40 mm is reached (Figure 2.7(c)).

2.4.2 Physical experiments

During the experiment, the time-lapse intruding force is measured. F_i represents the intruding force and u_y is the height of the intruder that penetrates into the material. Figure 2.8 presents results from two typical tests with an initial sample height $H=95$ mm. For one test, a vertical pressure of $\sigma_v = 7.5$ kPa was applied during the first step, while zero pressure was applied during the first step for the other test (i.e. $\sigma_v = 0$ kPa). For the case of $\sigma_v = 7.5$ kPa, a smooth increase of reactive intruding force is observed and the intruding force reaches the peak F_i^p within 5-10 mm of intruding depth, and then the force gradually drops as the intruder continues moving upwards. Additional tests (not shown) in which different non-zero vertical pressures are applied for a range of different initial heights H exhibit similar trends, except for the magnitude of the peak force F_i^p differs. There are two components that contribute to the intruding force: 1) the gravity of the material that is generally shared across the bottom of the test cell before the intruder begins to move, and 2) a reactive force from the material's internal shear resistance. As the intruder begins to move, particles above the intruder are forced to move against the surrounding particles, and a substantial reactive force is generated. During this process shear bands form, and the local particle-level strength is overcome as the particles roll and detach. The bulk shearing of the material is accompanied by dilation along with the shear bands. At this stage, the reactive force reaches its peak value. After that, material deformation concentrates in the shear bands, and the reactive force decreases because the contact area within the shear band decreases. It can be observed that the lower bound of the intruding force is equivalent to the gravity of material directly above the intruder (shown in Figure 2.8).

For the case of $\sigma_v = 0$ kPa (i.e. without pre-loading) shown in Figure 2.8, the intruding

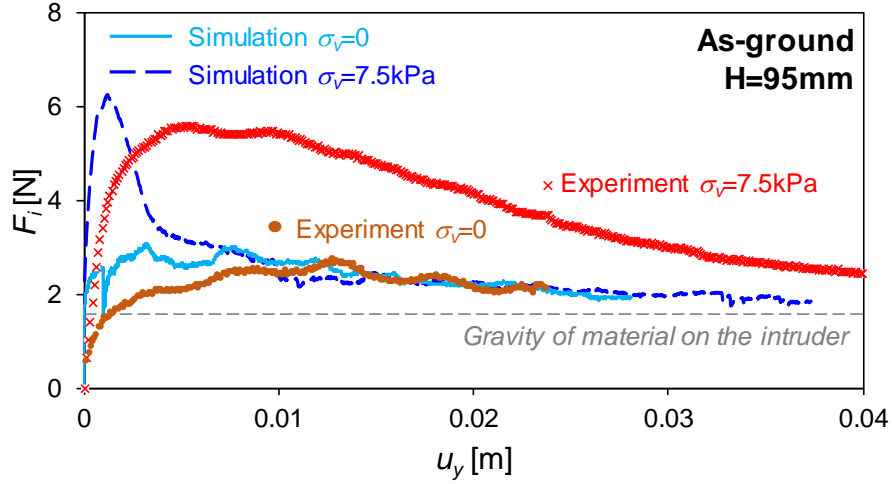


Figure 2.8: Comparison of time-lapse measured force on the intruder for the numerical simulation (lines) and physical experiments (dots). F_i denotes the intruding force and u_y denotes the intruder travel distance. For clarity, Only the data of the *as-ground* sample with height $H=95$ mm with vertical pressures $\sigma = 0$ and 7.5 kPa are presented. The gray dashed line represents the force of gravity from the material that is directly above the intruder.

force is significantly different from other cases with $\sigma_v \neq 0$ (i.e. with pre-loading). This phenomenon is primarily due to particle packing as discussed in subsection 2.3.4. The uncompacted specimen has a higher degree of void space, which allows the voids to redistribute and the particles to shear without forming stable force chains. The higher degree of void space in the uncompacted sample facilitates shearing action. As the particles slide past one another, the force chains (networks) that resist deformation change so that the force on the intruder fluctuates without experiencing an evident peak. The maximum force on the intruder appears later and has a lower value than in the case with $\sigma_v \neq 0$.

2.4.3 Numerical model setup and results

An axially symmetrical finite element (FE) model is constructed in Abaqus with the same geometry and initial and boundary conditions as the experiment. This model is shown in Figure 2.7, in which the container, the intruder, and the lids are all modeled as rigid bodies. A hard normal contact and a Mohr-Coulomb frictional shear contact with a friction angle 15° are used [12]. Note the initial void ratio is calculated from the measured bulk density

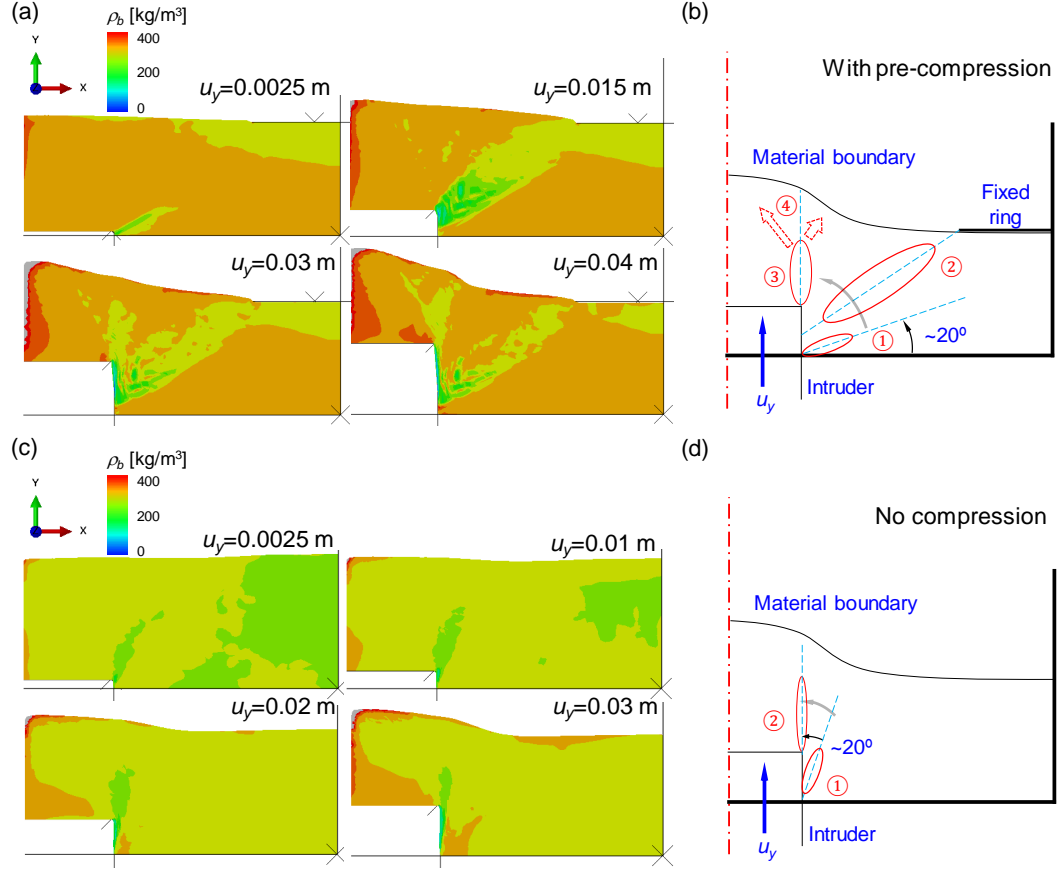


Figure 2.9: Modeling predicted shear zone development for the case of $H = 95$ mm and $\sigma_v = 7.5/0$ kPa. (a,c) Bulk density distribution during the intrusion step with and without pre-loading ($\sigma_v = 7.5$ kPa and $\sigma_v = 0$ kPa, respectively). The shear zones are manifested as local low-density regions. (b,d) Sketch of shear zone migrations for the case with and without pre-loading.

$e_0 = \rho_s/\rho_b - 1$, and gravity is applied before the compaction step. The G-B hypoplastic model with material parameters listed in Table 2.3 is used and the FE model is solved with the explicit solver.

An example of the predicted force on the intruder is included in Figure 2.8. The simulated axial shear test predicts a similar magnitude of the peak force F_i^p as the experiment for $\sigma_v = 7.5$ kPa, and the residual intruding force is bounded by the equivalent gravity of material directly over the intruder (dashed gray line). Yet, the predicted peak occurs earlier and declines more rapidly in the simulation than in the physical experiment. This discrepancy is mainly due to the fact that the G-B model is originally formulated for incompressible

sand particles. This conclusion is further explained in the discussion below.

As expected, the bulk density of both the precompacted and uncompacted samples is highly uniform in the vicinity of the intruder (near the center of the shear cell) as the intruder begins to move (see Figure 2.9(a) and (c)). Figure 2.9(a) and (c) also show that a shear band immediately begins to form for both samples at the outer edge of the intruder as it begins to move upward. For the precompacted sample, the G-B model predicts that a shear band quickly forms to connect the edge of the intruder to the inner boundary of the fixed ring, as indicated by the low-density region in Figure 2.9(a) at $u_y = 0.015$ m. The formation of this shear band with decreased bulk density and increased void ratio rapidly reduces the shear strength of the material and decreases the reactive force F_i on the intruder in Figure 2.8. Interestingly, Figure 2.9(a) indicates the formation of two separate shear zones as the intruder continues to move upward through the precompacted sample. The first shear zone continues to connect the outer edge of the intruder to the boundary of the fixed ring, while the other shear zone extends vertically above the edge of the intruder and is due to the shearing action of material directly above the intruder against adjacent material. As the intruder moves upward through the precompacted sample, the first shear zone shrinks, while the second one grows. The apparent evolution of the shear zones for the precompacted sample is sketched in Figure 2.9(b). The final state in which the dominant shear zone is vertical explains why the residual force on the intruder is slightly more than the weight of the material directly above the intruder.

The development of the shear zone is significantly different for the uncompacted sample ($\sigma_v \neq 0$) as shown in Figure 2.9(c). The only shear zone that forms is vertical at the outer edge of the intruder. This shear zone separates the material directly above the intruder from the remainder of the material. Because the mass of the material directly above the intruder does not change appreciably, the predicted force on the intruder does not change appreciably but only fluctuates as particles slide past one another, creating and destroying local force chains (networks). This behavior is evident in the experiment (brown dots in

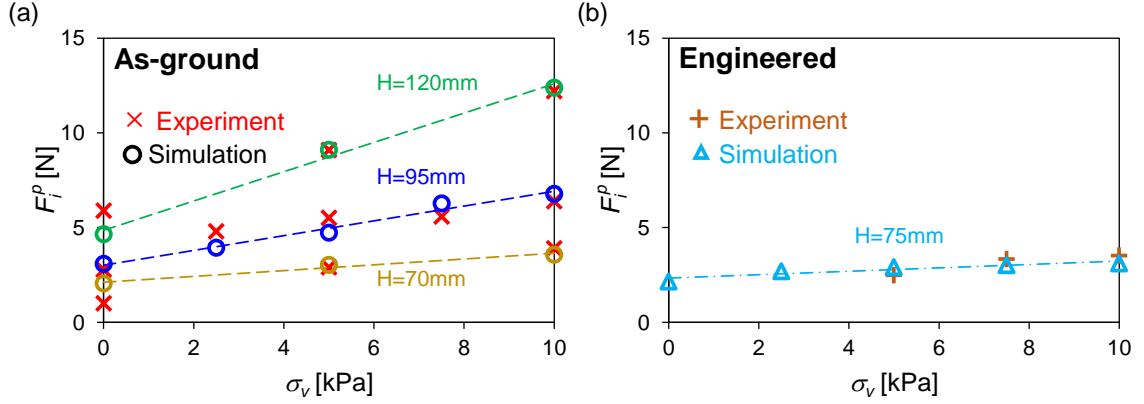


Figure 2.10: Comparison of peak force on the intruder F_i^p with different pre-loading pressures σ_v for the simulations and the physical measurements for the *as-ground* sample (a) and the *engineered* sample (b). H represents the initial sample height before compaction.

Figure 2.8) and is captured by the simulation (azure curve in Figure 2.8).

To test the ability of the G-B model to capture the key features of quasi-static flow, a suite of numerical analyses were performed for scenarios with different initial material heights H and different levels of pre-loading stress for the two samples. The peak intruding force F_i^p for each case is extracted and compared against physical measurements as shown in Figure 2.10. Extensive investigations of the influence of the time marching increment Δt , the upward velocity of the intruder, the mesh density and the pre-loading stress were carried out. The results indicate that consistent peak predicted forces on the intruder can be obtained with a proper combination of all three numerical factors. Figure 2.10 shows that the numerical predictions closely agree with the physical measurements across a range of parameters, indicating the G-B model can capture the key features of the quasi-static flow. The peak force on the intruder during the shear step linearly increases with increasing pressure in the prior compaction step, in agreement with physical measurements. This result shows that the G-B accurately captures the dependence of material shear strength upon the stress history. These results are remarkable because other continuum modeling approaches, such as M-C based methods are unable to realistically capture stress history impacts [12]. It can also be observed that the peak force increases non-linearly with increasing sample height at the same level of compaction, and the numerical model successfully captures this

trend as well.

2.4.4 Discussion on particle stiffness

Similar to the axial shear tests, the G-B model simulated ring shear tests also predict that the peak and the critical shear stresses occur at much smaller strain levels as compared to physical experiments (Figure 2.5(a)). Yet, the magnitude of the peak shear strength τ_p and the critical state shear stress τ_c , similar to the peak intruding force F_i^p , are not significantly affected by the particle stiffness.

In addition to the critical state achieved at high strain levels, the low particle stiffness of pine chips also results in different evolutions of shear stress and density distribution (Figure 2.5(a)). As noted above, pine chips require greater rotational displacement to reach maximum shear stress compared to materials with rigid particles. In addition, the material density can reach a maximum even when the shear stress does not [12]. As shown in Figure 2.5(a), three types of shear behavior can be identified: 1) under-compacted shear in which the particles compress as they shear, which results in an increase in both shear stress and density; 2) over-compacted shear in which samples dilate as they shear causing existing force chains to be replaced with weaker force chains as the sample shears. This process results in the formation of shear bands in which density decreases as shear stress increases. 3) Critical state shear in which the amount of particle contacting pairs with shear squeezing (particle level contraction and increasing friction) is balanced with shear dilation (particle level roll over and decreasing friction), such that the density and shear stress are both constant over time.

Soft granular materials (e.g., pine chips) require large shear strains to achieve critical/steady state. This feature challenges characterization methods that do not allow infinite strain, such as tri-axial testers, as well as granular flow models that need to be calibrated from these finite-strain testers. This limitation can be overcome using a combination of standard laboratory tests and numerical simulations, as demonstrated in section 2.3.

2.5 Flowability in dense regime

2.5.1 Numerical modeling and validation

In order to further evaluate the performance of the G-B model in capturing the flow behavior of ground loblolly pine in the dense flow regime, numerical simulations were performed of material flow in a wedge-shaped hopper and compare prediction against physical measurements. Modeling granular material flow through a hopper is numerically challenging using continuum mechanics based-methods. The large deformation experienced by the material can induce mesh tangling for the Lagrangian mesh based finite element method (FEM). The Coupled Eulerian-Lagrangian (CEL) method was used to address this numerical issue. In the CEL method, the material flowing through the Eulerian-fixed mesh is tracked by the volume percentage in each element. Namely, each Eulerian element is occupied by both material and “voids” quantified by their volume fractions. The interaction between the Lagrangian elements (e.g. the hopper wall) and the Eulerian elements (e.g. the pine chips) is realized by a general contact based on a penalty algorithm.

The cross section of the wedge-shaped hopper with a bin, which is used to experimentally characterize the dense flow behavior of loblolly pine chips, is shown in Figure 2.11(a). The length of the hopper wall and the height of the bin are both 0.6 m. The hopper opening width W can be adjusted by changing the length of the wall (i.e. sliding along the blue arrows in practice). The inclination of the hopper is measured by the semi-angle μ as shown in Figure 2.11(a), and a fixed $\mu = 30^\circ$ is used in this chapter. The size of the system in the direction perpendicular to the cross section is 0.4 m, which provides plane strain conditions for the material inside the hopper. In addition, it can be observed that the flow pattern is symmetric with respect to the central surface. Accordingly, a half slice of the cross section with a thickness of 25 mm was modeled to reduce computational cost. A fixed displacement boundary condition in the direction out of the plane is applied to the two surfaces parallel to the plane. And a symmetrical boundary condition is applied to the

symmetrical surface. The hopper wall is modeled as a rigid body, and a wall friction angle of 8.5° is adopted for all simulations in accordance with experimental measurements.

The physical hopper flow experiments were conducted by 1) sliding the hopper wall to close the outlet, 2) charging the hopper-bin system with *as-ground* pine sample to the targeted total height of 0.68 m, which is measured vertically from the tip of the hopper to the top surface of material, 3) sliding the hopper wall to the targeted opening width to initiate the flow, 4) logging the cumulative mass m_t collected at the bottom of the hopper with a scale. The measured cumulative mass discharged from the hopper is linear with respect to discharging time (marked as red 'x's in Figure 2.11(c)) for all tested cases.

Instead of explicitly modeling the hopper wall sliding action to open the hopper outlet, the outlet width is fixed and zero vertical displacement at the outlet is assigned. The charging process is modeled by applying gravity to the elements with material assigned. Once the internal stress of the material is in equilibrium, the fixed displacement boundary condition at the hopper outlet is replaced by a Eulerian free flow boundary to initiate flow. During the flowing step, the nodal velocity located at the outlet surface and the density of elements with one face constituting the outlet surface at each time increment are tracked. The values of nodal velocity and element density are then used to calculate the average mass flow rate of each element q_m . The extracted data show that the density and the velocity are uniformly distributed along the direction of thickness, which confirms the plane strain assumption. The velocity, the density, and the flow rate profiles, averaged in the thickness direction, along the outlet cross-section are plotted in Figure 2.11(b) for the case of $W = 60$ mm at time $t = 6$ s. Note that the velocity, the density, and the flow rate using their respective maximum values in the plot are normalized. The trends of the three parameters are similar even with different flow steps and different outlet widths. The total mass flow rate through the outlet \bar{q}_m is calculated by numerically integrating the flow rate profile.

Figure 2.11(c) shows the total discharge mass m_t as a function of time (marked as the

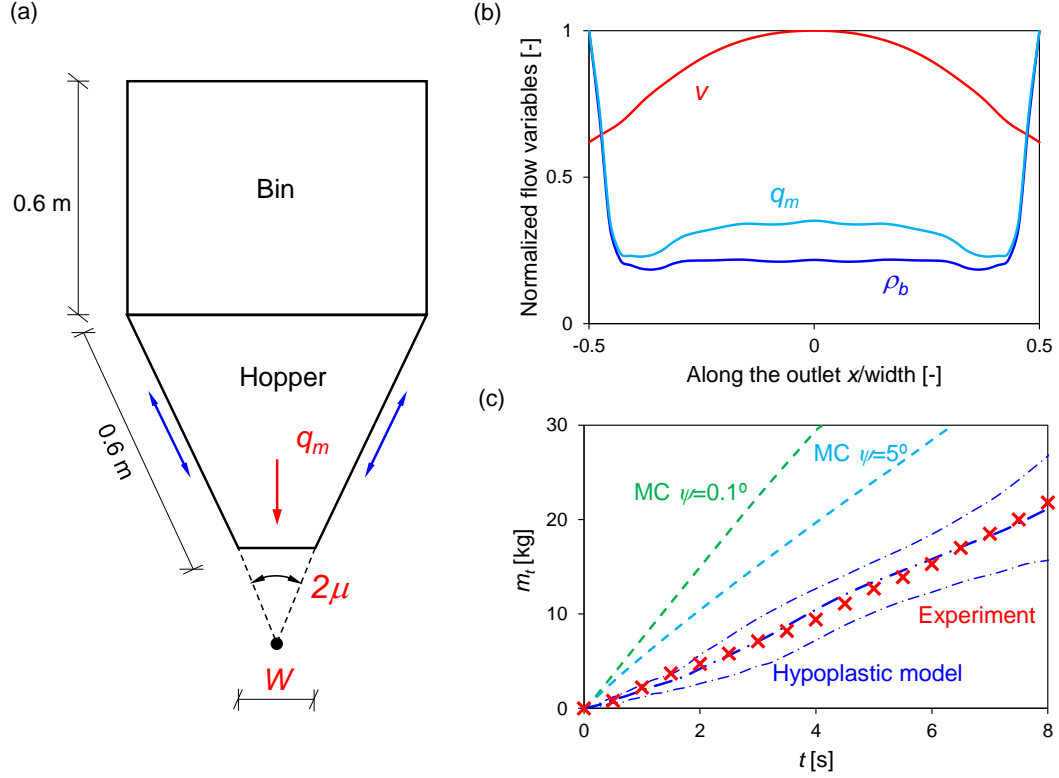


Figure 2.11: (a) Geometry of the wedge-shaped hopper with an upper bin for both the numerical simulation and the physical tests. The outlet size is controlled by sliding the hopper walls. (b) Normalized representative flow rate q_m , bulk density ρ_b , and velocity v profiles along the width of outlet. (c) Comparison of predicted cumulative mass discharged m_t from the G-B model (dot-dashed lines) and the M-C model (dashed lines) against experimental measurements (red 'x's) for $W = 60$ mm and $\mu = 30^\circ$.

dot-dashed line in blue) for a hopper outlet width of $W = 60$ mm and a semi-angle of $\mu = 30^\circ$ as predicted by the G-B model. Recall the forward Euler integration is used to implement the G-B model (subsection 2.2.2), which results in that the predicted total discharge mass depends on the time increment size Δt . The three dot-dashed lines represent respectively the maximum, the mean, and the minimum total discharge mass predicted by the G-B model simulations, with Δt ranging from $1 \mu\text{s}$ to $20 \mu\text{s}$. Time-marching increments outside this range suffer from either convergence issues or heavy computational costs. In addition to the G-B model, the popular Mohr-Coulomb model was also used to perform the hopper flow simulation with the same geometry and boundary conditions. A friction angle of 39.2° is used for the Mohr-Coulomb (M-C) model for the *as-ground* pine sample. This

value is obtained directly from Schulze ring shear tests (Figure 2.5). Elasticity parameters are adopted from Jin et al. [12]. The only unknown parameter is the dilation angle ψ , which is assumed to be 0.1° or 5° , given that the material is not densely packed (no compaction after charging step) and will not dilate significantly upon shear. The cumulative mass discharges predicted by the M-C model m_t are presented as dashed lines in Figure 2.11(c). Both of the two M-C predictions significantly overestimate the mass flow rate measured from physical experiments (red 'x's). This result exemplifies why hopper designs based on the M-C model do not achieve design flow rates biomass refineries. The complex flow behavior of ground loblolly pine cannot be captured by the simple M-C model. In comparison, the results predicted by the G-B model match well with experiments, indicating that the G-B model with calibrated parameters can qualitatively and quantitatively characterize hopper discharge flow behavior for ground loblolly pine.

2.5.2 Effects of outlet size and wall friction

Hopper outlet width is a critical parameter to control the flow rate and to avoid the hopper bridging issue. In order to evaluate whether the G-B model is capable of capturing the effects of outlet width on the discharge flow response, a suite of simulations with different outlet widths are performed. The predicted average mass flow rates (\bar{q}_m blue circles) are compared against experimentally measured data in Figure 2.12. Note the semi-angle is fixed at $\mu = 30^\circ$. The uncertainty bars of the numerical prediction represent the effect of the time increment Δt , due to the forward Euler integration method, as explained previously. All the simulation data points as well as the trend lines are bounded within the $\pm 20\%$ uncertainty boundaries of the experimental measurements. These results validate that the G-B model, with calibrated material parameters, can capture the flow behavior of ground loblolly pine within the dense flow regime.

Hopper wall friction angle is another critical design parameter that can influence the material discharge behavior. an additional suite of numerical simulations were conducted

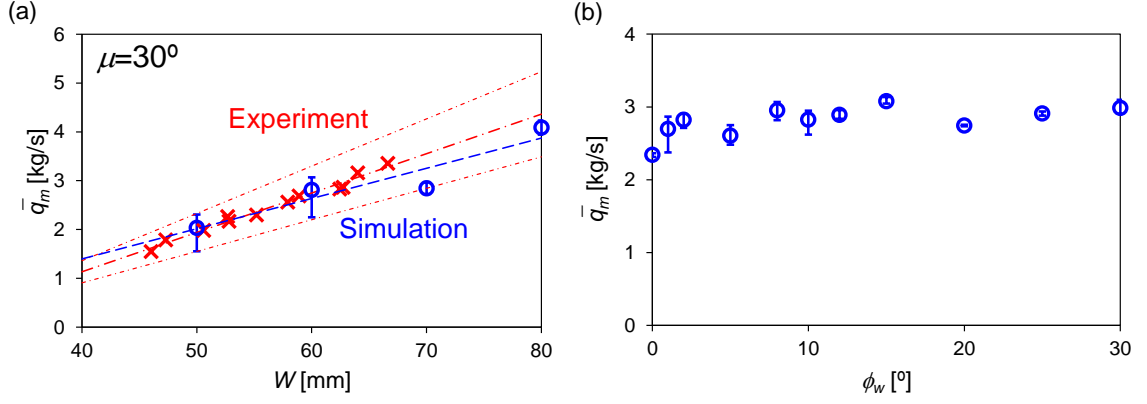


Figure 2.12: (a) Comparison of predicted average mass flow rates (blue circles) for different hopper outlet widths W to physical measurements (red 'x's'). The dot-dashed lines in red represent $\pm 20\%$ -error boundaries. (b) Predicted average mass flow rate from the numerical model as a function of wall friction angle. Uncertainty bars on the numerical results represent the standard deviation due to a reasonable range of time increment sizes Δt .

with the wall friction angle ϕ_w ranging from 0° (smooth surface) to 30° (rough surface) with a fixed hopper semi-angle of $\mu = 30^\circ$ and a hopper width of $W = 60$ mm. The predicted average mass flow rate \bar{q}_m as a function of wall friction angle ϕ_w is plotted in Figure 2.12(b). The flow rate is sensitive to the wall friction angle when its value is less than 3° and remains statistically constant at 3 kg/s for wall friction values greater than 3° . The Schulze ring shear tester measured the friction angle between the steel wall and pine chips to be in the range 12-18 degree [12], indicating the effect of the wall friction on the magnitude of flow rate is trivial. However, the simulated results show that the wall friction has a significant influence on the flow pattern within the hopper. As shown in Figure 2.13, a small wall friction angle ($\phi_w = 8.5^\circ$) yields a mass flow pattern in which material at the same height tends to flow at approximately the same speed. A high wall friction angle ($\phi_w = 30^\circ$) produces funnel flow in which material at the center of the hopper tends to move faster than material closes to the wall.

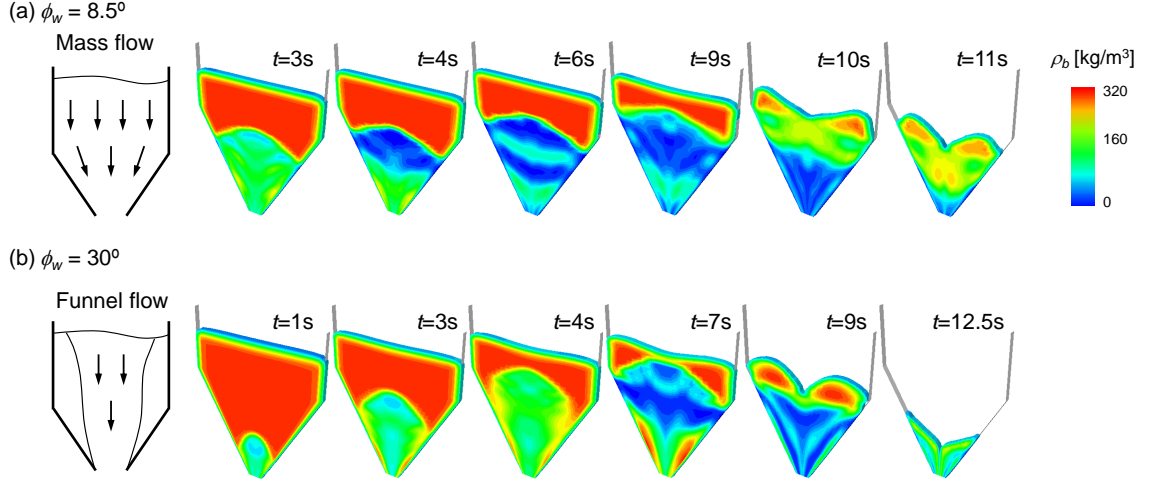


Figure 2.13: Predicted flow pattern with wall friction angle $\phi_w = 8.5^\circ$ (a), and with wall friction angle $\phi_w = 30^\circ$ (b).

2.6 Conclusions

An integrated numerical and experimental investigation was carried out to address the poor flowability issue of a widely used biomass feedstock, ground loblolly pine. The Gudehus-Bauer (G-B) hypoplastic model was first implemented into the Abaqus user subroutine and the implementation was validated with a single-element simulation of oedometer tests. The G-B model parameters for two ground pine samples were calibrated using standard laboratory equipment (including a load frame but not a tri-axial tester). Model parameters are either directly obtained from index tests, the Schulze ring shear test, and an oedometer test, or indirectly obtained by modeling those tests. With calibrated material parameters, the G-B model is further used to simulate a customized axial shear test in a quasi-static flow regime and a hopper flow test in a dense flow regime. Simulated results are compared against experimental measurements. The key conclusions from this work can be summarized:

1. The traditional characterization methods suffer from either incomplete stress state measurement (ring shear tests) or limited strain range to achieve steady/critical state (triaxial shear tests) for biomass materials with high compressibility and high shear

resistance. The stress state of ground pine chips can be characterized using a combination of relatively simple laboratory tests and numerical simulations.

2. The customized axial shear test and the hopper test are effective approaches to characterize the flowability of particulate materials in multiple flow regimes, and can serve as good validation tools to evaluate the capabilities and limitations of numerical models.
3. Advanced finite element method (e.g. CEL) with the G-B hypoplastic model is a valid tool to predict the flow behavior at both the quasi-static and the dense flow regimes for ground loblolly pine. The discrepancy between experimental and simulation results is most likely due to the incapability of the G-B hypoplastic model to capture particle deformation. However, such discrepancy does not influence the prediction of key metrics of ground pine flowability because the compressible particles are not deformed significantly during the critical state flow.
4. Experimental measurements and numerical predictions both reveal that the mass flow rate of ground loblolly pine in the wedge-shaped hopper linearly increases with the hopper width. And numerical modeling indicates that the wall friction angle is one of the key parameters to control the flow pattern, yet, its influence on flow rate is insignificant. Sensitivity study of wall friction, wall inclination, and material parameters on flow patterns, bridging mechanisms will be pursued in the future study.

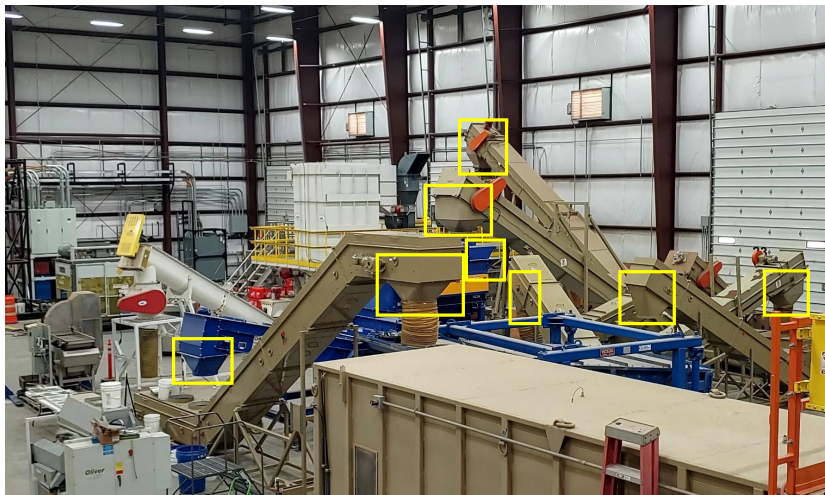
CHAPTER 3

FLOW AND ARCHING IN WEDGE-SHAPED HOPPERS

3.1 Introduction

The commercialization of lignocellulosic biomass as an energy source has been substantially limited by its poor flowability, which often results in dramatic issues during bulk solids handling, for example, hopper arching, ratholing, and screw feeder jamming [4, 8, 10, 9, 11, 63]. Figure 3.1(a) demonstrates the wide application of hopper (marked with yellow boxes) in the transportation of biomass feedstock in a typical biorefinery, and Figure 3.1(b) shows woody biomass material arching in a wedge-shaped hopper. The current operational reliability of a biorefinery is only 30%, which is far away from the goal 90% required by the U.S. Department of Energy to achieve the target cost of \$3.00 per gallon of gasoline [4, 64].

(a) Biomass material Process Development Unit



(b) Arching in wedge-shaped hopper

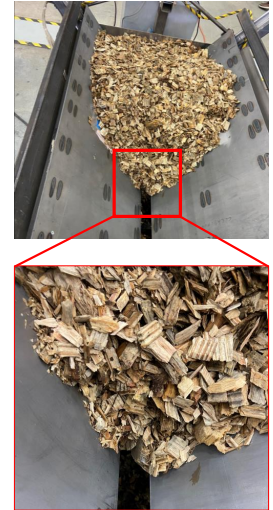


Figure 3.1: (a) A biomass material Process Development Unit at Idaho National Laboratory, Idaho Falls, ID, USA. Hoppers are marked out in the yellow boxes. (b) An example of woody biomass material arching in a wedge-shaped hopper.

The leading reason for these handling problems is the poor understanding of the gran-

ular biomass flow behavior. Comparing to conventional granular particles (e.g., sands), granular biomass particles have low particle density, high aspect ratio, high compressibility and high shear resistance. These unique characteristics, manifested through their porous microstructure and complex surface morphology, make the bulk flow behavior challenging to be characterized experimentally and theoretically [65]. In experiments, the standard characterization tests suffer from either a limited strain range to reach the critical shear state (e.g., tri-axial shear test) or inadequate measurement of full stress state (e.g., ring shear test) for granular biomass materials [65, 13, 17, 24]. In theory, the classical constitutive models (e.g., Mohr-Coulomb, Drucker-Prager), proven to be able to capture the flow behavior of conventional granular materials, fail to represent the mechanical behavior of granular biomass materials [12, 32]. Yet, the design of biomass material handling equipment still uses incompetent experimental methods and theoretical models, which results in material processing upsets in biorefineries. Take the most used material handling equipment, hopper/silo, as an example, its design is still guided by Jenike and colleagues' early work in the 1960s [66, 26, 67]. The design method has been experimentally and numerically demonstrated that it conservatively overestimates the critical outlet size of hopper/silo for various granular materials [68, 69, 70, 34]. However, the hoppers/silos, designed by following this method, constantly experience arching/bridging in biorefineries, indicating the critical outlet width is underestimated [17, 7].

Hopper arching is a classical challenge in bulk solid handling, a significant amount of experimental and numerical studies have been conducted in literature. One of the focuses of these studies is the determination of the hopper critical outlet width for various materials (e.g., rocks, coals, ores, pharmaceutical particles, and ideal spherical beads) [70, 71, 72, 73]. Experimental characterization of a specific granular material is the most direct way to understand the flow behavior and quantify the critical outlet width. Yet, limited by the sensors on the hopper, experiments can only measure global flow response (e.g., flow rate, flow pattern), cannot track the strain-stress behavior within the material. In addition,

experiments at the industry-scale with a comprehensive test plan are not economically viable. Numerical simulations, with models validated by experiments, can address the experiment limitations listed above. For the hopper arching problem, both the Discrete Element Method (DEM) and the Continuum Mechanics-based Finite Element Method (FEM) have been utilized. DEM explicitly models the particle and has been proved suitable for investigating the granular interaction near the hopper outlet [74, 75]. Yet, DEM is not capable of modeling the large-scale hopper flow due to its non-affordable computational cost even with the current super-computing resources [76, 29]. Without heavy computational burden, advanced FE Methods with a valid constitutive law have been successfully utilized to study the arching behavior in hoppers [34, 77]. Most of these experimental and numerical studies focus on conventional granular materials (e.g., sands, pharmaceutical particles), and investigation on hopper arching for granular biomass material is missing.

To fill the knowledge gap on the flow behavior of biomass feedstock in a hopper, physical experiments and numerical simulations are combined in this chapter to understand the effect of the critical material attributes and the critical processing parameters on hopper flow. A customized hopper with adjustable inclination angle and outlet width is used for experimental investigation. The critical state theory-based hypoplastic model, calibrated and validated for ground loblolly pine [65, 12], is adopted as the constitutive law. Focused on flow performance in mass flow rate and hopper arching, the development of a Coupled Eulerian-Lagrangian (CEL) FEM model is first presented with its validation against the hopper flow experiment. Flow and arching affected by hopper inclination angle and opening size are investigated experimentally and numerically in the following. Systematic analysis of the influences of material packing, particle density, and hopper filling height or surcharge on flow performance are conducted. This chapter sets a foundation for the construction of a novel design method for flowing granular biomass material in a hopper.

3.2 Methods

3.2.1 Granular pine samples

The granular material used in this chapter is ground loblolly pine. The detailed description of the sample are reported in subsection 2.3.1 and the previous work [65, 12]. The particle size distribution ($d_{10}=0.38$ mm, $d_{50}=0.82$ mm, $d_{90}=1.79$ mm) is obtained by the sieve analysis and shown in Figure 3.2(a) with a photo presenting the particle size and shape. Note that the dashed line is empirically extrapolated due to the lower limit of the sieve screen.

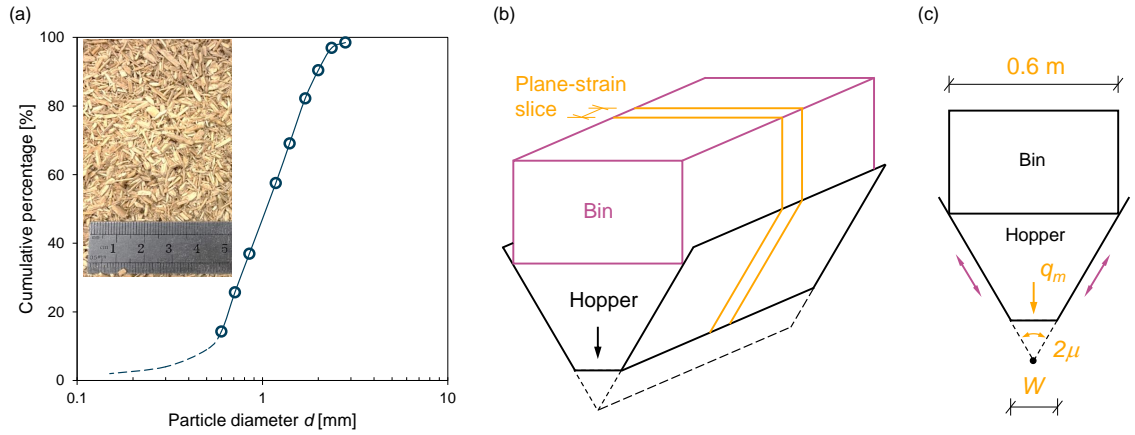


Figure 3.2: (a) Particle size distribution of the sample and a photograph presenting particle size and shape. The dashed line is empirically extrapolated due to the lower limit of the sieve screen to measure the particle size. (b) A schematic view of the experimental setup: a wedge-shaped hopper extended with an upper cuboid bin. The numerical model is constructed using a slice with a finite thickness of 25 mm based on the plane strain condition. (c) The geometry and boundary conditions of the pseudo-3D numerical model. Note the outlet size is adjusted by sliding the hopper walls.

3.2.2 Experimental setup

¹ A customized wedge-shaped hopper attached with a cuboid bin at the top, as shown in Figure 3.2(b), was used to perform all the flow tests. Equipped with stepper motors, rack and pinion gearing on both sides, the hopper walls on both sides are capable of sliding as well as rotating through hand wheels and threaded supports at the top, which allow

¹The experimental work in this chapter were conducted by the Idaho National Laboratory.

us to adjust hopper inclination and outlet size. The walls were synchronized and moved together to either a fixed position for measuring the discharge rate or were incrementally opened to measure the critical outlet width. Figure 3.2(c) shows the 2D hopper geometry from the axial direction. The width of the bin is fixed as 0.6 m, and the length of the wall is adjustable by sliding according to different hopper inclinations and outlet widths. The half of the angle between the two walls is denoted as the hopper inclination angle μ (Figure 3.2(c)), and W is used to denote the hopper outlet width.

For each test, the hopper wall is adjusted to a specified inclination angle and is closed initially ($W = 0$). Granular biomass feedstock with a fixed mass M is loaded into the hopper and the bin. The flow test was initiated by sliding the wall until the hopper outlet reaches a preset opening width W . A balance with a readability of 5 g is placed below the outlet to measure the cumulative hopper discharging mass m_t against time. A typical $m_t - t$ response is shown in Figure 3.3(a) as the yellow ‘ \times ’s. The mass flow rate q_m was calculated as the slope of the curve during the discharging period after eliminating the two ends of inception and decay.

In addition to quantifying the mass flow rate, the critical outlet width W_{cr} was also measured. Similar to the previous description, the hopper was first loaded with the biomass feedstock. Then, the outlet gate was opened about 1 mm by sliding the wall and hold for 30 s to observe the flow/no-flow conditions. The open-hold process was repeated with the outlet width increased around 1 mm each time, and the process was stopped when a steady hopper flow is observed. The critical outlet width W_{cr} is calculated as the average of the outlet widths before and after the steady flow and at the center line (axial direction) of the hopper opening.

3.2.3 Numerical modeling

Reliable modeling of the flow of the highly compressible granular biomass material is challenging for both particle-based methods (e.g., DEM) and continuum mechanics-based

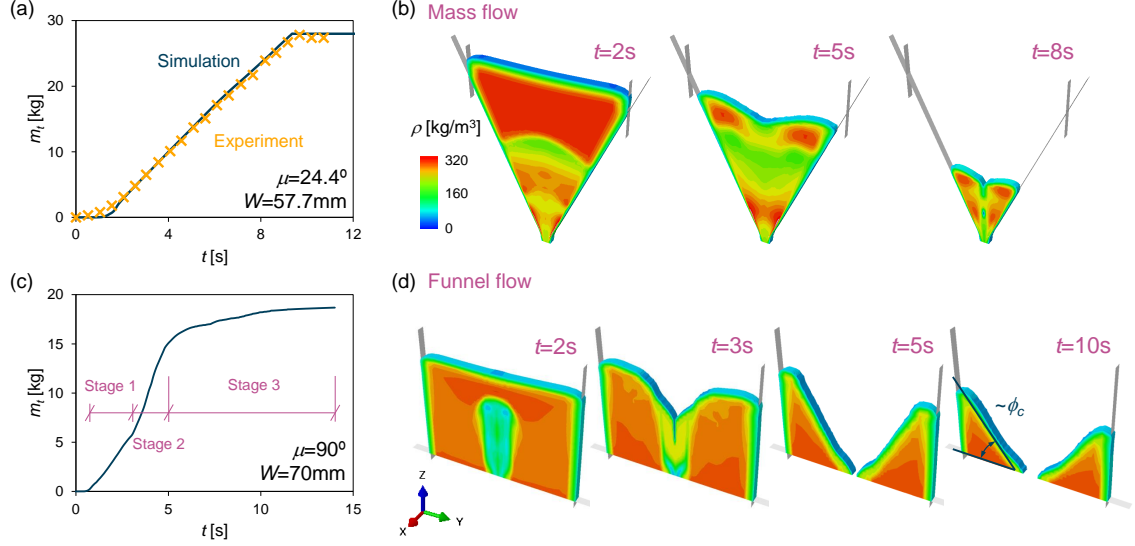


Figure 3.3: Numerical model validation and predicted flow response for a hopper (low inclination angle) and a silo (high inclination angle). (a) Comparison of simulation predicted cumulative mass discharged m_t against experimental measurements for outlet width $W = 57.7$ mm and hopper inclination $\mu = 24.4^\circ$. (b) Flow pattern demonstration superposed with density distribution for the case in (a). (c-d) Typical flow response of a silo (flat-bottom hopper) with outlet width $W = 70$ mm and inclination $\mu = 90^\circ$.

methods (e.g., FEM). For DEM, the computational cost and the quantification of the particle-level contact behavior limit its application [28]. For FEM, mesh tangling is difficult to handle for large deformation, and high-fidelity constitutive models across flow regimes do not exist yet [32, 12]. The constitutive models (e.g., the classical Mohr-Coulomb model) used for hopper flow simulation in literature [78, 35, 34, 36] cannot capture the compaction (respectively, dilation) induced hardening (respectively, softening) exhibited by the loblolly pine chips. The recent work on the modeling of granular biomass material flow using an advanced FEM (i.e., the Coupled Eulerian-Lagrangian (CEL) approach), and the Gudehus-Bauer hypoplastic model [45, 46] shows the above limitations can be circumvented with promising results [65]. The CEL approach constitutes two steps: 1) a Lagrangian mesh is attached to the material and it deforms with the material using the conventional FEM; 2) the mesh is returned to its original position (i.e., fixed mesh in a whole increment) and the deformed material with its properties are interpolated back onto the “fixed” mesh. This two-step scheme enables CEL capable of modeling large-deformation flow simulations.

The G-B hypoplastic model incorporates critical state theory and utilizes void ratio to characterize the density-dependent flow behavior. With these features, the CEL approach and the G-B model are used for simulating the complex flow behavior of compressible biomass materials in this chapter.

The formulation, implementation and validation of the G-B hypoplastic model in Abaqus User Material Subroutine (VUMAT) are described in the previous study [65] and open-sourced in Github. A workflow to calibrate the G-B model parameters for ground loblolly pine by combining lab characterization experiments and numerical simulations were also provided. Briefly, the eight parameters in the G-B hypoplastic model are: 1) the minimum, the critical, and the maximum void ratios at zero pressure e_{d0} , e_{c0} and e_{i0} , 2) the granulate hardness h_s , exponent n and β , which closely relate to material compressibility, and 3) the internal friction angle at the critical state ϕ_c and exponent α , which determine the shear stress at the critical and the peak states, respectively. The calibrated material parameters are listed in Table 2.3 as the as-ground sample.

Figure 3.2(c) shows the cross-section of the CEL numerical model. Its geometry is exactly the same as the experimental set-up with fixed bin width as 0.6 m. Similar to the experiments, the hopper outlet width W is adjusted by sliding the hopper wall. A plane strain condition is observed in the experiments with the axis direction perpendicular to the 2D surface shown in Figure 3.2(c). Given both the geometry and the boundary conditions are symmetric with respect to the central surface of the two hopper walls, only a half slice of the cross-section with a finite thickness of 25 mm is simulated for the sake of computational efficiency. Except for the walls, symmetric boundary conditions are applied to the planes with normal direction out-of-the-plane and to the symmetric central surface. The hopper walls and the bin are modeled as rigid bodies, with a “hard contact” using the penalty method in the normal direction and a Coulomb frictional contact in the tangential direction. Experimentally determined friction angle 8.5° between the wall and the pine chips is used for all the simulations. A structured hexahedron mesh is used with an average size of 15

mm within the hopper cross-section plane and 5 mm in the axial direction. Constrained by the mesh size (i.e., large mesh distortion and computation efficiency), the time step of 2-20 μs is used for all simulations. The experiments were modeled using two steps: 1) after the Eulerian meshes are charged with material, the gravity was applied with a smooth step function followed by rest until the internal stress of the material reaches equilibrium, 2) the flow was initiated by sliding the hopper wall from the closing state to the preset outlet width W .

Similar to the experiments, the mass flow rate q_m and the critical outlet width W_{cr} were quantified for each simulation. For the mass flow rate q_m , the nodal velocity and the elemental density for all the outlet elements are extracted. Through integration over the outlet surface and time, the predicted accumulative mass discharged is plotted against time shown in (Figure 3.3(a)). The computed average mass flow rate q_m is the slope of the $m_t - t$ line. For the critical outlet width W_{cr} , the Dichotomy method is used by trying two different outlet widths W and gradually narrowing the range of upper and lower bounds until a dramatic change of flow responses is observed with 2 approaching outlet widths (e.g., $W = 20$ mm and 21 mm in Figure 3.4). Another method to obtain W_{cr} is also presented. After the simulated mass flow rates against different outlet widths are plotted, the data points ($q_m - W$) is extrapolated with a line, and denote the intersection point across the line and the horizontal axis as the W_{cr} . The validity of the second method is approved as its predicted W_{cr} is almost the same as the value directly simulated through the Dichotomy method. Details on this method are presented in subsection 3.4.1.

3.2.4 Model validation

The numerical model was validated by comparing the model predicted cumulative discharged mass m_t against the experimental measurements, as shown in Figure 3.3(a) with a hopper inclination angle 24.4° and an outlet width 57.7 mm. In addition, a series of simulations are performed to obtain the mass flow rate q_m variation with different outlet width

W at hopper inclination angles 24.4° , 30° and 36° . The match between the numerical prediction and the experimental measurements for all these cases (subsection 3.4.1) validates the numerical model. It is worth noting that the numerical model developed in this chapter significantly outperforms the one in the previous study [65] (chapter 2), which realizes the opening of the hopper through the Eulerian boundary condition instead of sliding the walls.

3.3 Results

3.3.1 Flow response

Figure 3.3(a) and (c) respectively present the modeling predicted variation of cumulative discharged mass m_t against time t for a slender hopper with $\mu = 24.4^\circ$, $W = 57.7$ mm and a flat-bottom hopper with $\mu = 90^\circ$, $W = 70$ mm. For most of the hoppers with low inclination angle (which is denoted as slender hoppers), the predicted $m_t - t$ flow response is a straight line, which implies the hopper flow is in a steady state and the mass flow rate is a constant. The overall flow section in $m_t - t$ response is used to calculate the slope as the mass flow rate q_m . The corresponding remaining material at time $t = 2$ s, 5 s, 8 s superposed with density are shown in Figure 3.3(b). Recall that a relatively small wall friction angle (i.e., a smooth wall) is used, the predicted flow has a typical *mass flow* pattern: material at the same height tends to move simultaneously at a similar velocity.

For the flat-bottom hopper (also called silo), a typical *funnel flow* pattern is observed: material above the outlet tends to flow out first and a vertical flow channel is formed as shown in Figure 3.3(d). The predicted $m_t - t$ response is not a straight line, and it can be divided into 3 stages (Figure 3.3(c)): 1) the material right above the outlet drops out ($t = 2$ s in Figure 3.3(d)); 2) the material near funnel surfaces starts to collapse and flow towards the outlet, the overall material height gradually decreases in this stage ($t = 3$ s in Figure 3.3(d)); 3) the toes of the funnel surfaces touch the outlet and the flow rate q_m dramatically decreases ($t = 5$ s in Figure 3.3(d)), less and less material flow out of the outlet until it fully stops with residual material retained within the silo ($t = 10$ s in Figure 3.3(d)).

According to the observation, the mass flow rate q_m is calculated from the slope of the Stage 2 $m_t - t$ response. After the material fully stops flowing, the angle between the surface of the residual material and the bottom surface of the silo is measured. It was found that this angle fluctuates around the critical state internal friction angle ϕ_c . The physical mechanism of the residual material formation inside the silo (i.e., internal material friction) is the same as the formation of the pile for the angle of repose experiment. Note the magnitude of the angle of repose is around ϕ_c [48, 79]. The agreement between the residual material slope angle and the critical state internal friction angle further validates the numerical model.

3.3.2 Arching

As described in the subsection 3.2.3, the critical outlet width W_{cr} is obtained by the Dichotomy method. Figure 3.4(a) shows the variation of cumulative discharged mass with time for the hopper with a fixed inclination $\mu = 24.4^\circ$ and three different outlet widths $W = 19, 20, 21$ mm. For the cases of $W = 19$ and 20 mm, almost zero flow rates are predicted. While for the case of $W = 21$ mm, a large flow rate can be observed. This indicates the W_{cr} around 20.5 mm with a ± 0.5 error bound. Note that the continuum mechanics-based model cannot predict a complete stop of material (Figure 3.4(a)). Yet, the almost zero value of the mass flow rate indicates arching is realized.

The predicted density ρ , vertical velocity v_z , and normalized friction ratio M/M_c (Figure 3.4(b-d)) were further compared for the hoppers with $W = 19$ and 21 mm at time $t = 8$ s. Figure 3.4(b) shows that the material in the arching hopper ($W = 19$ mm) is compacted and forms a high-density region near the outlet, while in the free-flow hopper ($W = 21$ mm), material flow out and a loose region is formed near the outlet. Note the predicted high density shows the limitation of the numeral model, yet, it does not impair the results discussed in this chapter. In addition to the density, the near zero vertical velocity v_z predicted for the case of $W = 19$ mm in Figure 3.4(c) also indicates material arching.

Figure 3.4(d) demonstrates the comparison of the normalized friction ratio M/M_c ,

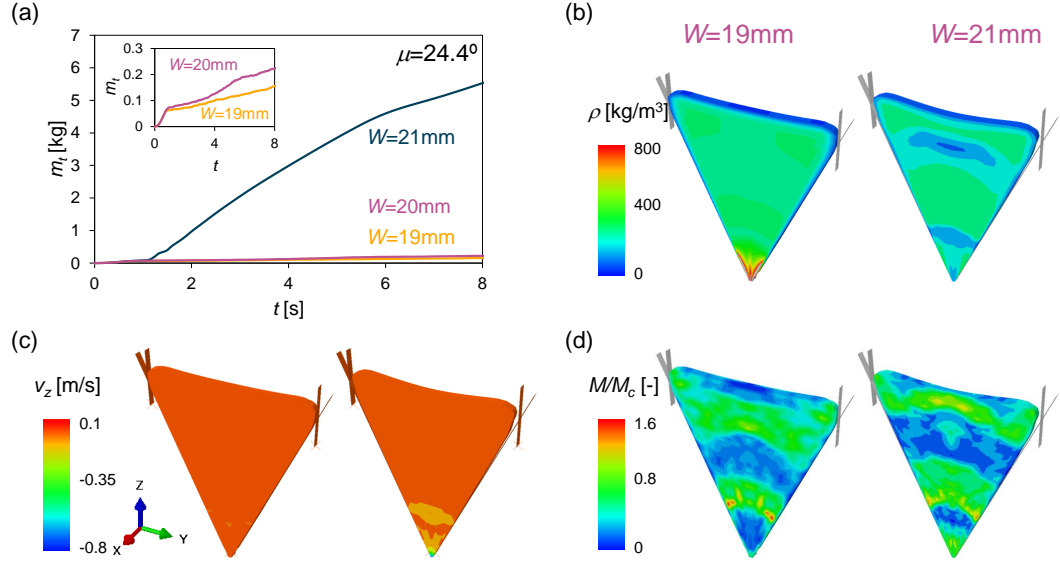


Figure 3.4: Numerical demonstration of hopper arching. (a) The predicted cumulative mass discharged m_t against time for a hopper with fixed inclination $\mu = 24.4^\circ$ and three outlet width $W = 19, 20, 21$ mm. Free flowing is predicted for $W = 21$ mm while hopper arching is realized for $W = 19, 20$ mm. Note the continuum mechanics-based model cannot model the complete stop of material flow as shown in the small zoomed-in figure, yet, the over one magnitude of difference in predicted flow rate indicates material arching is realized. (b-d) Comparison of the contours of the density (b), the vertical velocity (c), and the normalized friction ratio (d) between the arching hopper case with $W = 19$ mm and the free-flow hopper case with $W = 21$ mm.

where M is defined as the ratio of the deviatoric stress q over the mean stress p , and M_c is the slope of the critical state line in the $q-p$ space. Note M_c is dependent on the Lode angle and the void ratio. This friction ratio M/M_c physically represents whether shear stress is large enough to overcome the confining pressure and to initiate the flow. It is another good indicator of flow/no-flow state and can be interpreted for all critical state-based constitutive model as:

$$M/M_c \begin{cases} \geq 1 & \text{free-flow - material in the critical state,} \\ < 1 & \text{no-flow - material not yet reach the critical state.} \end{cases}$$

According to this theory, the M/M_c near the outlet is much smaller than 1 indicating hopper arching for the case of $W = 19$ mm. But for the case of $W = 21$ mm, the M/M_c near the

outlet is close to 1 implying material flow. Note that the small blue band in the $W = 21$ mm hopper case near the outlet is the result of a high void ratio (i.e., low density shown in Figure 3.4(b)).

3.4 Analyses and discussion

3.4.1 Hopper outlet width

The effect of the hopper outlet width W on the mass flow rate q_m is investigated both numerically and experimentally. Hopper flow tests with the variation of outlet width at the fixed inclination angle of 24.4° , 30° , and 36° were performed. Note that the same weight of pine chips were used for all experiments (~ 28 kg), which results in a slight change in material height within the hopper due to the inclination angle variation. The measured mass flow rates are presented as the yellow ‘ \times ’s in Figure 3.5. Following steps detailed in the subsection 3.2.3, the simulation predicted mass flow rates are obtained and shown as the fills diamonds. The numerical prediction can be fitted well with a linear relation shown as the dashed line. These lines closely overlay with the experimental data for all tested hopper inclination angles, demonstrating that increasing outlet width linearly increases the mass flow rate for hopper flow of pine chips. The intersections of the fitted lines with the outlet width W axis, which numerically represent the outlet width at a zero flow rate, overlap with the critical outlet widths W_{cr}^d (marked as filled triangles) obtained from the Dichotomy method (subsection 3.2.3). This mutual validation of the Dichotomy and the extrapolating methods demonstrate the robustness of the numerical model.

3.4.2 Hopper inclination

Hopper inclination angle is one of the most important design parameters, and its effects on the mass flow rate q_m and the critical outlet width W_{cr} were studied. Figure 3.6(a) presents the comparison of experimental measurements (markers) and numerical predictions (lines) of the $q_m - W$ relationship of the hopper at different inclination angles ($24.4^\circ - 36^\circ$).

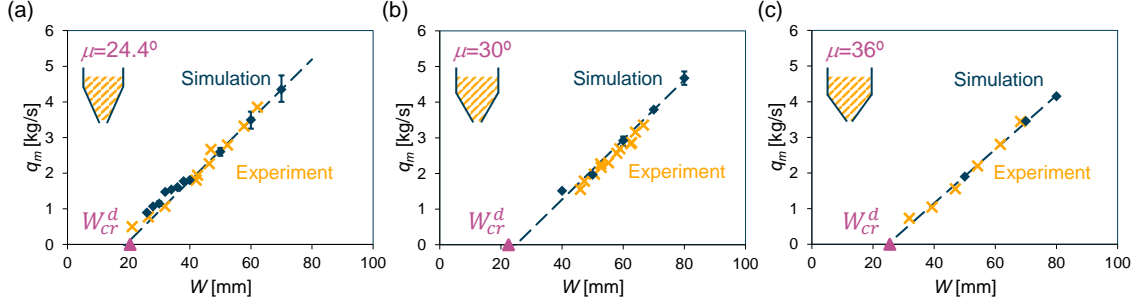


Figure 3.5: Effect of hopper outlet width W on the mass flow rate q_m with hopper inclination angle of (a) 24.4° , (b) 30° and (c) 36° . For each case, the yellow ‘ \times ’s stand for experimental measurements, the filled diamonds represent numerical predictions, and the dashed line is fitted from numerical results. The filled triangles located on the W -axes W_{cr}^d are the critical outlet widths obtained from the Dichotomy method for each hopper inclination case.

The numerical predictions have a good match against the experimental measurements, and both of them show the mass flow rate decreases with increasing inclination angle for all fixed outlet widths. This decreasing trend gradually slows down until it reaches a basin around $\mu = 30^\circ$. For cases with inclination angle exceeds this critical value (i.e., $\mu > 30^\circ$), experimental and numerical data overlap with each other at any given outlet width. The results imply the mass flow rate can be controlled slightly using the inclination angle at a value smaller than the critical one.

Figure 3.6(b) presents the variation of the critical outlet width W_{cr} against the hopper inclination angle μ , where yellow triangles are calculated from the classic Jenike design guideline, green ‘ \times ’s are experimentally measured results using the Dichotomy method described in the subsection 3.2.2, brown ‘+’s are obtained as the intersections between the fitting lines of the experiments measured $q_m - W$ data and the W axis as described in the subsection 3.4.1, and the dark circles stand for numerically obtained W_{cr} from both the Dichotomy method and the extrapolating method. Note that the numerical predictions of W_{cr} from the two methods are almost identical, which gives negligible error bars for each case. With these data points, it can be concluded that the numerical and experimental results generally agree with each other. The small difference is due to the local effect of

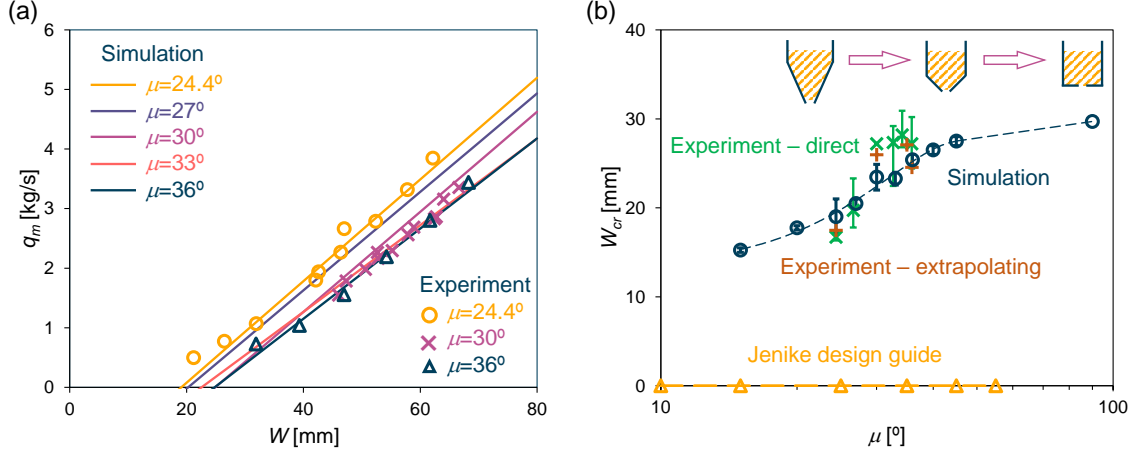


Figure 3.6: Effect of the hopper inclination angle μ on the mass flow rate q_m and the critical outlet width W_{cr} . (a) The plot of the mass flow rate q_m against the hopper outlet width W at different inclination angle μ . Markers represent experimental measurements, and lines stand for simulation predicted results. Different hopper inclination angles μ are color-coded. (b) The influence of hopper inclination angle μ on the critical outlet width W_{cr} . The green 'x's with error bars are measurements from experiments. The brown '+'s are extrapolated as the intersections of the experiments measured $q_m - W$ fitting lines (Figure 3.6(a)) and the W -axis. The dark circles represent numerically obtained W_{cr} from the Dichotomy method and the extrapolating method, note the two methods obtained W_{cr} are close to each other. The yellow triangles are calculated from the classic Jenike design guide. The axis of inclination angle is in log-scale.

pine samples near the outlet area with a non-representative particle size distribution. This localization effect is often observed in biorefineries as a variation of critical outlet size is observed for the same feeding material. In contrast to the numerical and experimental results, the Jenike design approach [66, 26] predicts no arching for all the cases. This over-estimation of the material flowability clearly explains the inconsistent flow experienced by many biorefineries.

In general, both the numerical predictions and the experimental measurements show the critical outlet width W_{cr} increases with the increasing hopper inclination angle. When μ is small, the flow is initiated first as the gravity ($F_g = \sqrt{F_s^2 + F_n^2}$) induced driven force F_s along the wall exceeds the wall friction resistance $F_n \tan \phi_w$, recall a low wall friction angle $\phi_w = 8.5^\circ$ is used for experiments and simulations. When the inclination angle μ increases, gravity results in more normal force ($F_n = \sin \mu F_g$) and less driven force ($F_s = \cos \mu F_g$),

so that an increasing outlet width is needed to flow the material. When μ becomes large enough, overcoming the friction resistance within the material is more easier comparing to overcoming the wall friction resistance. Material shear along a plane with an inclination angle μ' smaller than μ , and funnel flow pattern occurs.

3.4.3 Initial packing

Time effect (i.e., material self-weight compaction) is another important reason for biomass handling issues in biorefineries. For conventional granular materials, their particles are almost non-compressible, and self-weight compaction is negligible in the time period of material storage and handling. Yet, the high compressibility of biomass particles results in compaction under self-weight. In this section, the time effect is investigated by simulating hopper discharge with a fixed mass of materials (30 kg) at different initial packing conditions. This varying initial compaction is realized by assign different values of the initial density/void ratio. As demonstrated in Figure 3.7(b), a high void ratio or a low density corresponds to a loose packing, and a low void ratio or a high density stands for dense packing.

Figure 3.7 demonstrates the influence of initial packing on the flow behavior and the critical outlet width W_{cr} . Figure 3.7(a) and (c) show the variation of the cumulative discharged mass m_t against time in a slender hopper with $\mu = 30^\circ$ and a flat-bottom hopper with $\mu = 90^\circ$, respectively. In both plots, the cases with loose packing initially (e.g., $\rho_i = 220 - 240 \text{ kg/m}^3$) result in straight and smooth flow responses. For the cases with dense packing initially (e.g., $\rho_i = 300 \text{ kg/m}^3$ in Figure 3.7(a) and 270 kg/m^3 in Figure 3.7(c)), the slope of $m_t - t$ response varies from time to time, implying a surging or chunk-by-chunk flow behavior is predicted. Surging flow not only results in inconsistent material feeding, but also creates dynamic loading on the handling equipment. The influence of initial packing on the critical outlet width W_{cr} is shown in Figure 3.7(b) and (d). For the slender hopper, W_{cr} is not sensitive to the initial packing condition. However, the

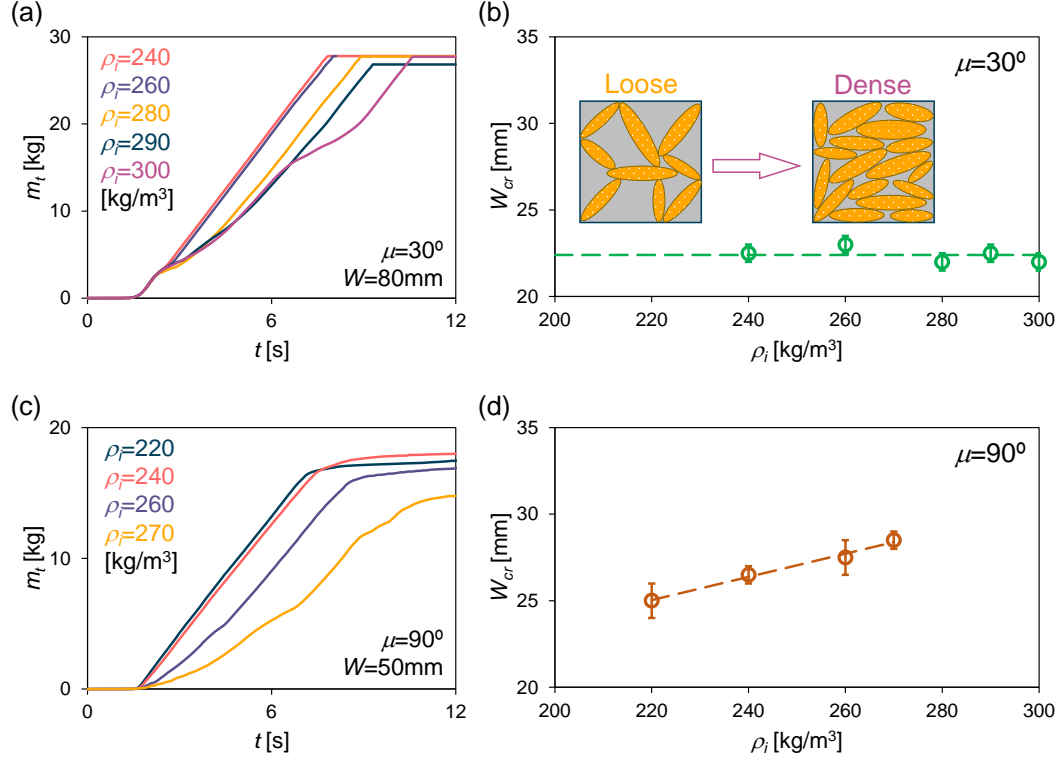


Figure 3.7: Effect of the initial packing on the mass flow rate q_m and the critical outlet width W_{cr} . (a, c) Predicted cumulative discharged mass m_t versus time t for a slender hopper with $\mu = 30^\circ$ and a flat-bottom hopper with $\mu = 90^\circ$, respectively. (b, d) Predicted critical outlet width W_{cr} at different initial packing conditions ρ_i in the slender hopper and in the flat-bottom hopper.

increase of W_{cr} with increasing initial density ρ_i indicates flow initiation gets harder for a densely packed material in the flat-bottom hopper.

The physical mechanism of these predicted flow behavior is the dilation (respectively, compaction) requirement of densely (respectively, loosely) packed material for flow. According to the critical state theory, material flow only occurs when both the stress and void ratio reach their corresponding critical state value. Given all materials within the hopper are assigned with the same packing density, the dilation of densely packed material away from the outlet requires extra space. This requirement can only be satisfied when the material below flows out and makes the way for volume expansion. This process occurs chunk-by-chunk manifested as surging flow (Figure 3.7(a, c)). For loosely packed material, it is compacted throughout the whole hopper while flowing, which results in smooth

flow behavior. For critical outlet width W_{cr} , the balance between the driven force and the resistance near the outlet determines its value. For the slender hopper, the wall friction angle determines the two forces as explained in the subsection 3.4.2, and the value of W_{cr} is not sensitive with packing (Figure 3.7(b)). However, for the flat-bottom hopper, the internal friction angle at the critical state determines the balance of the two forces. A densely packed material requires a higher driving force than a loosely packed material to reach the balance, which results in a higher magnitude of the critical outlet width (Figure 3.7(d)).

3.4.4 Particle density variability

One distinctive feature of granular biomass materials in comparison with conventional granular materials is their multi-scale variability [80, 81]. For ground loblolly pine, the most important variability is the particle density ρ_p given the critical state theory uses void ratio as a state variable that needs to be calculated via particle density. Direct measurement of ρ_p is challenging because of the existence of inner pores within particles and the difficulty to distinguish the inner pores from the exterior pores (void space among particles) [29]. Usually, the particle density is estimated from the density of the original wood block. However, the density of wood can be different among tree plantation location [50], tree age and height [49], and position of the wood on each tree. Therefore, the influences of particle density variability on the hopper flow performance is investigated.

The variation of particle density is not straightforward for the G-B hypoplastic model, instead, it is embedded within all the constitutive parameters. After selecting a reasonable range of the particle density for pine chips around 430 kg/m^3 , which is the value used so far, the model parameters were calibrated according to the same workflow reported in the previous work [65] against the same set of experimental data. The calibrated constitutive parameters with different ρ_p are listed in Table 3.1. With these parameters, hopper flow simulations were performed to obtain the flow response and the critical outlet width W_{cr} . Results are summarized in Figure 3.8. Note that the range of particle density is selected

Table 3.1: G-B-hypoplastic model parameters for the pine samples with different particle density.

ρ_p [kg/m ³]	ϕ_c [°]	h_s [kPa]	n [-]	e_{d0} [-]	e_{c0} [-]	e_{i0} [-]	α [-]	β [-]
350	47.3	55.0	0.327	0.17	0.68	0.88	0.32	1.7
400	47.3	129.0	0.304	0.38	0.92	1.19	0.30	1.2
430	47.3	187.6	0.300	0.50	1.06	1.38	0.3	1.0
500	47.3	354.9	0.285	0.77	1.40	1.82	0.27	0.8
550	47.3	494.0	0.280	0.96	1.64	2.13	0.26	0.6

based on previous studies [29, 49, 50]. Table 3.1 shows the most sensitive parameters to the particle density variability ρ_p is the granulate hardness h_s , it increases almost one-magnitude for a change of ρ_p from 350 to 550 kg/m³. Other parameters are either not dependent on ρ_p (ϕ_c), or not sensitive (α, β, n). Note that the void ratios (e_{d0}, e_{c0}, e_{i0}) serve as the bounding limits of the constitutive model and monotonously increase with increasing ρ_p .

Figure 3.8(a) and (c) present the numerically obtained mass flow rate q_m variation with hopper outlet width W in a slender hopper of $\mu = 30^\circ$ and a flat-bottom hopper of $\mu = 90^\circ$, respectively. It can be seen that particle density does not have a significant influence on the mass flow rate. Note only the two cases with the minimum and maximum particle densities are shown given all other cases have similar results.

Different from the mass flow rate, the predicted critical outlet width W_{cr} for the flat-bottom hopper ($\mu = 90^\circ$) changes significantly with particle density (Figure 3.8(d)). This dependence is not observed for the slender hopper ($\mu = 30^\circ$, Figure 3.8(b)). As sketched in Figure 3.8(b), a low particle density stands for soft particles, while a high ρ_p represents hard particles. Under the same loading condition, the material with a high granulate stiffness undergoes smaller deformation and interlocks more easily comparing to the material with a low granulate stiffness. This poor flowability with interlocking happens within the material. For the slender hopper, the critical balance of driven force and resistance is located at the wall as explained before, W_{cr} is independent of the interlocking induced by hard granulate

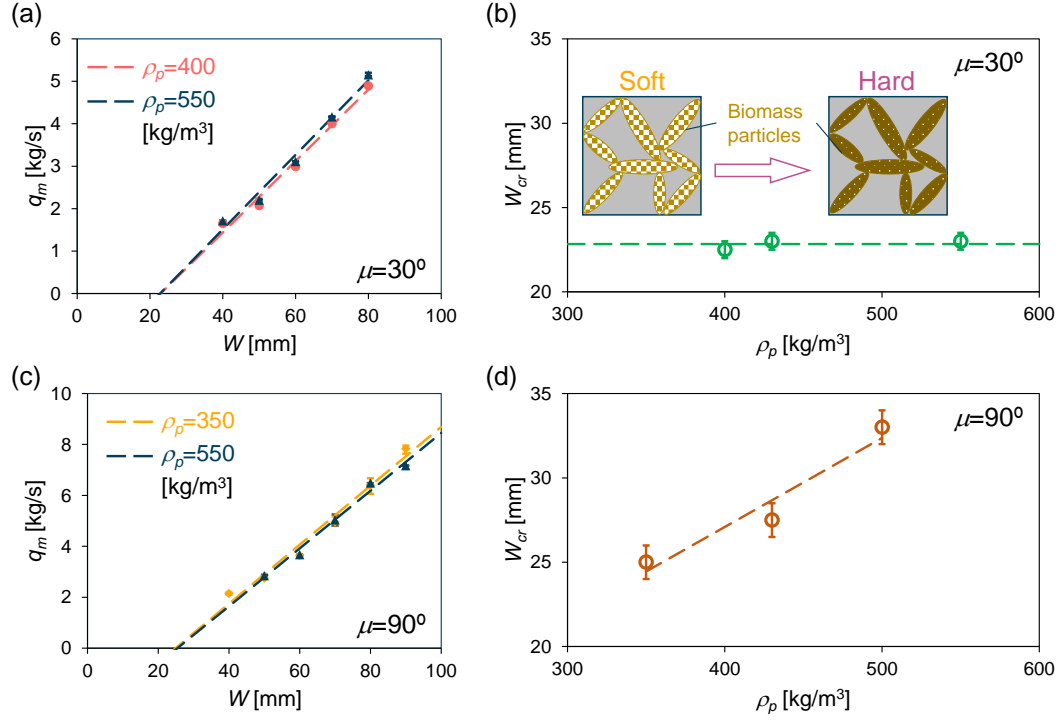


Figure 3.8: Effect of particle density variability on flow performance. (a, c) Predicted mass flow rate q_m of pine chips with different particle density against hopper outlet width W for a slender hopper ($\mu = 30^\circ$) and a flat-bottom hopper ($\mu = 90^\circ$). (b, d) The critical outlet width W_{cr} predicted at different particle density ρ_p for hoppers with inclination angle of 30° and 90° .

stiffness. However, for the flat-bottom hopper, internal friction and interlocking within the material determine the balance of the driven force and resistance. Consequently, the material with a higher granulate stiffness requires more driving force to counterbalance the interlocking, and a higher critical outlet width has resulted.

3.4.5 Surcharge

The surcharge, such as applying dead weight on the top of the feedstock in the hopper or filling more material, is a practice adopted to facilitate hopper discharge. The underline mechanism of surcharge is to add additional vertical stress as the driving force for hopper flow, however, the success of this practice varies case by case. Limited investigations have been done in literature on the influence of surcharge on the flow performance and the critical outlet width. In this section, the surcharge effect is studied through filling height variation

by numerically simulating the discharge process of the hopper filled with different amounts of material. Similar to the previous sections, two sets of simulations were performed with a slender hopper ($\mu = 24.4^\circ$) and a flat-bottom hopper ($\mu = 90^\circ$).

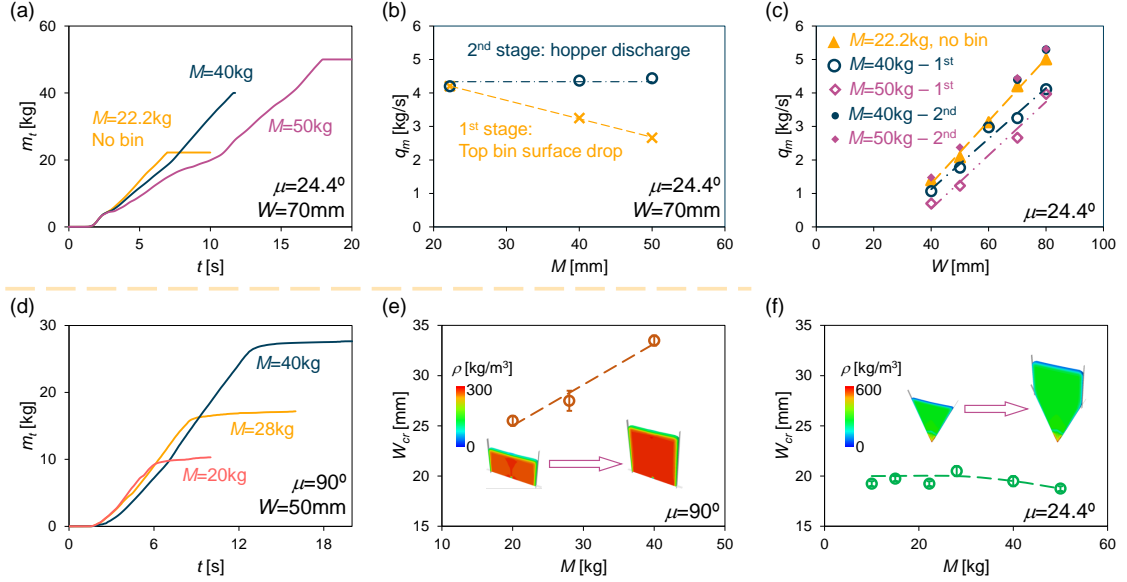


Figure 3.9: Effect of filling height on the flow response. (a, d) Predicted cumulative discharged mass m_t against time with different initial amount of materials for a slender hopper ($\mu = 24.4^\circ$ and $W = 70$ mm) and a flat-bottom hopper ($\mu = 90^\circ$ and $W = 50$ mm). Two stages of the flow rate (i.e., the slope of the $m_t - t$ response) are observed for the slender hopper (a). Note the case with material mass $M = 22.2$ kg does not have enough material inside the upper bin, only a straight line is predicted for $m_t - t$. (b) The mass flow rate q_m variation with the initial amount of material M obtained from the two stages. (c) Mass flow rate q_m variation against hopper outlet width W for different initial amounts of material and different stages. (e, f) The critical outlet width W_{cr} predicted for the flat-bottom hopper and the slender hopper against the initial filled material mass M .

Figure 3.9(a) presents the cumulative discharged mass m_t with time for different initial amount of material in a slender hopper ($\mu = 24.4^\circ$ and $W = 70$ mm). Note the case with $M = 22.2$ kg corresponds to a hopper without an upper bin, its $m_t - t$ is a straight line. For the other two cases, the $m_t - t$ responses are dual-linear. By observing the flow process, it can be found that the dual-linear response has resulted from the two-stage flow behavior. In the first stage, the material is discharged under the vertical pressure of the upper-bin material, and this stage ends when the top surface of the material touches the hopper-bin intersection. In the second stage, the rest of the material inside the hopper flows out

without any surcharge. The two-stage flow process is verified by the equivalent mass flow rate of the 2nd stage for all cases shown in Figure 3.9(b). Contrary to the assumption that surcharge can facilitate hopper flow, mass flow rate decrease with increasing filling height (reflected as the total amount of mass M) for the 1st stage (Figure 3.9(b)). This finding was further examined by modeling hopper flow with different outlet widths. Figure 3.9(c) plots the predicted q_m against hopper outlet width W for different initial filling mass M . It is clear that the mass flow rate of the 2nd stage overlap with each other and the mass flow rate decreases with increasing initial filling material mass for all cases. This phenomenon is also observed for the flat-bottom hopper as shown in Figure 3.9(d). The critical outlet width W_{cr} affected by the total amount of material is shown in Figure 3.9(e-f). In the flat-bottom hopper, the initiation of flow becomes harder with a heavier surcharge (Figure 3.9(e)). However, for the slender hopper (Figure 3.9(f)), the W_{cr} keeps constant when M is small, and it starts to decrease when M exceeds 22.2 kg.

The above phenomena of flow performance result from two competing mechanisms as the surcharge increases: 1) the extra weight of material compacts the material inside the hopper and decreases material flowability; 2) the extra weight of material increases the discharge driven force and facilitates the flow. The compaction mechanism is clearly demonstrated in Figure 3.9(a-d), the mass flow rate decreases with increasing surcharge weight for both the slender hopper and the flat-bottom hopper. The facilitation mechanism is reflected in the critical outlet width for the slender hopper case. Significant portion of surcharge weight is added to the flow driving force $F_s = \cos \mu F_g$ with small μ , and the critical outlet width W_{cr} decrease with increasing M when $M > 22.2$ kg as shown in Figure 3.9(f). For $M < 22.2$ kg, the material's height does not reach the hopper-bin intersection, the added weight is balanced by the wall friction resistance, which results in constant critical outlet width. Note the compaction mechanism has insignificant influence on critical outlet width in slender hoppers as detailed in the subsection 3.4.3. For the flat-bottom hopper, the material stagnation zone creates a shear surface with a high inclination

angle, less portion of the surcharge weight is used to drive material flow. In addition, the high internal friction angle increases the resistance. The combination of a less driving force and more resistance results in a trivial effect for flow facilitation of the surcharge weight. The compaction mechanism dominates this case, wider outlet opening is needed for more initial filling material.

It is concluded that the surcharge has significant influences on the hopper flow performance, which is contradictory to the literature [35, 34]. It is believed that: 1) the material (pine chips) used in this study has much higher compressibility than the conventional granular materials (e.g., sand) [65], compaction is more significant; 2) the constitutive model, used in previous studies (e.g., Mohr-Coulomb model), is not capable of capturing density-dependent flow behavior, while the G-B hypoplastic model used in this study can. These discrepancies demonstrate the significance of using a density/void ratio dependent model to characterize the flow behavior of compressible biomass materials.

3.5 Conclusions

Biomass material is a promising and sustainable energy resource but is limited in use because of significant difficulties and financial losses on material handling. In this work, a representative biomass material, loblolly pine chips, was used and its flow performance in a wedge-shaped hopper was investigated. A wedge-shaped hopper was firstly designed at the pilot-scale with adjustable wall inclination angle and outlet width. Then, the hopper flow rate response and the critical hopper outlet width were experimentally studied at various combinations of hopper inclination and outlet opening width. After a three-dimensional FEM model was developed and validated against the experimental data, the hopper flow performance affected by the outlet width, hopper inclination, initial packing, biomass particle density, and the filling height were numerically studied. Main contributions and conclusions are summarized as follows:

1. The numerical model consisting of the G-B constitutive law and the CEL solver is a

reliable tool to study hopper flow performance. A combination of physical experiments and comprehensive simulations is a cost-effective and time-efficient approach to address bulk material flow challenges at all scales.

2. The mass flow rate of pine chips increases with the hopper outlet width linearly, and it decreases with the wall inclination angle slightly. The decreasing trend stops when the inclination angle reaches the critical value of around 30° . The initiation of the flow is easier for a slender hopper as the critical outlet width increases with increasing inclination angle.
3. The flow pattern of the compressible particles is closely related to the initial packing of the material. A dense packing results in surging flow while a loose packing has a continuous smooth flow. More dense packing results in a wider critical outlet width for silo (flat-bottom hopper), not for slender hoppers.
4. The variability of biomass particle density creates uncertainty for the calibration of material constitutive parameters. Its influence on hopper flow performance is trivial except the critical outlet width for the silo: higher particle density results in a higher critical outlet width.
5. Surcharge affects the flow performance with two competing mechanisms: 1) flow impedance by the compaction of material and 2) flow facilitation by the increase of discharge driven force. The mass flow rate is dominated by the compaction mechanism so that the mass flow rate decreases with increasing surcharge weight. For the critical outlet width, the compaction mechanism also dominates in silos, higher surcharge weight results in wider critical outlet width. Yet, the facilitation mechanism dominates in slender hoppers.

CHAPTER 4

WEDGE-SHAPED HOPPER DESIGN FOR MILLED WOODY BIOMASS FLOW

4.1 Introduction

Addressing the bioenergy material handling challenges, e.g., particle segregation, surging flow, and jamming in hoppers, feeders, and conveyors, demands in-depth understandings of milled biomass material flowability, efficient flow prediction tools, and renovations of equipment design [11]. Efforts have been made to probe the complex flow behavior of various biomass materials [82, 83, 84, 13, 63, 85, 86, 9, 87] and to explore their flow and jamming physics in handling equipment [7, 24, 88, 89]. However, equipment design and operation taking woody biomass flow behaviors (e.g., flow pattern, flow rate) into consideration are still needed. For example, hoppers are one of the most widely used material handling equipment and their design still relies on the early work of Jenike and colleagues in 1960s [66, 26, 67]. Use of hoppers with outdated design in biorefineries often results in arching and jamming [17, 7], indicating the need for a modified design guide that incorporates state-of-the-art knowledge on biomass flow behavior. The updated design is expected to provide trouble-free hopper flow with the favored flow pattern and precise prediction of flow throughput.

There are two typical patterns in hopper flow: 1) mass flow, where all material moves and the material at the same height tends to flow with a similar speed (first-in/first-out), and 2) funnel flow, where a channel of moving material forms over the outlet with the rest forming a stagnant zone near the hopper walls (first-in/last-out). Mass flow ensures a more uniform discharge of material, whereas funnel flow may cause particle segregation [90] and make a hopper more susceptible to surging flow (material discharges chunk by chunk). At large scales, this may result in erratically high impact load on the hopper wall and subse-

quently cause hopper damage. Furthermore, the stagnant zone formed in funnel flow often results in material not able to be fully discharged. In order to avoid funnel flow, physical inserts can be placed inside hopper to modify the flow pattern [91, 92, 93, 94]. In addition, Jenike and colleagues [66, 26] developed a set of design charts in terms of hopper wall inclination, wall friction, and material internal friction to distinguish the two flow patterns. These design charts were developed using the Mohr-Coulomb (MC) model for describing material behavior and were widely used for various conventional granular materials. However, the MC model is incapable of describing the complicated flow behavior of biomass materials, because milled biomass features high particle flexibility, high bulk compressibility, and density-dependent mechanical behavior as compared to conventional granular materials [12, 32, 65]. Although the original Jenike design charts have been improved over the time for applications of non-conventional granular materials [95, 96, 97, 98, 99, 69, 100], milled biomass has not been well investigated yet for hopper. A simplistic and robust design chart for hopper will be essential for the bioenergy industry.

Hopper arching, a long-lasting challenge in bulk material handling, has been extensively investigated with both physical experiments and numerical simulations. For example, the hopper critical outlet width for flowing of conventional granular materials ranging from the ideal spherical beads to engineering materials (e.g., pharmaceutical particles, rocks, coals, and ores) have been investigated [34, 70, 73, 71, 72, 75]. Unfortunately, the arching behavior of granular biomass materials are way different from conventional materials [88] due to its distinctive characteristics (i.e., low particle density, high aspect ratio, high compressibility, and high shear resistance) [65]. As a result, the widely used Jenike hopper design guide [66, 26] usually overestimates the critical outlet width of hopper for conventional granular materials [68, 69, 34], but it constantly underestimates the critical arching outlet width for milled biomass materials [17, 7, 88].

Besides flow pattern and arching, the correct prediction and precise control of the hopper flow throughput (i.e., mass flow rate) are also important to ensure a trouble-free material

handling workflow. Series of equations have been established to predict the flow rate [101, 102, 103, 35]. Beverloo [101] pioneered an equation, which has been widely used with great successes on flat-bottom hoppers (aka, silo). To extend the application of Beverloo equation, Rose and Tanaka [104] and Brown and Richards [105] developed different equations to account for inclined-wall hoppers. In addition, the hourglass theories [106, 107, 108, 102] have been established to consider the roles of wall friction and material properties for predicting hopper mass flow rate. The most recent equation for mass flow rate prediction was proposed by the British Material Handling Board [102, 103] for both conical-shaped and wedge-shaped hoppers. Unfortunately, none of the above equations can offer a reliable prediction of the flow throughput for biomass materials.

To bridge the knowledge gap mentioned above and provide an updated design guide for bioenergy industry, this chapter attempts to investigate the critical flow behavior of woody biomass materials in wedge-shaped hoppers through physical experiments and numerical simulations. Two types of milled biomass, loblolly pine and Douglas fir, were used to conduct flow experiments in a customized wedge-shaped hopper. A finite element model with a hypoplastic material model was developed and validated to simulate the flow. Comprehensive flow and arching simulations and experiments were performed to determine the boundary of two flow patterns, identify the critical outlet width for arching, and obtain the mass flow rate. Critical material attributes (CMAs) and critical processing parameters (CPPs) for hopper design were identified to guide the trouble-free hopper design, and an empirical equation was established to predict the flow throughput. This chapter provides a novel design guide for flowing woody biomass in wedge-shaped hoppers.

4.2 Methods

4.2.1 Woody granular biomass materials

Woody biomass materials are commonly proposed to be used as feedstock for thermochemical conversion to generate energy and fuels from biorefineries [9, 109, 110]. The

pine samples used in this work was prepared by milling the stem of loblolly pine. Pine trees from the southern Georgian area were harvested, debarked, chipped, and hammer-milled until the particles pass a 6 mm retention screen in the mill. Then the pine chips were dried in a rotary drum until the moisture content reaches around 6%, this sample is denoted *as-ground*. To evaluate the influence of fine particles on the flow behavior, we sieved out and discarded the fines using a 0.85 mm screen (Round Separator, SWECO), and the remaining material is called *engineered*. More detailed information about the sample preparation was reported in a previous study [12]. Note that the two as-ground pine samples originated from the same parent loblolly pine chips. Several samples were taken over the course of the on-spec material production, and the natural variability in milling and material [111, 112, 80] resulted in the differences observed in pine-1 and pine-2. The particle size distribution measured from sieve analysis and photos showing their size and shape are presented in Figure 4.1.

Douglas fir trees were sourced and processed around Auburn, WA. After debarking the tree boles were chipped and then size reduced using a rotational, shear-based size reduction technique (Forest Concepts, Auburn, WA). The size reduced particles are then fed to an orbital screen where particle fines are removed, the on-spec sized particle are collected, and particles that are too large are recycled. For the 4mm particles, 9.5mm and 2.4mm screens were used to collect the on-spec particles. Similarly, the 2 and 1mm particles used screens of 4mm and 0.8mm, and 1.7mm and 0.4mm respectively. The nominal size labeling for these samples roughly corresponds to the 50% passing size as measured by analytical sieve.

4.2.2 Experimental setup

¹ As shown in Figure 4.2(a), a customized wedge-shaped hopper was used in this study with adjustable hopper walls by sliding and rotating. The width of the hopper at the top

¹The experimental work in this chapter were conducted by the Idaho National Laboratory.

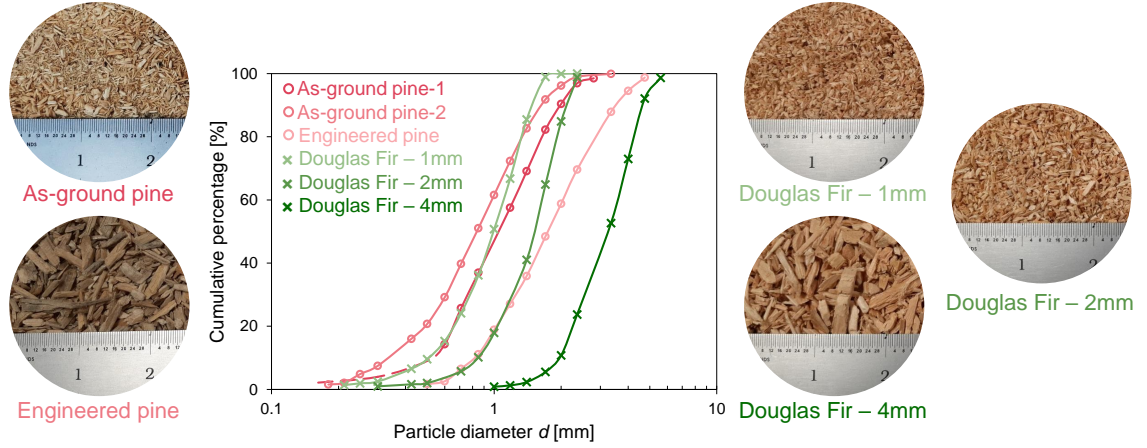


Figure 4.1: Particle size distribution of the 6 woody biomass samples used in this study with photos showing their size and shape. Note the unit of the ruler is an inch. The left two photos are as-ground and engineered loblolly pine samples, and the right three photos are Douglas fir samples generated from a crumbler with a head of 1, 2, and 4 mm, respectively. Note that the as-ground pine-1 and pine-2 samples originated from the same parent loblolly pine chips, and the difference of particle size distribution results from the biomass material variability.

is fixed as 0.6 m. Two vertical steel plates were fixed inside the hopper to constrain the axial dimension of 0.4 m. A cuboid bin can be equipped above the hopper to charge more material. The half angle of hopper inclination is denoted as μ and the outlet width is denoted as W (Figure 4.2(b)). More detailed description can be referred to subsection 3.2.2.

This hopper setup is capable of measuring discharge throughput q_m and critical outlet width W_{cr} for arching with various hopper inclination angles and outlet widths. The methods to measure q_m and W_{cr} are presented in subsection 3.2.2. Typical $m_t - t$ discharge responses measured from experiments can be found in Figure 4.2(c) as the green markers and a typical arching reflected through no-flow/flow discharge response can be found in Figure 4.5(a) and in the earlier work [88].

4.2.3 Numerical modeling and validation

Both the Discrete Element Method (DEM) and Finite Element Method (FEM) are effective numerical tools to simulate the flow behavior of milled woody biomass [89, 28, 32, 113]. DEM is preferred to investigate the particle-particle interaction and is capable of modeling

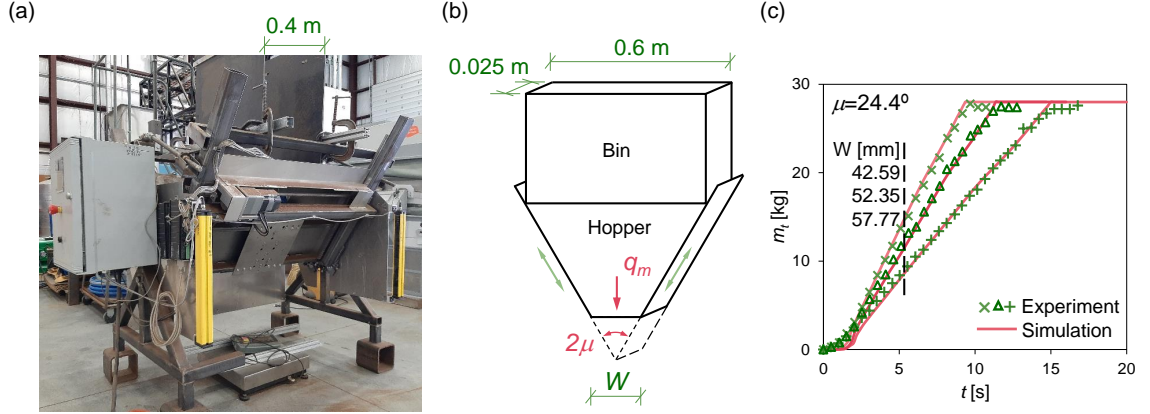


Figure 4.2: (a) Experimental setup for the hopper test. A wedge-shaped hopper is equipped with adjustable hopper inclination angle via rotating hand-wheels and outlet width controlled with step motors. The vertical steel plates inside the hopper are to control the length along the axial direction. A cuboid bin can be equipped above the hopper. A scale is placed below the hopper to measure the time-lapse discharged weight. (b) Numerical setup simulating a slice of the hopper-bin system based on the plane strain condition. (c) Validation of the numerical modeling by comparing the numerical prediction of discharge responses (lines) against the experimental measurements (dots) at different hopper outlet width W .

discontinuous flow systems [114, 76, 115], while FEM performs better on the parameterization of materials and can efficiently decipher the flow physics at large-scale systems [12, 65, 88]. This chapter used FEM to simulate the flow and arching behavior of woody biomass in wedge-shaped hoppers at equipment scale. To circumvent the mesh entangling difficulties involved in the hopper FEM flow modeling with large-deformation, the coupled Eulerian-Lagrangian (CEL) scheme was utilized.

Several state-of-the-art constitutive models that have been used to simulate the flow behavior of milled biomass are reviewed by Jin et. al [32], including hyperplastic models (Mohr-Coulomb, Modified Drucker-Prager/Cap, Cambridge-type Models), hypoplastic models (Gudehus-Bauer(G-B)), and rheology models ($\mu(I)$, Nonlocal Granular Fluidity). Among them, the Cambridge-type Models and the G-B model have incorporated the critical state theory, which defines the state of void ratio and stress that material can shear infinitely. The explicit stress integration of the G-B model makes it computationally robust for simulating large deformations and it has been successfully adopted for simulating

biomass granular flow. The formulation, implementation, parameter calibration, and model validation have been reported in the recent study [65], along with the open-source release of Abaqus User Material Subroutine (VUMAT) on Github. The calibrated G-B material parameters for the *As-ground pine-1* sample are listed in Table 2.3 (as the as-ground sample).

A schematic view of the numerical model is shown in Figure 4.2(b), which has the same geometry as the experiment except for the thickness in the axial direction. The wall friction angle ϕ_w was experimentally determined using a reciprocating sliding tribometer [76], where the biomass sample was slid along a flat surface of the wall material (carbon steel in this study) and the normal and tangential forces were measured during the sliding. The ϕ_w was determined and fixed as 8.5° accordingly for most of the simulations and varied when investigating the influence of the wall friction. More information about numerical modeling and how to obtain q_m and W_{cr} can be found in subsection 3.2.3.

The numerical model was validated by comparing the numerical discharge responses $m_t - t$ against the experimental measurements. As demonstrated in Figure 4.2(c), the experimental and numerical $m_t - t$ responses overlap with each other for all three outlet widths, indicating that the numerical model can quantitatively simulate the flow behavior. Note that the agreement of the critical arching distance W_{cr} between experiments and simulations was reported in the previous work [88].

4.3 Results & Discussion

4.3.1 Flow patterns

A demonstration of mass flow and funnel flow is shown in Figure 4.3(a), where the color contour represents the magnitude of the velocity. As described in section 4.1, mass flow (first-in/first-out) is more likely to guarantee a uniform material discharge. However, funnel flow (first-in/last-out) is more susceptible to handling issues. For example, the material may form a flow channel at the center above the outlet and the material near the hopper

wall consolidate into a cake, which forms the well-known rat hole problem in material handling. In addition, a funnel-flow hopper is more likely to have surging flow, where the material flows chunk by chunk, and this results in high impact loads on the hopper wall and may trigger hopper failure [26]. Moreover, funnel flow often causes particle segregation with inconsistent particle size distribution before and after the discharge [26, 116, 117, 118]. Therefore, this study aims to develop a numerical simulation-guided design chart, with which handling equipment designers can refer to for designing mass flow-guaranteed hoppers for woody biomass materials. This will greatly complement to the existing design approaches, in which the flow pattern is difficult to investigate through physical experiments quantitatively.

Mass flow index

The two distinct flow patterns can be quantitatively described by the Mass Flow Index (MFI) which is defined as

$$MFI = \frac{v_w}{v_c}, \quad (4.1)$$

where v_w and v_c stand for the average flow velocity at the hopper wall and at the hopper centerline, respectively. According to literature [118, 78], the velocity ratio of $MFI = 0.3$ can be utilized as a practical boundary, where $MFI > 0.3$ represents mass flow and $MFI < 0.3$ indicates funnel flow. Note that the MFI was only extracted from the hopper region without taking the bin into consideration. The v_w , v_c , and MFI are spatial-temporal variables, but a single MFI value from one simulation is needed to determine the flow pattern. Therefore, the spatial and temporal effects on MFI of each simulation need to be investigated to obtain a representative MFI.

The spatial variation along the axial direction was firstly investigated shown as the x -axis in Figure 4.3(a). 5 layers of elements were used to mesh the axial direction and the symmetric boundary condition was applied to the front and the back surfaces following the plane strain assumption. Theoretically, all the variables (e.g., stress, strain, density,

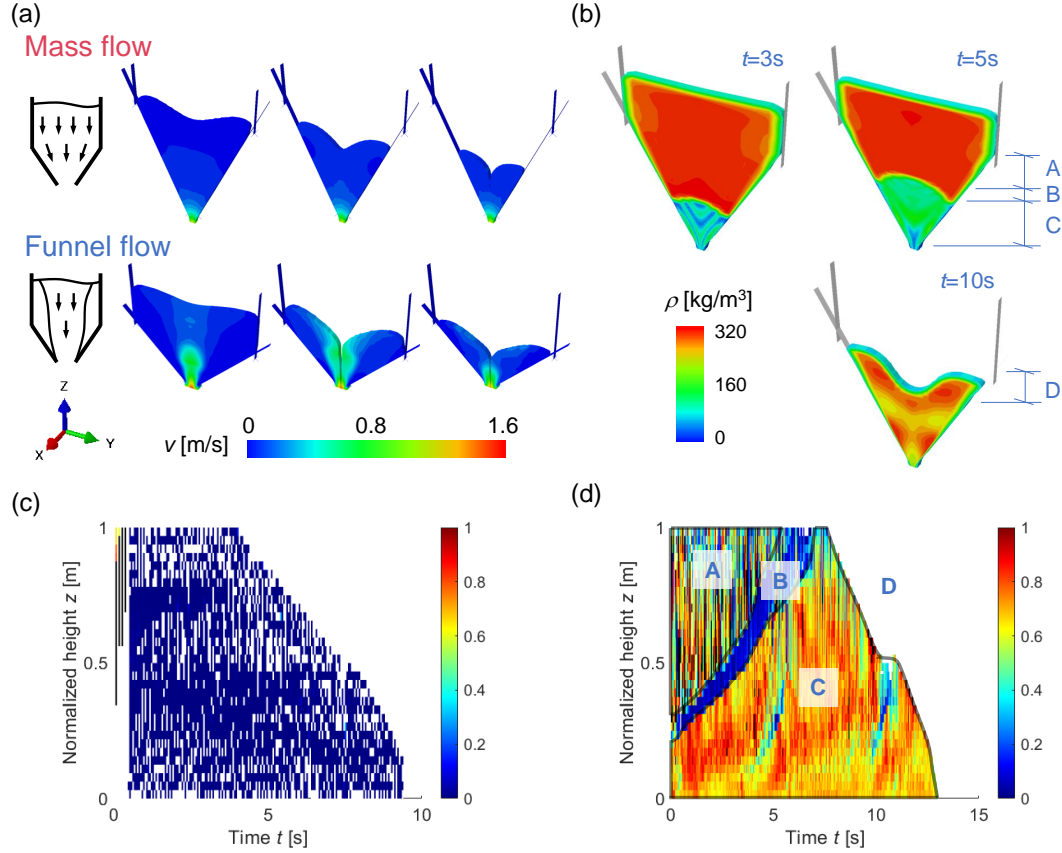


Figure 4.3: (a) Demonstration of the two flow patterns with the color representing velocity magnitude. Mass flow: $\mu = 24.4^\circ$, $\phi_w = 8.5^\circ$, $W = 52$ mm; Funnel flow: $\mu = 45^\circ$, $\phi_w = 30^\circ$, $W = 75$ mm. (b) The distribution of bulk density ρ_b at time $t = 3s$, $5s$, and $10s$ inside a simulated mass-flow hopper ($\mu = 30^\circ$, $\phi_w = 8.5^\circ$, $W = 60$ mm). Sections with different Mass Flow Index (MFI) are denoted as: A) no-flow zone, B) an arch-shaped layer between flow and no-flow zones, C) flow zone, and D) zone with material at the centerline already discharged. (c) The MFI map for a funnel flow simulation ($\mu = 30^\circ$, $\phi_w = 45^\circ$, $W = 60$ mm). (d) The MFI map for the mass flow simulation shown in (b) with the four MFI regions marked.

velocity, etc.) should be the same along x . It is confirmed that the simulation prediction is uniform along the x direction by comparing the v_x at the wall and at the centerline. As a result, the MFI were averaged at the x -axis.

The spatial-temporal variation of MFI along the z -axis (i.e., height direction) is more complicated, and the “MFI map” was developed by plotting the MFI against the normalized height z and the time t as shown in Figure 4.3(c, d). The MFI maps were color-coded from 0 (blue) to 1 (red) with black and white representing numerical anomalies: 1) when material

near the wall has not started flowing, the magnitude of v_w is trivial and fluctuates around zero, which may result in negative MFI, and these points were marked as white; 2) when material at the centerline has not started flowing (usually at the top part of the material), the denominator v_c is close to zero and may be smaller than v_w , which results in MFI greater than 1, and these points were marked as black. Note that MFI will also be plotted as white when material at the centerline has been completely discharged ($v_c = 0$, e.g., region D in Figure 4.3(d)) and MFI was extracted temporally since the flow was initiated. As shown in Figure 4.3(c), the MFI in the funnel flow situation ($\mu = 30^\circ$, $\phi_w = 45^\circ$, $W = 60$ mm) is close to zero in the spatiotemporal space except for the anomalies (black and white). However, for the mass flow case ($\mu = 30^\circ$, $\phi_w = 8.5^\circ$, $W = 60$ mm) shown in Figure 4.3(d), the MFI map has 4 regions A-D, corresponding to the spatiotemporal regions of the density distribution in Figure 4.3(b). Region A stands for the upper part of the hopper at the early flow stage where the material has not started flowing yet, and both v_w and v_c are close to zero with large MFI fluctuation. Region B represents the arch-shaped layer between the flow and non-flow zones, where v_w is close to zero while v_c is not, making MFI close to zero. The flow zone is denoted as regions C where both v_w and v_c are non-zero. Region D means the material at the centerline has been discharged while the material near the wall is still flowing, thus v_c , as well as MFI, is close to zero. It can be concluded that only the MFI from region C is meaningful and the average was taken in this region as a single representative MFI for each simulation.

The difference of using the total velocity v against velocity at the z direction v_z for computing MFI was also evaluated. It is found the value of v_z near the wall is smaller than its total counterpart v , and the resulted MFI is smaller than the value calculated from the total velocity, which challenges distinguishing mass flow from funnel flow. Accordingly, the total velocity was used to calculate MFI for all following cases.

It is worth noting that the proposed MFI is a simple and quantitative variable to understand flow pattern, and is sufficiently enough to guide industrial design. There are much

more complicated hopper flow patterns, for example, surging flow, flooding, expanded flow, sub-types of funnel flow [26, 118, 67, 119]. These patterns cannot be characterized by the single value of MFI, yet the MFI map can provide more information to get a better understanding of flow pattern.

Design charts

Hopper flow pattern is controlled by a series of material attributes and processing parameters. An exhausting investigation of all influencing parameters is not practical for physical experimentation and computationally non-affordable for numerical simulation. Only the critical processing parameters (CPPs) and the critical material attributes (CMAs), which have significant effects on the flow pattern, should be identified and investigated for the construction of design chart. Based on the previous studies on hopper flow [65, 88], it can be found that mass flow and funnel flow for a specific biomass material can be realized by adjusting the hopper inclination angle μ and the wall friction angle ϕ_w . This indicates μ and ϕ_w are the two CPPs for flow pattern.

For CMAs, the internal friction angle at critical state ϕ_c , which significantly influence the flow pattern for various granular materials according to literature [26, 118, 78], is a CMA for flow pattern of biomass hopper handling. In addition, a parametric modeling study indicates that the variation of initial relative packing can trigger surging flow and the granulate hardness h_s (Table 2.3) affects arching [88]. The relative packing is defined in terms of initial void ratio e and the minimum and the critical state void ratio e_{d0}, e_{c0} as $\xi = (e - e_{d0}) / (e_{c0} - e_{d0})$. Therefore, the effects of h_s and initial relative packing ξ , on flow patterns need to be quantified. The rest of material attributes listed in Table 2.3, including n (pressure sensitivity exponent), α (exponent governing shear strength for densely packed material), β (stiffness exponent), and e_{i0} (upper limit of void ratio), have negligible effects on hopper flow pattern based on their physical meaning and the preliminary simulations. Therefore, these parameters were excluded from the sensitivity analysis of CMAs. In sum-

mary, the potential CMAs for hopper flow pattern are internal friction angle ϕ_c , granulate hardness h_s , and initial relative packing (e_{d0} and e_{c0}).

To determine the CMAs from all potential candidates, a parametric study was conducted with varying ϕ_c ($30^\circ - 60^\circ$), h_s ($2 \times 10^1 - 10^4$ kPa), and ξ ($0 - 0.8$). All these cases were simulated with two fixed hopper configurations (i.e., case-1: $\mu = 30^\circ$, $\phi_w = 30^\circ$, $W = 60$ mm; case-2: $\mu = 20^\circ$, $\phi_w = 20^\circ$, $W = 50$ mm), which yield funnel flow and mass flow patterns for flowing *as-ground* pine samples, respectively. It was found that the granulate hardness h_s and relative packing ξ have negligible influence on MFI, and their effect is much smaller than the critical state friction angle ϕ_c . Therefore, it can be concluded that the internal friction angle at critical state ϕ_c is the only CMA for woody biomass to distinguish mass flow from funnel flow. Note that the initial packing ξ_{init} is a CMA to determine surging/non-surging flow [88], but the single MFI value cannot distinguish it from mass- and funnel-flow patterns.

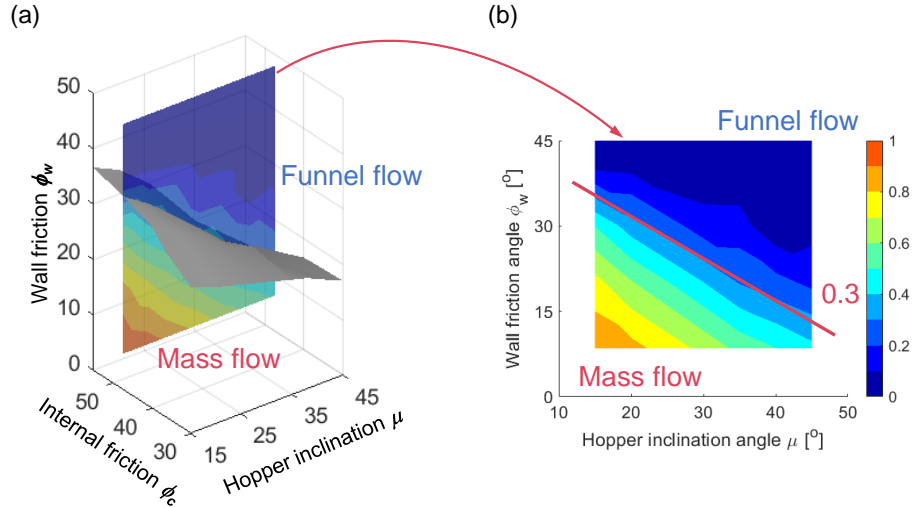


Figure 4.4: (a) Three-dimensional flow pattern design chart with the boundary (gray surface), which represents the MFI equal to 0.3, separating the two flow patterns. The color-coded slice represents the simulated MFI distribution for flowing the *as-ground* pine sample ($\phi_c = 47.3^\circ$) with different hopper configurations. (b) The two-dimensional MFI contour with a fixed internal friction angle of $\phi_c = 47.3^\circ$ representing the *as-ground* pine sample.

Series of simulations with the above identified CMA ϕ_c and CPPs μ and ϕ_w were conducted. The obtained flow pattern design charts are shown in Figure 4.4, where Fig-

ure 4.4(a) demonstrates the iso-surface of $MFI = 0.3$ (gray) serving as the boundary to separate the two flow patterns. Taking the *as-ground* pine sample with a fixed value of internal friction angle ($\phi_c = 47.3^\circ$) as an example of milled woody biomass, the MFI contour in the space of hopper configuration $\phi_w - \mu$ can clearly show the expected flow pattern with the boundary of $MFI = 0.3$, as shown in Figure 4.4(b). Note that the range of the internal friction angle ϕ_c $[30^\circ, 55^\circ]$ covers most of the woody biomass feedstock, and it has been identified from the parametric study that ϕ_c is the only CMA. Therefore, the design charts are applicable for most milled woody biomass including the 6 samples used in this study. The maximum of hopper wall friction ϕ_w is 45° because a friction coefficient greater than 1 ($\tan 45^\circ$) is physically meaningless and falls in the funnel flow pattern region according to Figure 4.4(b). Figure 4.4 shows that mass flow is qualitatively resulted with a slender hopper and smooth walls in general. For a specific woody biomass material with high internal friction, mass flow is easier to be obtained in slender hoppers, while a shallow hopper with a higher wall inclination angle μ can be utilized for the material with low internal friction. With the obtained MFI charts, equipment suppliers and hopper operators can optimize woody biomass handling by designing hopper geometry and the material construction of the hopper walls.

4.3.2 Arching

Avoiding arching is another important design criterion to achieve trouble-free hopper flow. The arching behavior affected by material properties and hopper processing parameters (e.g., inclination, initial packing, biomass density variability, and surcharge) have been studied and reported in the previous work with detailed discussion on force balance mechanism [88]. This chapter focuses on the wedge-shaped hopper design guide by quantifying the critical outlet width W_{cr} , which is defined as the hopper outlet size that marks the boundary between consistent flow and clogging.

Figure 4.5(a) shows the flow responses of hoppers with a wall inclination $\mu = 24.4^\circ$ and

outlet size $W = 19, 20, 21$, and 42 mm. Quantitatively, the responses of hopper cases with $W = 19$ and 20 mm are close to each other with $q_m \approx 0$. But the response of the hopper with $W = 21$ mm has a $q_m \gg 0$, indicating that arching occurs when $W = 19/20$ mm. The average of the arching and the flowing cases with the closest W was taken as the critical outlet width W_{cr} (i.e., $W_{cr} = 20.5$ mm with a ± 0.5 mm error range in this case). Qualitatively, hopper discharge can be seen when $W = 21$ and 42 mm, while the material is compacted at the bottom (with a large density) and does not flow when $W = 19$ mm, as shown in the density configuration at the upper left corner of Figure 4.5(a).

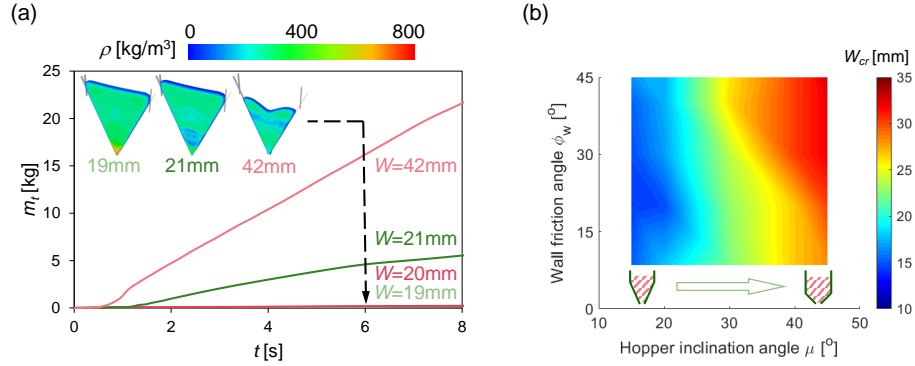


Figure 4.5: (a) Time-lapse responses of the cumulative discharged mass m_t with a hopper inclination of $\mu = 24^\circ$. The two hopper cases with $W = 19$ and 20 mm yield arching, while the two cases with $W = 21$ and 42 mm result in flowing. The color-coded profiles in the upper left of the plot present the density configuration at the time $t = 6$ s for all cases. (b) The predicted critical outlet width contour in the space of the hopper inclination angle μ and the wall friction angle ϕ_w .

Following the same approach in subsection 4.3.1, the CMAs and CPPs for constructing the W_{cr} design chart were firstly identified. The previous study [88] found that the initial packing has a negligible influence on W_{cr} for a wedge-shape hopper. Accordingly, the internal friction angle ϕ_c , granulate hardness h_s , hopper inclination angle μ , and wall friction angle ϕ_w were down-selected as the potential CMAs and CPPs for W_{cr} . Sensitivity analysis of all potential CMAs was conducted and the results show that the min-max range of W_{cr} caused by changing ϕ_c and h_s is about one magnitude lower than the range caused by varying μ and ϕ_w . Therefore, only the two CPPs (μ and ϕ_w) were chosen as the

design parameters.

Figure 4.5(b) demonstrates the critical outlet width W_{cr} changing with the hopper inclination angle μ and the wall friction angle ϕ_w . It can be observed that the influence of μ on W_{cr} is more significant than ϕ_w . This is because arching is fundamentally governed by the competence between the discharge driven force resulted from gravity ($F_g = \sqrt{F_s^2 + F_n^2}$) against the resistance force resulted from material internal friction and the material-wall friction [88]. When we have a slender hopper with a small μ , the gravity-driven force along the wall ($F_s = \cos \mu F_g$) is much larger than the wall friction ($F_f = \tan \phi_w F_n = \tan \phi_w \sin \mu F_g$) regardless of how large ϕ_w is. Therefore, material flows well with a hard time forming an arch if μ is small for a hopper with all possible wall friction angle ϕ_w . However, if we have a shallow hopper with a higher μ , the values of the driven force F_s and the pressure on the wall F_n are comparable. The increase of ϕ_w causes the escalation of wall friction ($F_f = \tan \phi_w \sin \mu F_g$), which makes the hopper more susceptible to arching. It is concluded that Figure 4.5(b) can serve as the critical arching design chart for handling woody biomass materials

4.3.3 Flow throughput prediction

In addition to predicting flow pattern and avoiding hopper arching, the last design metric is the prediction of hopper throughput (i.e., mass flow rate q_m). The 5 types woody biomass materials (6 samples) were comprehensively tested by hopper flow experiments with different inclination angle μ and outlet size W shown in Figure 4.1. The experimental results are shown in Figure 4.6(b) (pine samples) and Figure 4.7 (Douglas fir samples) as the red “×”s. To better understand the influence of the material internal friction ϕ_c (CMA) on hopper throughput, a series of numerical simulations of hopper flow were also performed with the as-ground pine-1 sample, shown as the red “○”s in Figure 4.6(b). As expected, the experimental and numerical flow rates agree well with each other.

From these results, it can be observed that the hopper inclination angle μ and the outlet

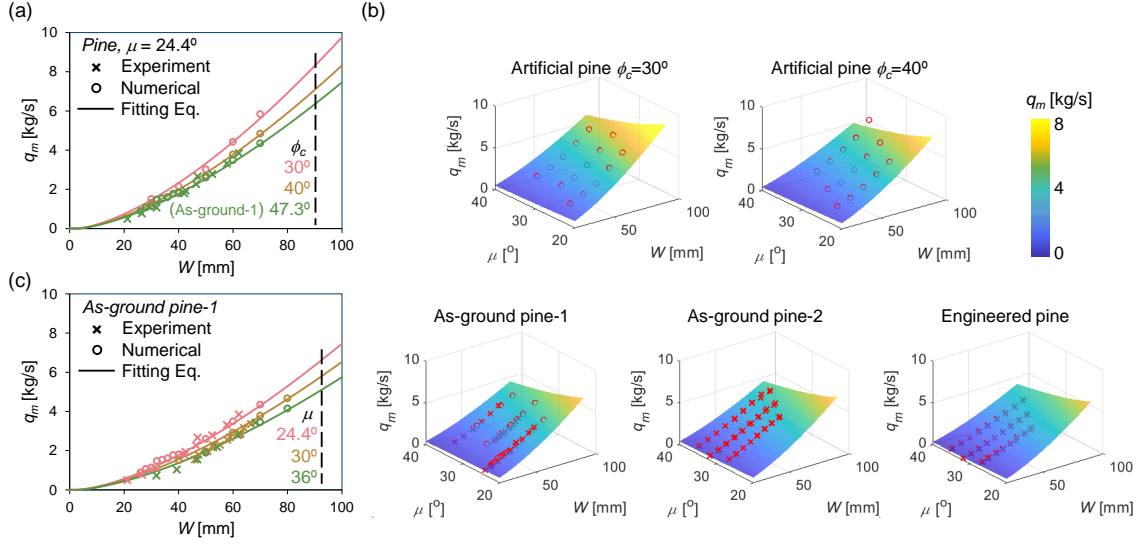


Figure 4.6: (a) Mass flow rate q_m of a fixed hopper inclination angle $\mu = 24^\circ$ for flowing pine materials (artificial and as-ground) with different friction angle $\phi_c = 30, 40$, and 47.3° . (b) Mass flow rate q_m variation with hopper inclination μ and outlet width W for different pine materials. Note that the dots here are used for fitting the equation. (c) Mass flow rate q_m of flowing the as-ground pine-1 sample with different hopper inclination $\mu = 24^\circ, 30^\circ$, and 36° . Note that “ \times ”s represent experimental measurements, circles stand for numerical results, and the lines and surfaces are predicted by the empirical equation in all plots here.

width W significantly influence the mass flow rate q_m . In contrast, the hopper wall friction ϕ_w has negligible influence from the previous study [65]. Therefore, it can be identified μ and W as the two CPPs for throughput. Note that the hopper outlet length L at the axial direction is also a CPP, but it is a constant in this study. For CMAs, the particle density ρ_p , mean particle size d_{50} (particle size at 50% percentage in Figure 4.1), and internal friction angle ϕ_c were identified from the experimental results.

Figure 4.6(a) presents the influence of the material internal friction by comparing the flow rate q_m of pine samples with internal friction angle $\phi_c = 30^\circ, 40^\circ$, and 47.3° . Note that the case with $\phi_c = 47.3^\circ$ stands for the as-ground pine-1 sample. The other two samples have the same material parameters listed in Table 2.3 except ϕ_c , and they are denoted as *artificial pine*. it can be seen that the flow rate increases with decreasing friction angle ϕ_c . Physically, this is because material with a smaller internal friction ϕ_c provides less flow resistance. Figure 4.6(c) demonstrates the effect of hopper inclination μ by comparing the

Table 4.1: Mean particle size and internal friction angle of the woody biomass samples.

	As-ground pine-1	As-ground pine-2	Engineered pine	Douglas fir 1mm	Douglas fir 2mm	Douglas fir 4mm
d_{50} [mm]	1.00	0.84	0.75	0.99	1.51	3.27
ϕ_c [°]	47.3	47.3	49.6	50.0	53.0	60.0

resulted flow rate q_m from flowing the as-ground pine-1 sample in hoppers with different inclination angle at $\mu = 24.4^\circ, 30^\circ$, and 36° . It can be observed that a slender hopper with a small μ results in a higher flow rate. This is because a smaller μ results in a larger gravity-driven discharge force $F_s = \cos \mu F_g$ and a smaller resisting force $F_f = \tan \phi_w \sin \mu F_g$ as discussed in subsection 4.3.2.

With the investigated CMAs and CPPs' influence on hopper throughput, the following empirical equation is proposed here, motivated by the British Material Handling Board [102, 103] for conventional granular materials, to predict q_m for flowing woody biomass as:

$$q_m = a \rho_p \sqrt{g} (L - k d_{50}) (W - k d_{50})^{1.5} \tan^b(\mu) \tan^c(\phi_c) \quad (4.2)$$

where ρ_p and ϕ_c are particle density and critical state internal friction angle (CMAs), respectively. L , W , and μ are hopper length (axial direction), outlet width, and hopper inclination angle (CPPs). g stands for the gravity, and the term $k d_{50}$ accounts for the effective outlet size width with d_{50} representing the mean particle size and k considering the particle shape. $k = 2.5$ was used in this study following literature [102, 103]. a , b , and c in Equation 4.2 are coefficients to be fitted. The mean particle size d_{50} and friction angle ϕ_c of the 6 samples are listed in Table 4.1. The particle density of loblolly pine and Douglas fir samples used in this study are 430 kg/m^3 and 425 kg/m^3 according to literature [29, 50, 49].

The flow rate q_m of pine samples are used as the fitting data set and the results of Douglas fir samples as the testing data set. To obtain the fitting parameters a , b , and c from the pine data set, the loss function of the gradient descent method was formulated and

implemented to minimize the empirical equation (Equation 4.2) prediction from the experimental and numerical results. The obtained optimal values are $a = 0.31$, $b = -0.55$, and $c = -0.43$. On top of experimental and numerical data points (markers), the predicted mass flow rates are shown as solid lines in Figure 4.6(a,c) and color-coded surfaces in Figure 4.6(b). For the fitting pine data set, the root mean square error (RMSE), mean absolute percentage error (MAPE), and coefficient of determination (R^2) are 0.28, 13%, and 0.95, respectively. The formulated empirical equation with the fitted coefficients was tested using the Douglas fir data set. Figure 4.7 plot the comparison of the Equation 4.2 prediction (surfaces) against the laboratory measurements (markers), and the RMSE, MAPE and R^2 are 0.20, 12% and 0.95, respectively. Even though the RMSE values for both the fitting and validation data sets are not small, the R^2 s are high. It is concluded the proposed empirical equation with fitted coefficient is robust to predicting hopper throughput for handling granular woody biomass.

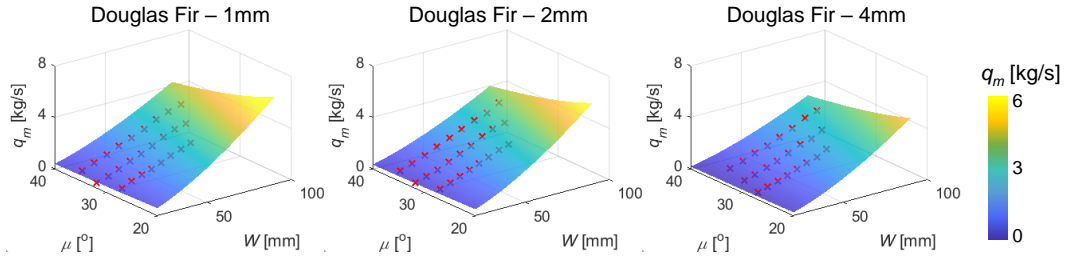


Figure 4.7: Validation of the empirical equation using Douglas fir flow data: mass flow rate q_m changing with hopper inclination μ and outlet width W , where “x”s represent experimental measurements, circles stand for numerical results, and the surfaces are prediction of the fitting equation.

4.3.4 Design guide

Through the experimental and numerical investigations, the CMAs and CPPs for wedge-shaped hopper design have been identified with respect to flow pattern, arching, and flow throughput prediction. To obtain the favored mass flow pattern, the material internal friction angle ϕ_c (CMA), hopper wall inclination μ , and wall friction ϕ_w (CPPs) need to be

carefully controlled. For arching prevention, μ and ϕ_w are important for woody biomass materials. Moreover, the throughput prediction needs hopper geometric parameters W , L , and μ (CPPs) and material attributes ρ_p , d_{50} , and ϕ_c (CMAs). In summary, the wedge-shaped hopper design guide for flowing woody biomass materials in mass-flow is mathematically expressed as:

$$MFI(\mu, \phi_w, \phi_c) > 0.3 \quad (4.3)$$

$$W > W_{cr}(\mu, \phi_w) \quad (4.4)$$

$$q_m = 0.31\rho_p\sqrt{g}(L - kd_{50})(W - kd_{50})^{1.5} \tan^{-0.55}(\mu) \tan^{-0.43}(\phi_c) \quad (4.5)$$

Note the above design guide is based on the pilot-scale hopper. The scale dependency of MFI, critical outlet width, and throughput was tested by simulating hopper flow with $10\times$ size. The MFI prediction is still valid with slight discrepancies. However, the absolute value of W_{cr} varies significantly from the pilot-scale hopper and needs further validation, and physical experiments are needed to calibrate the numerical model at larger scale. In addition, we note the critical outlet width contour was obtained by assuming materials are dry. Woody biomass with significant moisture content might result in different values for W_{cr} . The empirical throughput prediction (Equation 4.2) only includes one meso-scale parameter ϕ_c and two particle-level parameters ρ_p and d_{50} for the materials, which might be the reasons of the high RMSE values. An improvement using additional parameters on particle size and shape may capture more particle-level features and predict flow rate better.

4.4 Conclusions

The commercialization of biomass materials as a renewable energy resource has been greatly restrained by the lack of knowledge in biomass flow behavior and the design of effective handling equipment. This chapter investigated the flow behavior of milled woody biomass materials, i.e., ground loblolly pine and Douglas fir, in wedge-shaped hoppers.

Comprehensive hopper flow experiments and simulations were conducted to study the most important three design metrics: flow pattern, arching, and throughput prediction. The critical material attributes (CMAs) and critical processing parameters (CPPs) governing these three metrics were identified, and a design guide has been proposed. Key conclusions and contributions are:

1. Hopper flow patterns like mass flow and funnel flow can be quantified with the Mass Flow Index (MFI) map. The governing parameters to distinguish mass flow against funnel flow are material internal friction angle ϕ_c (CMA), hopper inclination angle μ (CPP), and hopper wall friction angle ϕ_w (CPP). The design recommendation is $MFI(\mu, \phi_w, \phi_c) > 0.3$ for obtaining mass flow.
2. Arching is governed by the competence between discharge driven force from gravity against flow resistance from material internal friction and material-wall friction. The governing parameters for milled woody biomass are hopper inclination μ and wall friction ϕ_w (CPPs). The design should satisfy $W > W_{cr}(\mu, \phi_w)$.
3. The determination of mass flow rate q_m requires particle density ϕ_p and mean particle size d_{50} (particle level CMAs), internal friction angle ϕ_c (meso-scale CMA), hopper length L , outlet width W , and inclination μ (CPPs). A robust throughput prediction for woody biomass materials is expressed in Equation 4.5.

Future research will focus on releasing constraints, e.g., materials with high moisture content and cross-scale hoppers, for a comprehensive design guideline of flowing milled woody biomass materials.

CHAPTER 5

CHARACTERIZATION AND MODELING ON THE MULTI-REGIME FLOW BEHAVIOR

5.1 Introduction

Comparing with conventional granular materials like sands, biomass particles have irregular and elongated shape, high angularity, inner pores, low stiffness, low density, at particle scale. These particle-scale properties collectively manifest as high internal friction and high compressibility of biomass materials at bulk scale [82, 84, 65]. These challenges faced by the bioenergy industry demand an in-depth understanding of the granular biomass flow behavior.

Granular biomass materials, similar to conventional granular materials, can behave like solids (e.g., during storage), liquids (e.g., when flowing in hoppers and feeders), and gases (e.g., if strongly agitated). Its flow behavior can be categorized into three typical flow regimes defined by the particle interaction mechanisms [60, 61, 120, 121]: 1) quasi-static regime, where friction and interlocking among particles dominates material bulk behavior, 2) dense flow regime, where both particle friction and collision control the flow behavior, and 3) dilute flow regime, where particles interact mainly by collision. As argued by Campbell [61], dilute flow regime seldom exists outside the laboratory, and most flows in handling granular biomass materials are either quasi-static or dense. Therefore, characterization and modeling of the granular biomass flow behavior in each of the two regimes and the transition between the two regimes are desired [32].

Over the decades, physical characterization studies have been conducted to understand the flow behavior of biomass feedstock, including 1) particle scale characterization focusing on particle size and shape and their relation with material flowability [14, 13, 16, 15,

122, 82], 2) meso-scale or lab-scale characterization on bulk properties like bulk density, elasticity, and shear behavior [17, 12, 122, 18, 83, 13, 19, 20, 22, 85, 84], and 3) macro-scale or equipment-scale characterization of flow behavior in hoppers [17, 7, 23, 24] and screw feeders [17, 6, 123, 124]. These characterizations focus on the particle and bulk properties using quasi-static experiments and the efforts to correlate them with large-scale flow behavior (e.g., hopper flow), which may partially or entirely flow in a dense regime, weaken their conclusion. Meanwhile, characterizations have been conducted in dense flow regime through vertical and inclined chutes, rotary drum, and customized ring shear cell on various conventional granular materials (e.g., glass beads, polystyrene beads, sands, agricultural seeds) [125, 129, 130, 131, 121, 132, 133, 134, 135, 126, 127, 128]. Yet, the characterization on the dense flow behavior of granular biomass materials is missing.

Modeling and simulations base on both the Discrete Element Method (DEM) and the continuum mechanics methods, in parallel with experiments, have been used to explore the flow physics and to optimize the design of biomass material handling equipment. Recent DEM studies successfully simulated the flow of milled biomass with resolved particle shapes [29, 113, 76] and sophisticated contact laws [114, 89], indicating that DEM is advantageous for capturing particle-particle interactions and modeling discontinuous flow media at the cost of expensive computation [28, 89]. Continuum mechanics methods like the Finite Element Method (FEM) with a robust constitutive model are preferred for industrial scale granular flow simulations and are good at the parameterization of materials [89]. FEM have been successfully used to simulate various lab-scale tests (e.g., oedometer, ring shear, axial shear) and salient granular flow phenomena in pilot-scale material handling tests (e.g., hopper flow and arching, avalanche in rotary drum) by using modified Drucker-Prager/Cap model [12], Gudehus-Bauer hypoplastic model [65, 88, 89], Cam-Clay model [21, 136], and NorSand model [32]. However, all these constitutive models were formulated to capture the quasi-static mechanical behavior and may not be effective in simulating dense flow with a high shear rate [89]. A few constitutive models, for example, $\mu(I)$ rhe-

ology model [137] and Nonlocal Granular Fluidity model [138, 139, 140, 141], have been successfully formulated to simulate the dense flow behavior of conventional granular materials [132, 142, 143, 144, 145]. Yet, the applicability of these models for modeling granular biomass materials is not thoroughly examined [32]. Multi-regime constitutive models that can capture the granular flow behavior of milled biomass in both quasi-static and dense-flow regimes are still greatly desired.

This chapter attempts to bridge the gap of multi-regime flow characterization and modeling of granular biomass materials. The flow behavior of loblolly pine chips with different inclination angles and initial velocities were first investigated using a customized inclined plane tester. The run-out velocity and the material thickness profile along the plane after flow stops were measured to distinguish and evaluate the dense flow and quasi-static behaviors. Then, the Gudehus-Bauer hypoplastic model, which is a quasi-static model and has been employed successfully to simulate the flow of milled biomass [65, 88, 89], was used to simulate the inclined plane flow experiments. A new constitutive model, the Drucker-Prager- $\mu(I)$ (DP- $\mu(I)$) model that was formulated by combining a quasi-static model (DP) and a dense flow model ($\mu(I)$), was implemented and used to simulate the same set of inclined plane flow experiment. The dense flow dominant steady flow behavior and the stopping thickness, which was primarily determined by quasi-static flowability, predicted by the two models were evaluated by comparing against experimental measurements. The scaling law of pine chips flowing on an inclined plane was reported.

5.2 Methods

5.2.1 Inclined plane experiment

¹ The multi-regime flow behavior of granular biomass materials was investigated with a customized inclined plane experiment. Figure 5.1(a) presents the setup of the experiment, where a material storage box and an inclined ramp are attached on an aluminum frame.

¹The experimental work in this chapter were conducted by the Idaho National Laboratory.

The box sidewall facing the ramp can be slid upward to initiate the flow. The angle of inclination θ can be adjusted by raising either the two legs of the storage box or the end of the ramp. The dimension of the experimental setup is shown in Figure 5.1(a, b). A layer of biomass particles were glued on the plane to realize the no-slip boundary condition. The material used in this work is loblolly pine chips, which was hammer-milled until the particles passed a retention sieve of 6 mm and dried in a rotary drum until a moisture content of around 6% (room moisture content) was achieved. The size and shape of the sample is shown in Figure 5.1(c), from the particle size distribution the particle mean size $d_{50} = 0.82$ mm, $d_{10} = 0.38$ mm, and $d_{90} = 1.79$ mm, were obtained respectively. Note that the procedures and devices to obtain the pine samples have been elaborated in detail in the previous study [12].

In each experimental trial, the pine chips were first loaded into the storage box followed by sliding the gate to a preset position with a certain gate opening height h_0^0 . After the flow was initiated, the run-out velocity was calculated by dividing the ramp length L (1.22 m) over the time that the material takes to reach the end of the ramp using a stopwatch. After the flow stopped, the thickness of the material at the middle symmetric surface along the length of the ramp was measured by series of the laser-based distance sensors (Wenglor OPT2011). A representative experiment with an inclination angle of $\theta = 29.5^\circ$ is demonstrated in Figure 5.2(a) with a highlight of the region for thickness measurement.

5.2.2 Numerical modeling

The Coupled-Eulerian Lagrangian approach in FEM is adopted in this chapter. As demonstrated in Figure 5.1(b), the numerical model was developed with the same size as the experiment setup, except that the initial height of the material H has a limit due to the height of the storage box in experiments but can vary in simulations. Given the setup is symmetric in the y direction, only half of the domain was modeled with a symmetric boundary condition applied to the symmetric surface. No-slip boundary condition was applied to the

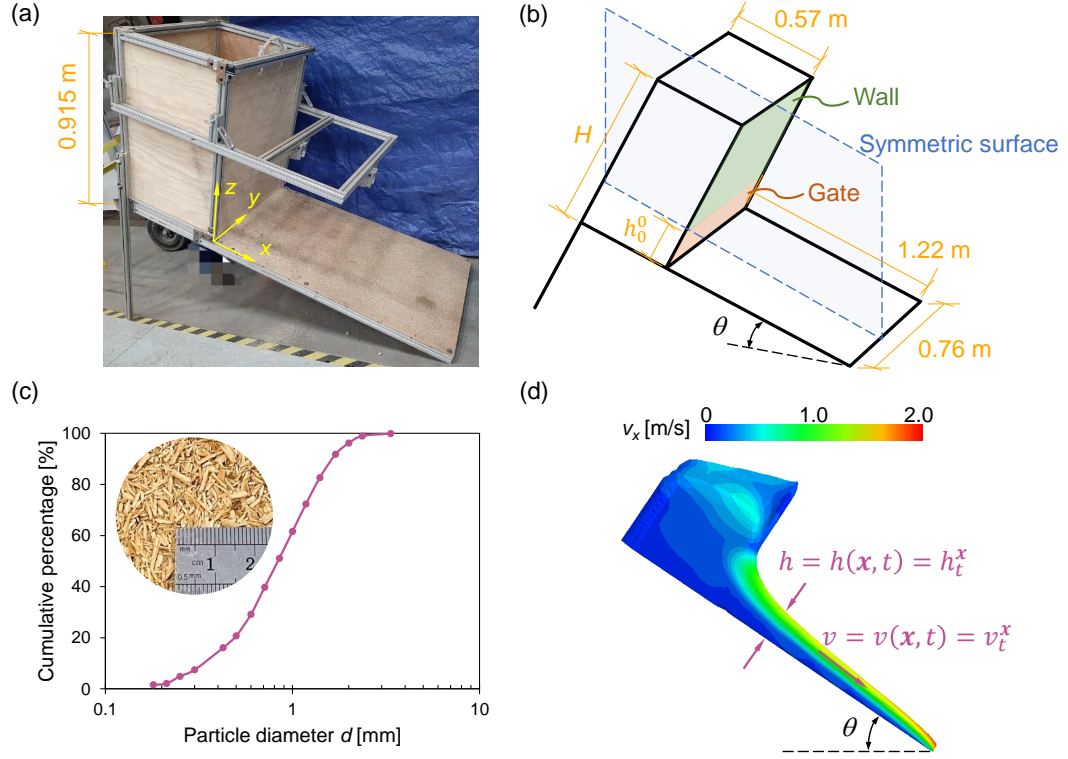


Figure 5.1: (a) The experimental inclined plane setup with a local coordinate system. A layer of biomass particles was glued on the ramp to realize the no-slip boundary condition. (b) Schematic view of the numerical model. Note the “Gate” was opened by releasing boundary constraints in modeling instead of sliding the side wall as in experiments. The dimensions of the experiment setup and the numerical model are the same except that the material height H in experiments is limited by the height of the storage box (0.915 m) while the H in numerical models can surpass the limit. (c) Particle size distribution of the loblolly pine chips used in this chapter and a photo demonstrating particle size and shape. (d) A velocity profile at the symmetric middle surface shows the variables measured in simulations, where h represents the thickness of the material and v stands for the flow velocity along the x direction. Both variables are spatially distributed and evolve with time.

ramp. All these boundary conditions were applied directly on the Eulerian mesh to avoid computationally intensive contact detection near the corners.

Each simulation consists of two steps: 1) the gravity was smoothly applied to the material followed by resting until the stress distribution stabilizes, and 2) the boundary constraints applied to the nodes located in the “Gate” area, marked in Figure 5.1(b), were released to initiate the flow. All simulations were stopped until the flow completely stopped with a fixed material thickness profile along the ramp. A representative simulated response

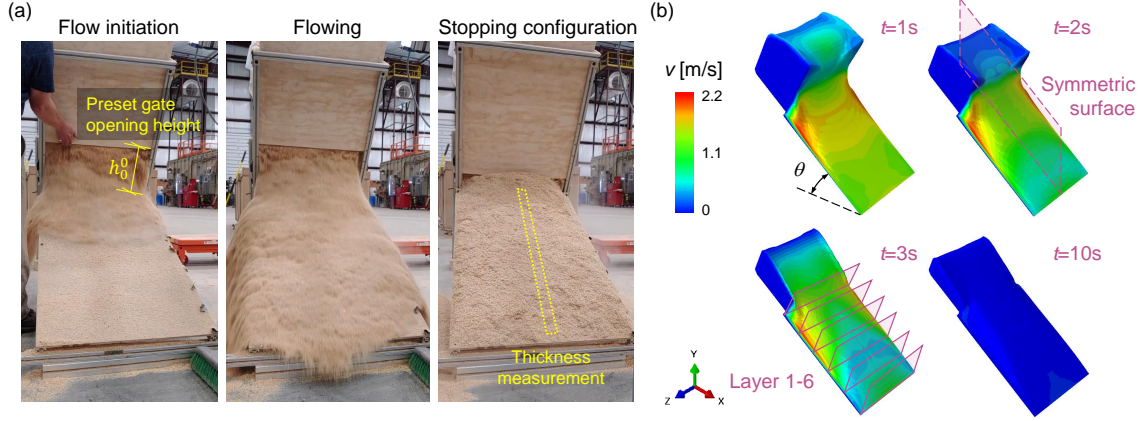


Figure 5.2: Experimental and numerical results showing the flow of milled biomass. (a) A demonstration of experimental steps of the inclined plane flow tests and the region of material thickness measurement. (b) Modeling predicted velocity distribution of a flow test with an inclined angle of $\theta = 29.5^\circ$ and a gate opening of $h_0^0 = 0.35$ m. Note the 6 layers along the ramp were used to extract quantitative modeling results.

($\theta = 29.5^\circ, h_0^0 = 0.35$ m) is shown in Figure 5.2(b) with the velocity magnitude color-coded.

Figure 5.1(d) shows the predicted velocity distribution at the middle symmetric surface during flow for the case of $\theta = 34^\circ, h_0^0 = 0.31$ m. Note that both thickness h and velocity v vary in space and time, and $h(\mathbf{x}, t) = h_t^x$ and $v(\mathbf{x}, t) = v_t^x$ is used with the superscript indicating the location and the subscript standing for time. Given the most important variables are the h and v during steady flow and after the material fully stops, without further specific notice, v is used to stand for the steady-flow velocity at the top of the flow and along the x direction, v^m to denote velocity at the middle symmetric surface, h_{std} and h_{stop} to represent the steady-flow thickness and stopping thickness at the symmetric surface, respectively. Moreover, similar to experiments where the material thickness along the middle ramp was measured by a few sensors shown in Figure 5.2(a), the numerical results were extracted on the 6 layers from the beginning to the end of the ramp shown in Figure 5.2(b), where layer 1 is located at the beginning of the ramp while layer 6 sits at the end.

5.2.3 Constitutive models

Granular materials are ubiquitous and a great amount of constitutive models have been proposed to simulate their mechanical behavior across multiple regimes. For granular biomass materials, the start-of-art constitutive models was reviewed based on different theoretical frameworks [32]. Models based on hyperplastic (i.e., elastoplastic) theory without incorporating critical state theory (e.g., Mohr-Coulomb and Modified Drucker-Prager/Cap model) either cannot capture the high compressibility of biomass or have over-dilation issues when the compression is vanishing (e.g., material near the outlet of a hopper). Fluid mechanics based rheology models (e.g., $\mu(I)$ and Nonlocal Granular Fluidity Model) are challenged to simulate the material flow behavior at a low shear rate. The hyperplastic models (e.g., Cambridge-type models) and the hypoplastic models (e.g. Gudehus-Bauer model [45, 46]) with embedded critical state theory have high potential to capture the important flow features of biomass materials. In particular, the G-B hypoplastic model has been successfully used to simulate granular biomass material flowing in hoppers [65, 88]. Yet, the quasi-static nature of the G-B hypoplastic model questions its robustness for modeling material at a high shear rate [89]. In this work, both the G-B hypoplastic model and the Drucker-Prager- $\mu(I)$ (DP- $\mu(I)$) model are used to simulate the multi-regime flow behavior of the granular biomass materials.

Hypoplastic model

The G-B hypoplastic model [45, 46] incorporates the critical state theory and is capable of capturing most of the important flow characteristics of the granular biomass materials (e.g., density dependency, shear dilation (respectively, compression) for dense (respectively, loose) packing, and high internal friction. The explicit stress integration of hypoplasticity also renders it computationally robust and efficient for simulating large deformation problems. The formulation, implementation, and validation have been reported in details in chapter 2, and the coded Abaqus User Material Subroutine (VUMAT) has been open-

sourced on Github. The material parameters of the targeted pine chips in this chapter, listed in Table 2.3 as the “as-ground” sample, were calibrated by combining laboratory experiments and single-element FEM simulations (Table 2.3).

DP- $\mu(I)$ model

The DP- $\mu(I)$ model is formulated by combining traditional Drucker-Prager model to account for quasi-static behavior and the $\mu(I)$ rheology model to account for shear rate dependency. Its mathematical formulation, including yield criteria, hardening law, and plastic potential, is listed in Table 5.1. The DP- $\mu(I)$ model extends the DP yield criteria (T6) by changing the fixed friction coefficient μ into a variable that depends on inertial number I (T3), which is a function of shear rate $\dot{\gamma}$ and pressure p . Figure 5.3(a,b) sketch the cone-shaped yield surface in the principle stress space and the circles at different inertial numbers in the π plane. These circles indicate the DP- $\mu(I)$ model only takes two stress invariants (i.e., pressure p and deviatoric stress q) into account, as opposed to the G-B hypoplastic model, which has a rounded triangular shape in the π plane and has all three stress invariants in yield surface (i.e., pressure p , deviatoric stress q , and Lode angle). Note that the hypoplastic model formulation implicitly embeds the yield criteria instead of using an explicit yield function, the readers can refer to Goddard [146] for details. Figure 5.3(c) demonstrates the variation of the material friction coefficient, defined as $\mu = q/p$, with respect to the inertial number I . As defined in Equation T3 (Table 5.1), inertial number I is dominated by shear rate $\dot{\gamma}$ for a specific granular material. When material is sheared in quasi-static regime (i.e., the shear rate is small enough), the friction coefficient $\mu = \mu_s = \tan \phi_c^s$, where ϕ_c^s is the internal friction angle at critical state (Figure 5.3(a)) and can be measured from quasi-static shear tests (e.g., ring shear, triaxial compression). When shear rate increases, the friction coefficient increases hyperbolically until it reaches an upper bound μ_2 . The hyperbolic shape is determined by the inertial coefficient I_0 (Figure 5.3(c)). In addition to the criteria, a nonlinear elasticity formulation was also adopted for the DP- $\mu(I)$ model as

observed from the oedometer tests of pine chips [12] (shown in Figure 5.3(d) and T5 in Table 5.1).

Table 5.1: Fomulation of DP- $\mu(I)$ model.

Mean & deviatoric stress	$p = \frac{1}{3}\text{tr}\boldsymbol{\sigma}, \quad q = \sqrt{\frac{3}{2}}\ \boldsymbol{\sigma} - p\mathbf{I}\ $	(T1)
Mean & deviatoric strain	$\epsilon_v = \text{tr}\boldsymbol{\epsilon}, \quad \epsilon_s = \sqrt{\frac{2}{3}}\ \boldsymbol{\epsilon} - \frac{1}{3}\epsilon_v\mathbf{I}\ $	(T2)
Inertial number	$I = \dot{\gamma}d\sqrt{\frac{\rho_p}{p}}$	(T3)
Plastic potential	$G = q - \tan(\psi)p$	(T4)
Elasticity	$\boldsymbol{\sigma} = 2G(p)\boldsymbol{\epsilon} + \lambda(p)\text{tr}(\boldsymbol{\epsilon})\mathbf{I}$	(T5)
Yield criterion (DP)	$F = q - \mu p$	(T6)
Hardening law ($\mu(I)$)	$\mu = \mu_s + \frac{\mu_2 - \mu_s}{I_0/I + 1}$	(T7)
Non-associated flow rule	$d\boldsymbol{\epsilon}^p = \Delta\lambda \frac{\partial G}{\partial \boldsymbol{\sigma}}$	(T8)
$\boldsymbol{\sigma}, \boldsymbol{\epsilon}$: stress & strain tensors	G, λ : Lamé parameters	
F : yield surface	I, I_0 : inertial number, inertial coefficient	
μ : friction coefficient	μ_s, μ_2 : lower & upper bounds of μ	
$\Delta\lambda$: magnitude of plastic strain	$\dot{\gamma}$: total deviatoric strain rate, $\dot{\gamma} = \sqrt{2}d\epsilon_s$	
ψ : dilation angle	d, ρ_p : mean particle size & particle density	

Different from the G-B hypoplastic model, which uses an explicit stress integration, the DP- $\mu(I)$ model is formulated in the framework of hyperplasticity and requires an implicit stress integration. Given the model hardens isotropically, stress integration can be performed using a return mapping algorithm in strain invariant space following Borja and Andrade [147]. Mathematically, the main goal of stress integration is to find a stress state $\boldsymbol{\sigma}$ and a plastic multiplier $\Delta\lambda$ that satisfy the yield criteria for a given strain increment $d\boldsymbol{\epsilon}$. The given total strain increment $d\boldsymbol{\epsilon}$ includes both an elastic part $d\boldsymbol{\epsilon}^e$ and a plastic part $d\boldsymbol{\epsilon}^p$, and they are determined by dissipating the following residual vector \mathbf{r} as

$$\mathbf{r} = \mathbf{r}(\mathbf{x}) = \begin{Bmatrix} d\epsilon_v^e - d\epsilon_v^{e,tr} + \Delta\lambda\partial_p G \\ d\epsilon_s^e - d\epsilon_s^{e,tr} + \Delta\lambda\partial_q G \\ F \end{Bmatrix}; \quad \mathbf{x} = \begin{Bmatrix} p \\ q \\ \Delta\lambda \end{Bmatrix}, \quad (5.1)$$

where $d\epsilon_v^p = \Delta\lambda\partial_p G$ and $d\epsilon_s^p = \Delta\lambda\partial_q G$ was used, in which the superscripts e, p , and tr represent the elastic, plastic, and trial components and the subscript v, s denote volumetric

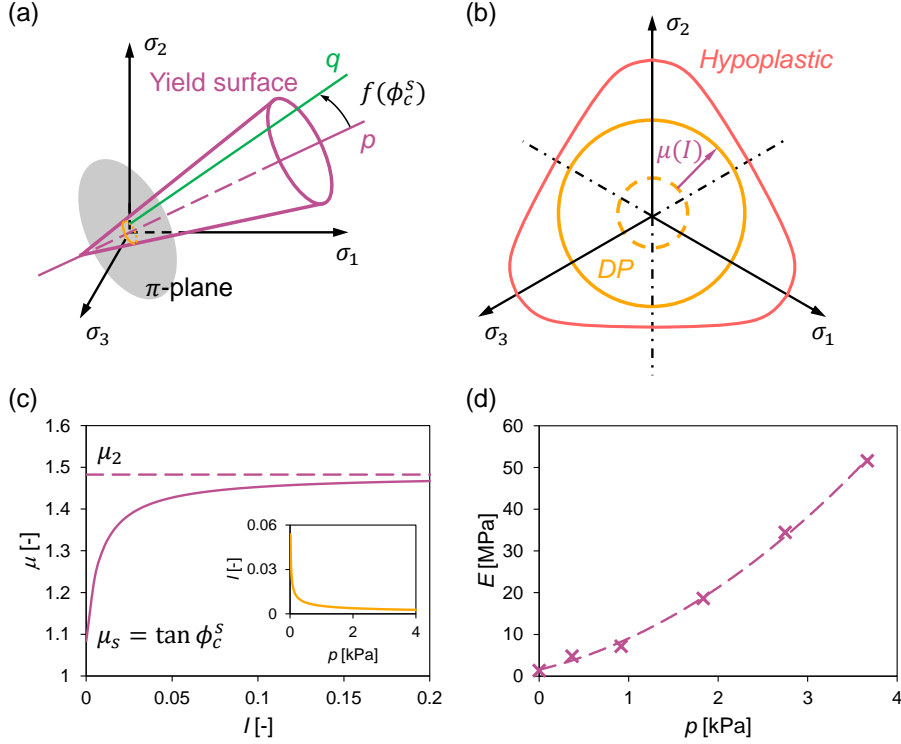


Figure 5.3: Sketch of DP- $\mu(I)$ model. (a) Yield surface in the principal stress space with demonstration of the π -plane and the friction angle in quasi-static regime ϕ_c^s . (b) Comparison of yield surfaces between G-B hypoplastic model and the DP- $\mu(I)$ model on the π -plane. Note the size of circular shaped yield surface in the π -plane for the DP- $\mu(I)$ model varies according to the value of dimensionless inertial number I , which is a function of shear rate. (c) A demonstration of friction coefficient μ evolving with the inertia number I at $\mu_s = \tan \phi_c^s = \tan 39.2^\circ$, $\mu_2 = \tan 56^\circ$, and $I_0 = 0.008$. The subplot presents that the inertia number I is a function of the pressure p with a fixed shear rate of 10 s^{-1} . (d) Elastic modulus E as a function of mean stress p .

and deviatoric components, respectively.

A local Newton iteration is needed to satisfy $\mathbf{r} = \mathbf{0}$ gradually. The stress invariants and Lagrange multiplier $\Delta\lambda$ is iteratively updated via:

$$\mathbf{x}_{n+1} = \mathbf{x}_n - \frac{\mathbf{r}(\mathbf{x}_n)}{\mathbf{r}'(\mathbf{x}_n)}, \quad (5.2)$$

where $\mathbf{r}'(\mathbf{x})$ stands for the local Jacobian. The step-by-step algorithm is summarized in Algorithm line 10, and this algorithm was implemented in an Abaqus User Material Subroutine (VUMAT).

Algorithm 1: Stress update in a representative time step with return mapping

```

1 Get stored state variables  $p, \mu$ , stress  $\sigma$ , and strain increment  $d\epsilon$  from previous step;
2 Calculate  $E = E(p), G, \lambda$ ;
3 Initialize  $\sigma^{tr}, p^{tr}, q^{tr}, I^{tr}$ ;
4 Compute  $F = q^{tr} - \mu(I^{tr})p^{tr}$ ;
5 if  $F < tolerance$  then
6   |  $(\cdot)_{t+1} = (\cdot)^{tr}$ , exit
7 else
8   | while  $F > tolerance$  do
9     | Calculate  $\mathbf{r}_n, \mathbf{r}'_n, \mathbf{r}'_{n-1}, \mathbf{x}_{n+1}, \mu_{n+1}, F_{n+1}$ 
10 Convert  $p_{n+1}$  and  $q_{n+1}$  to  $\sigma_{n+1}$ 

```

The DP- $\mu(I)$ model consists of 8 material parameters. Among them, the elasticity parameters E and ν were obtained from oedometer tests and were reported in the previous work [12]. The mean particle size d was measured from the sieve analysis (Figure 5.1(c)) and the particle density was estimated using the wood block density before milling [65]. μ_s measures the friction resistance in quasi-static regime and was determined as $\mu_s = \tan phi_c^s$, i.e., the tangent of the critical state internal friction angle obtained from the Schulze ring shear tests [12, 65]. The friction coefficient upper bound μ_2 and the inertial number coefficient I_0 were calibrated by comparing the numerical prediction of the stopping thickness h_{stop} and the run-out velocity of the inclined plane flow tests with the experimental measurements (see details in subsection 5.3.2). The dilation angle ψ was assumed as zero to avoid material dilation. The values of calibrated DP- $\mu(I)$ parameters are listed in Table 5.2.

Table 5.2: Calibrated DP- $\mu(I)$ model parameters for the loblolly pine sample.

E [MPa]	ν [-]	d [mm]	ρ_p [kg/m ³]	I_0 [-]	μ_s [-]	μ_2 [-]	ψ [°]
Figure 5.3(d)	0.4	0.82	430	0.0003-0.008	0.8156	1.4826	0

To validate the implementation and the calibrated parameters of the DP- $\mu(I)$ model, the predicted stopping thickness h_{stop} along the ramp and velocity of the inclined plane tests are compared with the experimental measurements shown in Figure 5.5. Note that

μ_2 and I_0 was calibrated using a single gate opening height h_0^0 at each inclination angle (i.e., a single point on each line in Figure 5.5(b)) and validated the model with all other different gate openings h_0^0 (i.e., other points in Figure 5.5(b)). Details will be discussed in subsection 5.3.2.

5.3 Multi-regime flow behavior

5.3.1 Typical flow response

Figure 5.4 shows representative flow responses predicted by a single simulation case with an inclination angle of $\theta = 34^\circ$ and a gate opening height of $h_0^0 = 0.31$ m using the G-B hypoplastic model. A steady flow stage and the complete stop of flow can be identified from both the velocity response (Figure 5.4(a)) and the thickness response (Figure 5.4(d)), where different colors code the extracted results from layer 1 to 6 (Figure 5.2(b)). During the steady flow stage, both the velocity v and the thickness h are stable across all layers, and the steady flow thickness h_{std} and the steady flow velocity v^m were extracted at the surface of the middle symmetric boundary. After the material flow stopped with zero velocity, the stopping thickness h_{stop} was extracted. Figure 5.4(b) shows the distribution of steady flow thickness along the y-axis of the inclined plane for the 6 layers at $t = 6$ s, and the curves are color-coded with the velocity magnitude. Similarly, Figure 5.4(e) presents the stopping thickness h_{stop} distributed along the width.

To evaluate the flow behavior in quasi-static and dense flow regimes and to compare prediction against experimental measurements, representative values of flow responses were extracted from Figure 5.4(a,b,d,e). Figure 5.4(c) demonstrates the velocity along the ramp in x direction (from layer 1 to 6) during the steady flow period, from which we can clearly see the velocity magnitudes from layer 2 to 5 are stable. The averaged v^m of those layers were calculated as the steady flow velocity scalar. Figure 5.4(f) presents the material thickness on the symmetric surface along the ramp during the steady flow stage and after the material flow stopped. Both predictions at the two stages show an attenuated trend, and

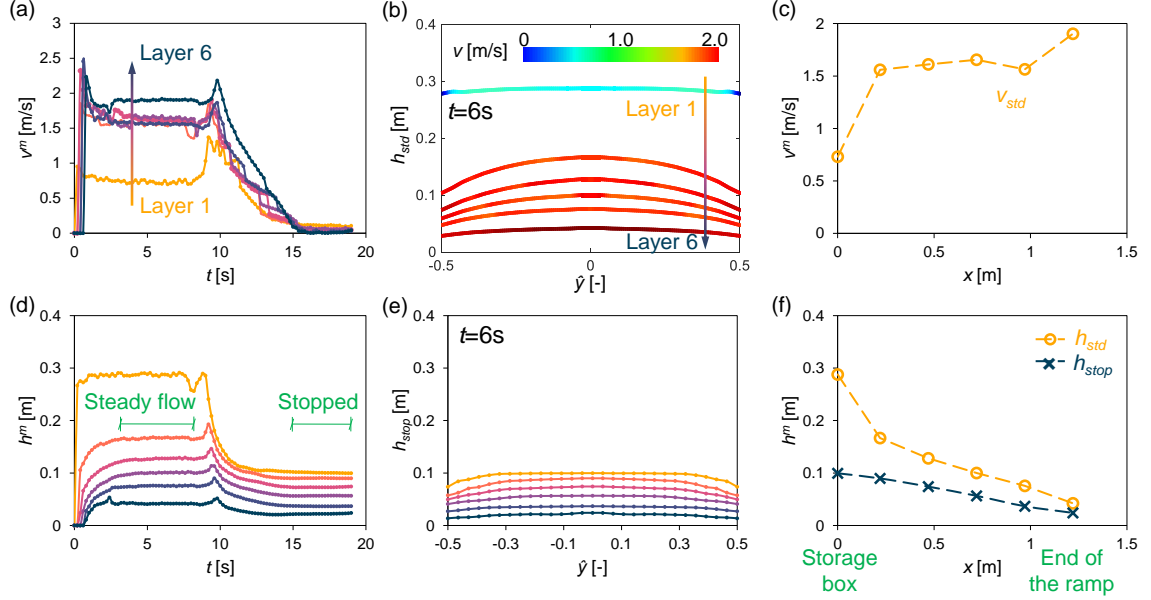


Figure 5.4: Demonstration of the flow responses ($\theta = 34^\circ$, $h_0^0 = 0.31$ m) calculated by G-B hypoplastic model. (a,d) Predicted velocity and material thickness at the middle symmetric surface evolving with time, where different colors represent different layers. Note the velocity across the thickness of the flowing material is not a constant, only the velocity at the top flow surface is presented. (b,e) The steady-flow thickness h_{std} and the stopping thickness h_{stop} profiles along the width of the ramp, where \hat{y} is the normalized length along the y direction. Note that the color in (b) quantifies the velocity magnitude and the color in (e) stands for different layers. (c,f) The steady-flow velocity v_{std}^m , the steady-flow thickness h_{std} , and the stopping thickness h_{stop} along the length of the ramp, where $x = 0$ and $x = 1.22$ m are the start and the end of the ramp, respectively.

the values at the middle of the ramp were used as the representative steady flow thickness h_{std} and stopping thickness h_{stop} for each inclination angle θ and gate opening height h_0^0 . It is observed that the flow responses calculated by the DP- $\mu(I)$ model have similar trends as the G-B hypoplastic model except for the stopping thickness h_{stop} . The difference is discussed in subsection 5.3.3.

5.3.2 DP- $\mu(I)$ model calibration and validation

The DP- $\mu(I)$ model parameters μ_2 and I_0 , which determine the shear rate-dependent dense flow behavior, were calibrated from the inclined plane flow experiments as described in subsubsection 5.2.3. For each inclination angle θ , one gate opening height h_0^0 was fixed

(e.g., $\theta = 34^\circ$, $h_0^0 = 0.31$ m) and (μ_2, I_0) values were fitted through trial-and-error of simulations to match experiments measured h_{stop} and v^m . With the calibrated (μ_2, I_0) and the rest material parameters listed in Table 5.2, these parameters were then validated by comparing numerical predictions against experimental measurements for the inclined plane flow tests with each θ and variated gate opening h_0^0 . Figure 5.5 presents the comparison of the stopping thickness and the steady flow velocity for different inclination angles θ and gate opening heights h_0^0 . It is clear that the multi-regime flow responses predicted from the DP- $\mu(I)$ model agree well with the experimental measurements. Given the challenge of measuring flow velocity at the steady state in experiments, the experimental data shown in Figure 5.5(b) are run-out velocities (i.e., material front propagating velocities). Replacement of the steady flow velocity with the run-out velocity should be valid as the flow rapidly reached the steady state during experiments, according to Pouliquen [125].

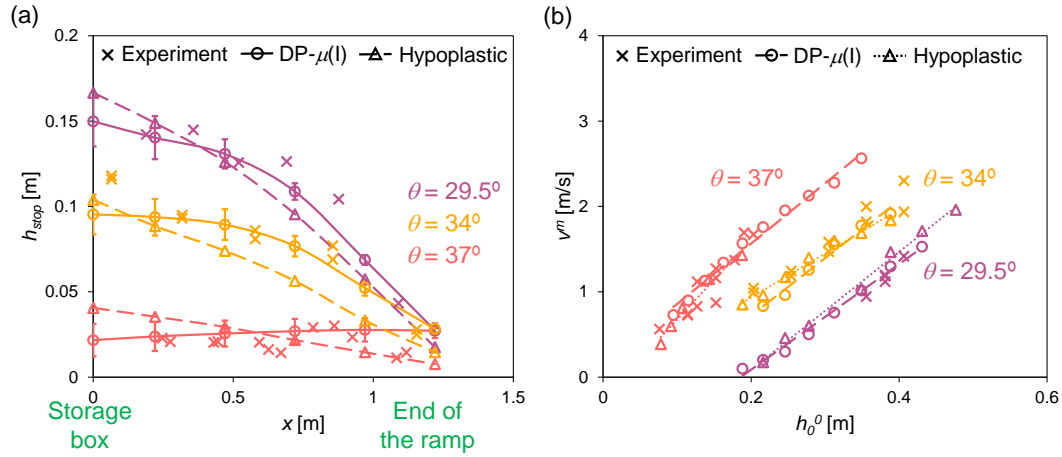


Figure 5.5: (a) The stopping thickness h_{stop} along the length of the ramp x for the inclined angle $\theta = 29.5^\circ$, 34° , and 37° . Error bars represent the variation from cases with different gate opening heights h_0^0 . The error bars predicted from the G-B hypoplastic model are omitted because the predicted variations are negligible. (b) Steady flow velocity at the top symmetric surface v^m from various inclined angles θ and gate opening heights h_0^0 . Note that the experimental v^m are the run-out velocities. The marker “x” stands for experimental measurements, “o” represents results from the DP- $\mu(I)$ model, and “Δ” means predictions from the G-B hypoplastic model.

5.3.3 Model comparison

Figure 5.5 also compares the predictions of the G-B hypoplastic model (the “ \triangle ”s) and the DP- $\mu(I)$ model (the “o”s) against the physical experimental data (the “ \times ”s). Figure 5.5(a) indicates that both models can capture the stopping thickness h_{stop} with the same magnitude as the experiments. However, the prediction from the DP- $\mu(I)$ model matches better than the G-B hypoplastic model prediction on capturing the shape of the material configuration after stopping. The hypoplastic model predicts an attenuated shape even if the inclination angle is large (e.g., $\theta = 37^\circ$) when both experiment and the DP- $\mu(I)$ model result a relatively flat shape. Moreover, the shape of the stopping profiles predicted by the hypoplastic model has a smaller curvature than experimental measurements and the DP- $\mu(I)$ model predictions. It can be concluded that the newly formulate DP- $\mu(I)$ model performs better in capturing the stopping thickness than the G-B hypoplastic model. However, it can also be found that the hypoplastic model is more robust than the DP- $\mu(I)$ model demonstrated from the error bars in Figure 5.5(a). These error bars represent the variations of h_{stop} calculated from different gate opening heights h_0^0 using the DP- $\mu(I)$ model. The error bars on the hypoplastic h_{stop} were omitted because the variations are negligible, which matches with experimental observation. The large variations predicted by the DP- $\mu(I)$ model stem from the shear rate rate dependent flow response, i.e., different gate openings h_0^0 induce different magnitudes of shear rate, which results in different material friction coefficients and is reflected by the variation of the material profile after flow stops.

Figure 5.5(b) presents the flow velocity v^m variation due to the change of gate opening h_0^0 . The predictions from both models match well with the experimental results. Generally, the flow velocity increases linearly with the increasing gate opening for a fixed inclination angle θ .

5.3.4 Flow profile

The flow profiles predicted at different inclination angles θ by the G-B hypoplastic model are presented in Figure 5.6. Figure 5.6(a,b) show the stopping material profile $h_{stop} - x$ and steady flow profile $h_{std} - x$ at different inclinations θ , where the color codes the material thickness. Note that the average values of both profiles due to different gate opening heights h_0^0 are presented. It is observed that h_{stop} has negligible variations while h_{std} has relatively larger variations, which correlates to the scaling law to be discussed in subsection 5.3.5. Both flow profiles show all flows are “attenuating” (i.e., the thickness decreases along the ramp) except for the case of $\theta = 40^\circ$, which corresponds to the zero stopping thickness $h_{stop} = 0$. Similar trend was observed in experiments, where the non-attenuating flow (plane flow) existed for the cases with $\theta = 37^\circ \sim 40^\circ$. This phenomenon is different from the previous studies [125, 131, 137], where the plane flow was observed within a wide range of θ . This discrepancy fundamentally stems from the high internal friction angle of pine chips as compared to the glass beads used in their studies with a low internal friction angle. For pine chips, the plane flow only exists when the inclination angle θ is close to the internal friction angle. For all other cases with an inclination angle smaller than the internal friction angle, pine chips flow in an attenuated way (i.e., a static layer exists between the flowing layer and the plane demonstrated as the deep blue zone in Figure 5.1(d)). When the inclination angle exceeds the internal friction angle, the flow becomes “accelerating” and no steady flow exists.

Figure 5.6(c) presents the numerical and experimental material thicknesses at the middle of the ramp ($x = 0.61$ m) against the plane inclination θ . The trend is different from what was reported by Pouliquen [125] because of different experimental procedure. For large inclination with small material thickness, Pouliquen used the same procedure as the conducted experiments in subsection 5.2.1 to obtain the $h - \theta$ relation, and this procedure can be denoted as the $h_{stop}(\theta)$ method. For small inclination with large material thickness, Pouliquen initialized the test by a fixed gate opening with zero inclination, followed by

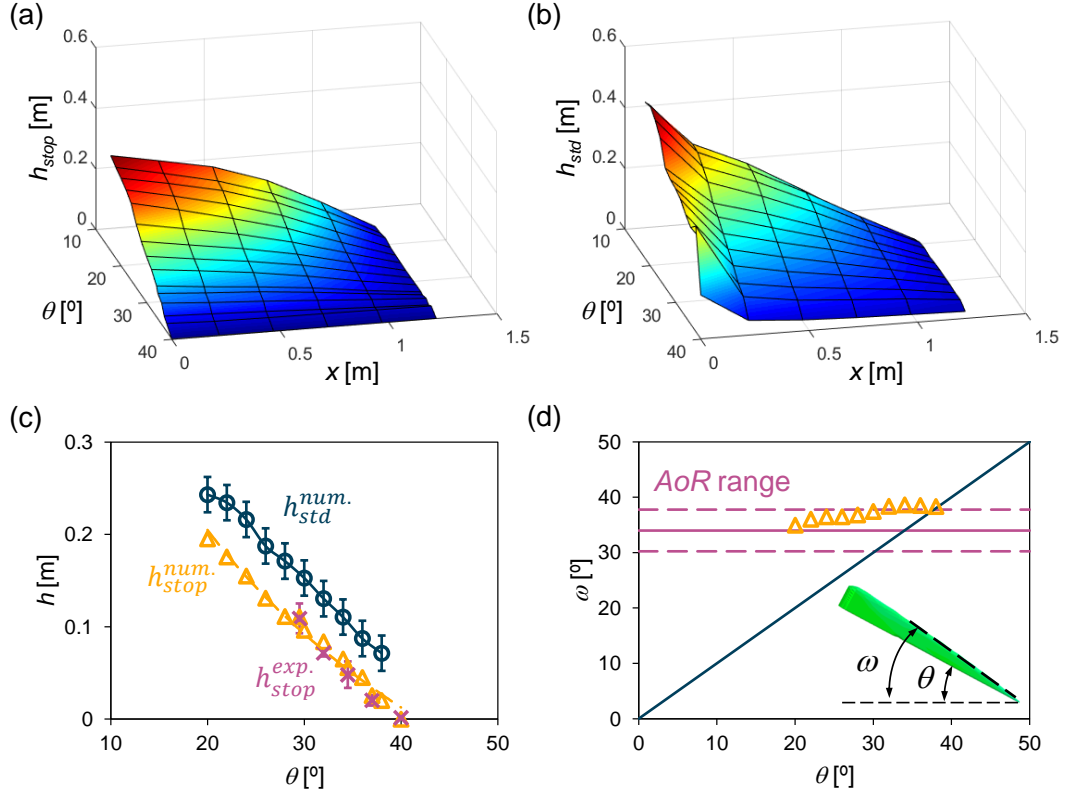


Figure 5.6: Flow profiles with various inclined angles θ predicted from the G-B hypoplastic model. (a,b) The stopping thickness h_{stop} and the steady flow thickness h_{std} distributed along the ramp x at different inclined angles θ . (c) Material thickness at the middle ramp as a function of inclined angle θ . The error bars of different steady flow thickness stem from the different gate opening heights h_0^0 . (d) Angle between the material top surface and the horizontal surface ω for varied inclined plane angle θ .

gradually increasing the inclination until a stable flow was observed. this procedure can be denoted as the $\theta_{stop}(h)$ method. The adopted two methods by Pouliquen results in a curved $h - \theta$ relation with an infinite value of thickness when the inclination approaches zero [125]. However, in this chapter, only the $h_{stop}(\theta)$ method was used for each θ and a close to linear relationship was obtained for $h - \theta$.

It should be pointed out that the inclined plane test is a varied version of the static Angle of Repose (AoR) test. As shown in Figure 5.6(d), the angle between the horizontal surface and the tangent of the material surface close to the end of the ramp was extracted when the material stopped flowing. It is denoted as ω and its value was obtained for each inclination. It can be seen that ω keeps almost to a constant for different inclinations and

its value equals to the AoR measured for the pine chips. This indicates the function of the plane is equivalent to an heap of pine chips. Intuitively, the AoR test is a specific case of inclined plane test with an inclination angle of $\theta = 0^\circ$.

In an idealized situation with a long enough plane and a high enough gate opening, steady flow exists when the plane inclination θ is within the range of zero to material internal friction angle ϕ_c , above which the flow becomes “accelerating”. In reality, the existence of steady flow is limited by the plane inclination, length, gate opening, and the material’s internal friction angle. In addition, plane flow only exists within a small range of θ near the friction angle ϕ_c (or the Angle of Repose). A smaller θ results in “attenuating” flow with a static layer of material existing between the flowing layer and the plane.

5.3.5 Scaling law

The scaling law is well known for the inclined plane experiment, which states that the Froude number (defined as $Fr = v/\sqrt{gh_{std}}$) and the normalized thickness (h_{std}/h_{stop}) form a linear relationship when $h_{std}/h_{stop} > 1$ for any given plane inclination θ or gate opening h_0^0 [125, 121]. This scaling law has been proved by both experiments on glass beads [125, 148, 121] and angular sand [148] as well as simulations [149]. In this chapter, the inclined plane tests with different inclination angles θ and gate openings h_0^0 were simulated, and the results were plotted in Figure 5.7. The gray “◆”s in Figure 5.7(a) denote numerical data predicted from the G-B hypoplastic model while all other symbols stand for results from the DP- $\mu(I)$ model at different plane angles θ . Results obtained from both models agree with each other when θ and h_0^0 are small, i.e., flow is in or close to the quasi-static regime. However, when h_{std}/h_{stop} becomes large (corresponding to a large θ , h_0^0 , and shear rate), a linear relationship is observed from the DP- $\mu(I)$ modeling results while the G-B hypoplastic model predicted a trend with a close to zero slope. This implies that the G-B hypoplastic model is less effective as compared to the rate-dependent DP- $\mu(I)$ model in capturing the dense flow behavior when the shear rate is high.

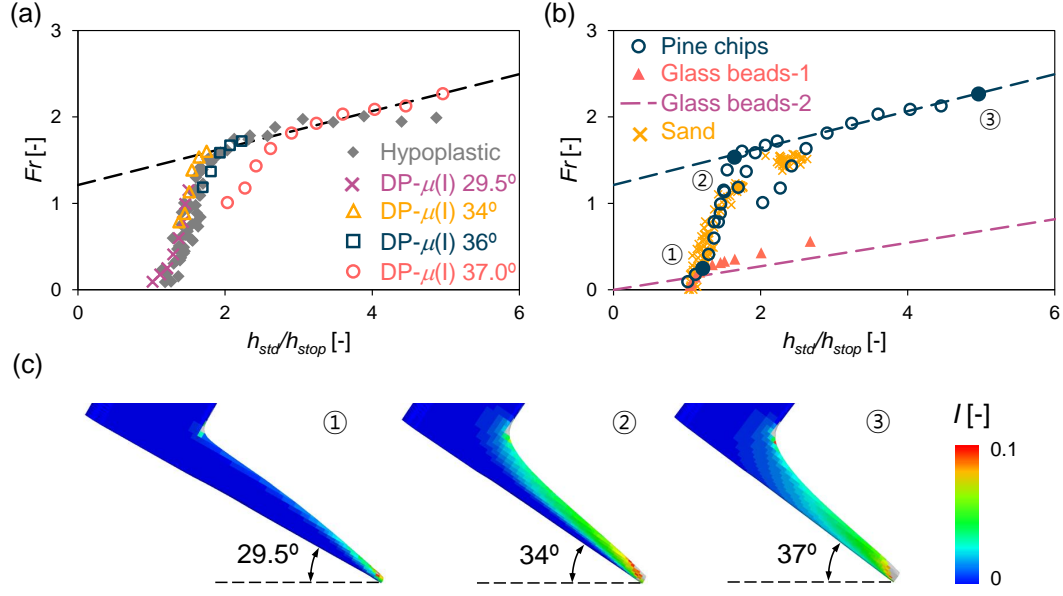


Figure 5.7: Scaling law and inertial number distributions. (a) The Froude number Fr against the normalized thickness h_{std}/h_{stop} of pine chips obtained from the G-B Hypoplastic model and the DP- $\mu(I)$ model with different inclined angles θ . (b) The relation of the Froude number Fr and the normalized thickness h_{std}/h_{stop} for different granular materials: pine chips (this study), angular sand [148], glass beads-1 [148], and glass beads-2 [125]. (c) Inertial number distribution obtained during steady flow from Point ① ($\theta = 29.5^\circ$, $h_0^0 = 0.25$ m), Point ② ($\theta = 34^\circ$, $h_0^0 = 0.35$ m), and Point ③ ($\theta = 37^\circ$, $h_0^0 = 0.35$ m). Note that the 3 points are marked in (b) as “•”s.

Figure 5.7(b) displays the Froude number Fr against the normalized thickness h_{std}/h_{stop} obtained from pine chips (this study), angular sand [148], and glass beads [125, 148]. The first interesting observation is that the slope of pine chips (0.214) is similar to the slope of the glass beads (0.136) reported by Pouliquen [125]. Moreover, all materials start from (1,0) because the steady flow thickness h_{std} is physically larger than h_{stop} . The scaling relations of the pine chips, sand, and glass beads-1 all start from (1,0) and increase with a similar slope until each of them reaches a different turning point for different materials. The scaling relations, then, continues to linearly increase with different slopes. We can observe that the turning point correlates with the internal friction of granular materials: a material with a higher internal friction angle (e.g., pine chips) needs a larger steady flow thickness h_{std} to reach a certain velocity v (i.e., larger Froude number). This is demonstrated by that the glass beads, with the smallest friction angle, has the lowest turning points, while the

pine chips with the largest friction angle among the three has the largest turning point.

The distribution of inertial number from the $DP-\mu(I)$ simulations can be then extracted to determine flow regimes at the limiting points in the scaling law. Figure 5.7(c) presents the magnitude of inertial number I at the beginning of the trend, at the turning point, and at the tail of the trend, which are marked in Figure 5.7(b) with “•”s. At Point ①, the internal number for almost the entire flow region is close to zero, meaning flow is in the quasi-static regime. At Point ②, which is the turning point for pine chips (Figure 5.7(b)), more than half of the material on the plane have an internal number larger than ~ 0.01 , indicating these materials are flowing in the dense regime. At Point ③, most of the materials are in the dense flow regime.

5.3.6 Limitations of $DP-\mu(I)$ model

Although the $DP-\mu(I)$ model performs better than the G-B hypoplastic model in capturing the flow response in dense flow regimes, it has some limitations. As mentioned in subsection 5.3.3, the stopping thickness h_{stop} predicted from different gate openings h_0^0 with the $DP-\mu(I)$ model has nonphysical large variations compared against the experimental and the G-B hypoplastic modeling results. The same reason also results in the simulation results depending on numerical time step size dt . Therefore, in this chapter, all the $DP-\mu(I)$ parameters were calibrated with the same dt and fixed it for all simulations.

Moreover, the parameters (μ_2, I_0) were calibrated separately for each plane inclination θ to accurately match with the experimental results. The μ_2 is fixed for all simulations while I_0 varies for different inclination angles θ (Table 5.2). Figure 5.8(a) plots I_0 , ranging from 0.0003 to 0.008, as a function of θ for $\theta = 29.5^\circ \sim 37^\circ$. Fixed I_0 as 0.0009 was also used and the tests with different θ and h_0^0 were simulated and the results were plotted in Figure 5.8(b,c). The $DP-\mu(I)$ modeling results with a fixed I_0 can still roughly agree with the experimental measurements, but its prediction is not as good as varied I_0 (Figure 5.5). Admittedly, this weakness of the proposed $DP-\mu(I)$ limits its application across all flow

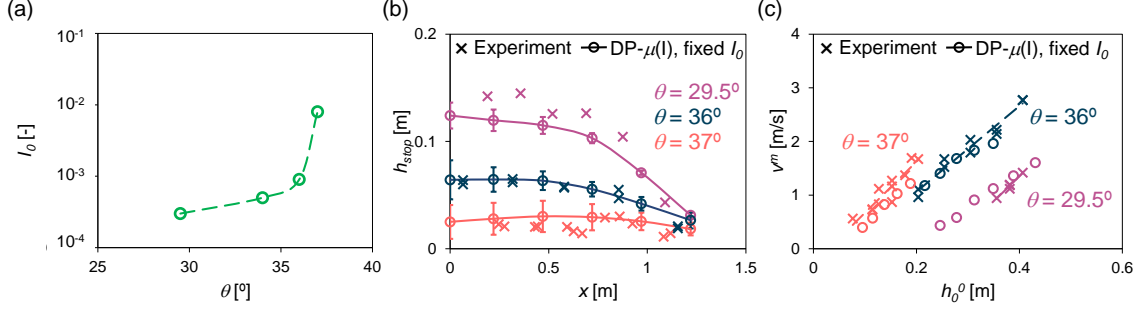


Figure 5.8: Limitations of the DP- $\mu(I)$ model. (a) Material parameter I_0 is a function of θ . (b) Stopping thickness h_{stop} profile along the ramp x predicted from a fixed $I_0 = 9 \times 10^{-4}$. Error bars represent the variation from different gate opening heights h_0^0 . (c) Steady flow velocity at the symmetric surface top v^m with a fixed $I_0 = 9 \times 10^{-4}$. The symbol “x” stands for experimental measurements and “o” represents results from the DP- $\mu(I)$ model with a fixed I_0 .

regimes at different shear rates with a single set of material parameters. However, for most granular flow applications (e.g., hopper flow, screw feeder transfer, landslides), the dominant shear rates are usually within a small range. The DP- $\mu(I)$ model with a well-calibrated set of material parameters for those dominate shear rates can still provide good predictions. The authors are working on improving the proposed model to address this weakness.

5.4 Conclusions

To advance the understanding of the multi-regime flowability of granular biomass materials, this chapter investigated the flow behavior of loblolly pine chips in both quasi-static and dense flow regimes with inclined plane flow tests. The flow behavior, manifested as the stopping thickness h_{stop} , the steady flow thickness h_{std} and the flow velocity v^m , were characterized by experimental measurements and numerical predictions using the classical Gudehus-Bauer hypoplastic model and the Drucker-Prager- $\mu(I)$ model. The formulation, implementation, parameter calibration, and validation of the proposed Drucker-Prager- $\mu(I)$ model were described firstly. The representative flow response was then reported with an in-depth discussion on the flow profile, flow regimes, and the scaling law of pine chips

flowing down an inclined plane. The performance of the two models were compared, and the limitations of the Drucker-Prager- $\mu(I)$ model was discussed. The main conclusions and contributions are summarized:

- The inclined plane flow experiment, complemented with validated numerical modeling, is an effective and robust approach to exploring the multi-regime flow behavior of granular biomass materials.
- For granular materials with a large internal friction angle like pine chips, plane flow only exists within a small range of the plane inclination angle that is close to the internal friction angle. A large inclination results in an accelerated flow while a small inclination results in an attenuating flow (heap flow). For heap flow, the angle between the material top surface and the horizontal surface is about the same as the material angle of repose.
- The scaling law of pine chips between the Froude number and the normalized thickness h_{std}/h_{stop} has a similar slope to the glass beads [125]. The turning point on the scaling curve corresponds to the transition between dense flow and quasi-static dominant flow.
- The DP- $\mu(I)$ model performs better for flow in a dense regime at high shear rates, yet, the G-B hypoplastic model is robust for simulating flow systems in a quasi-static regime and a dense regime with a low shear rate.

This study is the first-in-its-kind to explore the multi-regime flow behavior of granular biomass materials, which provides valuable data for future studies and validations. Future research will focus on improving the DP- $\mu(I)$ model to robustly capture wide flow regimes.

CHAPTER 6

EFFECTS OF MOISTURE CONTENT ON FLOW BEHAVIOR

6.1 Introduction

As reviewed in section 5.1, lots of experimental characterizations were conducted to understand the flow behavior of particulate biomass materials over the decades. Most of these studies focused on dry or room-moisture biomass particles. However, biorefineries often have to process wet materials with the water originated from the original plants as well as outdoor transport and storage. Wet biomass materials usually have worse flowability than dry particles. Understanding the effects of moisture content on the flow behavior of milled biomass is critical to evaluating bioenergy material handling in real situations.

Current studies on the influence of moisture content on biomass flowability can be grouped into three categories: 1) macro-scale flow and jamming behavior in handling equipment like hoppers [17, 150, 82, 84], silos [151, 152, 153], and screw feeders [154, 155], 2) meso-scale laboratory experiments of the effects of moisture content on material compressibility (including bulk density and elasticity) [156, 157, 158, 159, 160, 82, 17, 18], angle of repose [154, 161, 18, 159], shear responses [162, 158, 82, 18, 17, 84, 159, 160], and wall friction tests, [18, 156, 157, 163], and 3) particle scale characterization including particle size and shape, particle density, and particle stiffness [164, 150, 159, 157]. Most of these analyses tried to correlate the particle scale and meso-scale bulk properties with the macro-scale flow behavior in handling equipment like hoppers following the early framework contributed by Jenike [26]. However, it has been shown in previous chapters that Jenike's framework, though works well for conventional granular materials, often fails on milled biomass because the analysis was based on the Mohr-Coulomb model, which has been shown not capable of characterizing the high compressibility of biomass particles

[32].

In addition, as plant species, milled biomass mostly have pores inside particles and the pore size is often at the magnitude of micrometer [165]. Existence of these micro pores makes the flow of wet biomass particles complicated, where multiple mechanisms may exist simultaneously, e.g., capillary force, water-induced particle deformation, particle aggregates caused by surface tension, water lubrication, etc. Understanding how these mechanisms influence the flow behavior and identifying their dominant ranges of moisture content are greatly needed.

To address this knowledge gap, this chapter investigates the flow behavior of loblolly pine chips influenced by moisture content with multi-scale experiments and numerical simulations. The differential scanning calorimetry test and thermogravimetric analysis were performed to understand the component and the pores inside particles. Min/max density test, oedometer test, and angle of repose test were conducted to investigate the compressibility and the shear behavior at bulk or laboratory scale. Moreover, hopper flow simulations were performed to evaluate the flow behavior at equipment scale. This chapter enhanced the scientific understanding of biomass flowability affected by moisture content.

6.2 Methods

6.2.1 Biomass sample

The milled biomass sample used in this chapter is loblolly pine chips, which has been described in details in subsection 2.3.1 and will be omitted here. Note that the original pine chips were dried in a rotary drum after grinding until the moisture content reached the room moisture content, which is 9.5% (dry basis). During each test, the sample was first oven dried for 24 hours, and then specific amount of water was added to and mixed with the dry particles. The water was added separately to different parts of the dry sample and then mixed to avoid the local difference of moisture content. Note that the moisture content

in this study is defined according to dry basis, i.e.,

$$MC = \frac{m_w}{m_s} \times 100\%, \quad (6.1)$$

where m_w and m_s stand for mass of water and mass of solids, respectively.

6.2.2 Experimental methods and setups

Differential scanning calorimetry

The differential scanning calorimetry (DSC) test was conducted with the TA DSC 250 to determine the fiber saturation point (FSP) of pine chips, which measures the moisture content at which the cell walls are fully saturated with bound water and no free water exists. Water was firstly added to the original pine samples until the moisture content was surely higher than the FSP, which can normally range from 10% to 50% [166]. Then, around 5 mg of the sample was placed in the DSC cell, heated from -20°C until 20°C with a heating rate of 2°C/min. During heating, the time lapse temperature was measured and the time lapse heat flow was calculated by comparing the temperature difference between the sample and a reference.

Thermogravimetric analysis

Thermogravimetric analysis (TGA) was performed using EXSTAR TG/DTA 7300 to understand the components of the pine sample. Around 7 g of the original sample (with room moisture content) was placed in the TGA cell and was heated from room temperature (around 20°C) to 950°C in nitrogen with a heating rate of 20°C/min, and then the sample was kept at 950°C with air for 10 min followed by cooling back to the room temperature. The time lapse weight change was measured, and the rate of weight change was determined by the device.

Min/max density

The density evolution with pressure was determined by the min/max density tests according to the ASTM standards [53, 55]. The minimum density was achieved by the “rainfall” method described in subsection 2.3.2 while the maximum density was obtained by vibrating the sample for 5 min with the W.S.Tyler Ro-tap RX-29 sieve shaker . The maximum density was determined with the pressure ranging from zero to 10 kPa, which covers the pressure range in most of the bioenergy material handling applications [65].

Oedometer test

Continuous density-pressure relationships in samples with various moisture contents were obtained from the oedometer tests. Samples were air pluviated into a 4-inch diameter oedometer cell, which was placed within a load frame with displacement and load measurements. All samples were loaded, unloaded, and reloaded at a rate of 20% strain per hour.

Angle of repose

Angle of repose (AoR) tests with a funnel [167, 168] were conducted for pine chips at different moisture content. Materials flowing out of the funnel deposit on a smooth-surface acrylic plate, forming a conical pile. The AoR was determined through image analysis of the taken photos of the deposited piles. For each moisture content, at least ten tests were repeated.

6.3 Results

6.3.1 Fiber saturation point

The TGA results are presented in Figure 6.1(a), where the orange line represents the mass of the specimen left on the pan with increasing temperature. The dark line is the changing

rate of the mass, the dominant peak of which corresponds to cellulose and hemicellulose whose major decomposition temperature range is $200^{\circ}\text{C} \sim 400^{\circ}\text{C}$ [169]. The decomposition temperature of lignin spans from 150°C to 1000°C . The final small peak stands for mass burned in oxygen-rich gas (air). It can be determined that the pine chips tested in this study consists of 3% inorganic matter, 6% water, 65% cellulose and hemicellulose, and 26% lignin and other matters. The portions of components agree with what reported in literature [169, 170]. The small discrepancy between the moisture content of the original material (6% from TGA and 9.5% from oven drying) is probably caused by the small sample size of TGA (i.e., the diameter of the TGA pan is around 6 mm). The TGA sample only contains fine particles, which may not be representative for the whole sample.

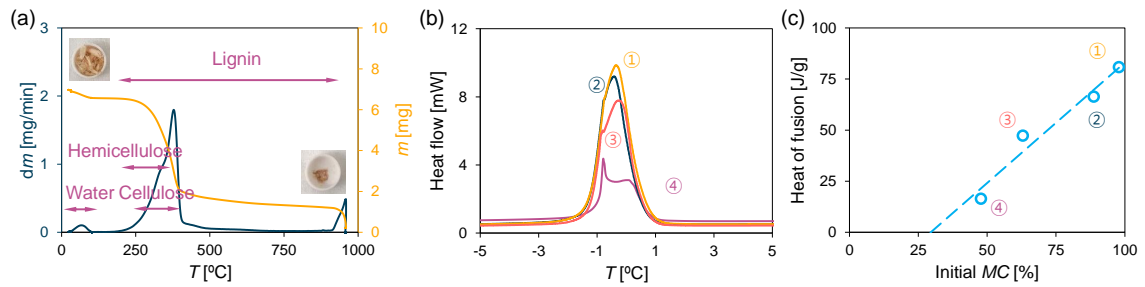


Figure 6.1: Particle characterization results. (a) Results from the Thermogravimetric Analysis (TGA) showing the evolution of mass and its derivative by raising temperature. (b) Results from the Differential Scanning Calorimetry (DSC) tests presenting the heat flow as a function of temperature. (c) Determined Fiber Saturation Point (FSP) by direct calculation from each test with different starting moisture content shown as the horizontal axis. (d) Heat of fusion as a function of initial moisture content computed from the DSC tests.

Presented in Figure 6.1(b) are the results from 4 DSC tests with the starting moisture content from 48% to 98%. The water molecules in biomass particles can be generally categorized into two types: 1) bound water, which are physically adsorbed in cell walls and held by molecular forces at hydroxyl sites of cellulose materials, and 2) free water, which mainly resides in lumen of cells or outside of particles and they can be easily driven off. Since the melting point of ice drops with the increasing pressure, the bound water (ice) are usually hard to freeze (melt) because of the high pressure caused by the small channel size. When raising temperature from -20°C in each test, ice starts melting from molecules

with higher pressure gradually towards those with lower pressure, making the heat flow gradually increase. Since the majority of molecules still have relatively low pressure, the melting and the heat flow reach the maximum when temperature approaches zero, which is the melting point of ice at the atmosphere pressure.

The fiber saturation point (FSP), defined as the moisture content at which the cell walls are saturated with bound water and no free water exists, was determined from DSC results by the extrapolation method [171, 172, 166]: 1) calculating the melting enthalpy ΔH_m of samples with different initial moisture content, 2) plotting the $\Delta H_m - MC_{init}$ data points, 3) extrapolating the line and obtaining the intersect with the MC_{init} axis, which stands for the moisture content at which the $\Delta H_m = 0$, i.e., the FSP. As shown in Figure 6.1(c), the FSP obtained from the extrapolation method is 30%.

6.3.2 Compressibility

The experimental results from min/max density tests and oedometer tests of biomass particles with various moisture content are presented in Figure 6.2. Figure 6.2(a) shows that the minimum density ρ_b^{min} , obtained from the “rainfall” method described in subsection 2.3.2, linearly increase with increase moisture content. The maximum density measured from the vibrating table tests are shown in Figure 6.2(b), where each line stands for the post-vibration density at vertical pressure from zero to 10 kPa for different moisture contents. It can be seen that the bulk density increases with both applied stress and moisture content. In addition, the oedometer results in Figure 6.2(c) show that the sample compressibility increases with increased moisture content.

6.3.3 Static friction

The angle of repose (AoR) tests were conducted by funnel method and the results are presented in Figure 6.3 with a photo demonstrating the measurement of the AoR. The AoR of pine chips at room moisture content is around 44° , which is similar as the internal fric-

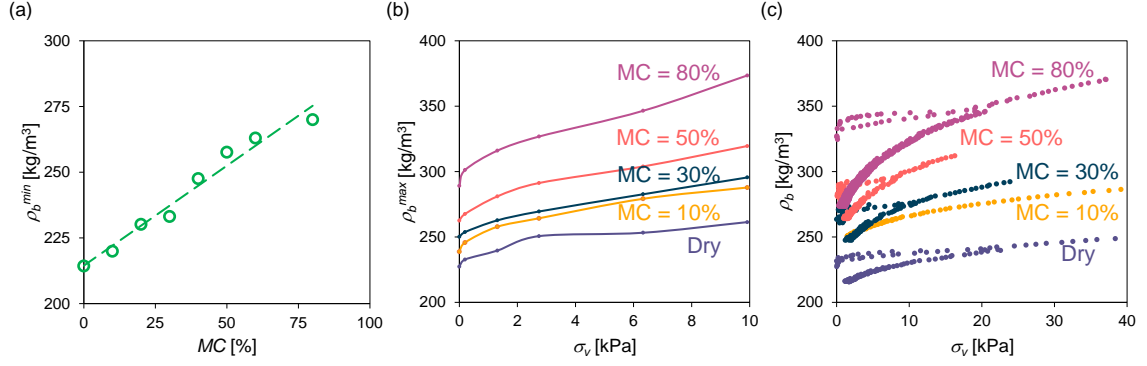


Figure 6.2: Experimental results demonstrating the material compressibility. (a) The minimum density ρ_b^{min} as a function of the moisture content. (b) The maximum density ρ_b^{max} determined after vibration at different surcharge loads and different moisture contents. (c) Bulk density response changing with compressive pressure at different moisture contents determined from oedometer tests.

tion angle 47.3° determined with the combined experimental-numerical method described in chapter 2. Note that small variations may exist due to the variability of biomass materials caused by the origin of the sample, i.e., different tree age, height, and the position and fraction of the tree may result in variations of material properties [88, 50, 49]. The AoR generally increases with higher moisture content, which implies a higher shear (flow) resistance, i.e., worse flowability of biomass particles, at a high moisture content

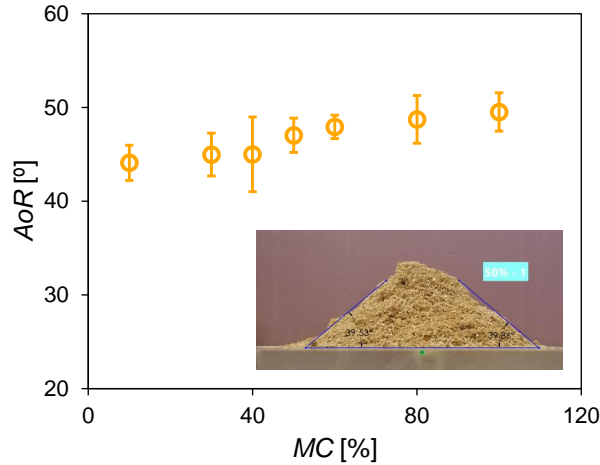


Figure 6.3: Angle of Repose (AoR) determined by funnel method as a function of the moisture content, where each point were averaged from 10 data points and the error bars represent the standard deviation.

6.4 Analyses and discussion

6.4.1 Particle swelling

Figure 6.4(a) shows that the bulk density of biomass samples subjected to a constant stress increases with increasing moisture content. However, the “effective” density, i.e., the packing of the corresponding dry biomass skeleton, decreases with increasing moisture content (Figure 6.2(b)). The effective skeleton density ρ_{sk} is defined as

$$\rho_{sk} = \rho_b \times \frac{1}{1 + MC}, \quad (6.2)$$

which measures the density of particle skeleton alone with the presence of water. The results in Figure 6.4(b) suggest that the biomass particles are compacted denser with moisture loss before the fiber saturation point (FSP = 30%), beyond which moisture content has negligible impacts to skeleton packing. This is mainly because the molecular structures of cellulose and hemicullose materials shrink and additional hydrogen bonds are formed between polymer chains with water loss below FSP. This also suggests that biomass particles swell upon wetting before FSP and the swelling ceases after the cell walls are saturated.

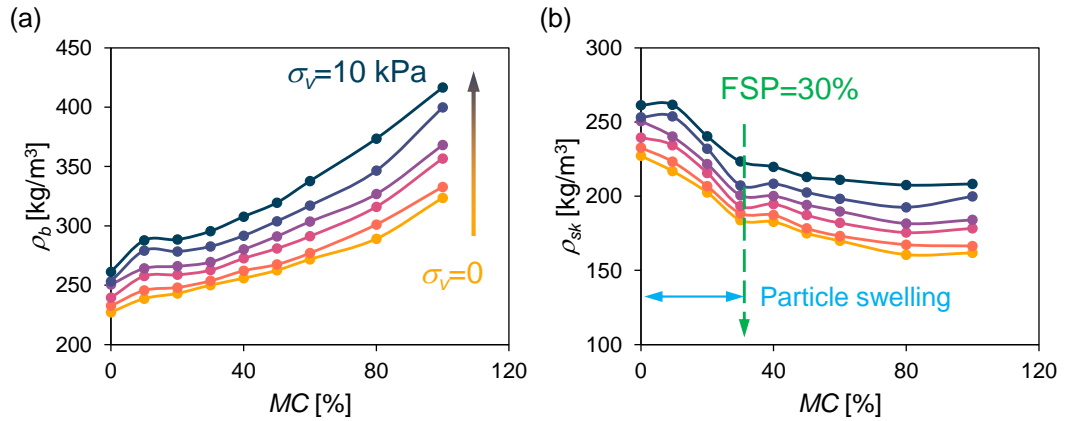


Figure 6.4: (a) The maximum bulk density of samples after vibration at different moisture contents, where the lines form bottom to the top represent compressive pressure from zero to 10 kPa. (b) Particle skeleton density ρ_{sk} , defined as the bulk density of particle skeleton (solids), as a function of the moisture content.

In addition, it is also noticed during the tests that particle aggregation occurred when the moisture content reaches around 40% to 60%. This aggregation of small particles can be attributed to the capillarity when a small amount of free water residing at the inter-particle contacts.

6.4.2 Flow behavior in wedge-shaped hoppers

Numerical modeling

To evaluate the influence of moisture content on the flow behavior at equipment scale, hopper simulations were conducted and the flow rates at different moisture contents were extracted and compared. The Coupled Eulerian Lagrangian (CEL) FEM scheme, which has been described in details in subsection 3.2.3, was used to develop a quasi-3D hopper flow model. Shown in Figure 6.5(a) is the 2D plane-strain slice in simulations to model the 3D hopper flow test. The numerical model is mostly similar as the one developed in subsection 3.2.3 except for the boundary conditions on hopper walls. In this chapter, no-slip boundary was implemented on both hopper walls by directly fixing all 6 degrees of freedom of boundary nodes.

Among various constitutive models on simulating flow behavior of milled biomass [32], the Gudehus-Bauer (G-B) hypoplastic model [45, 46] has been implemented and utilized to explore the physics of biomass granular flow with various successes [65, 88, 89]. Therefore, the G-B model is also used in this chapter to simulate biomass flow behavior with various moisture contents. The hypoplastic model parameters can be divided into three categories: 1) the minimum, critical state, and maximum void ratio at zero pressure e_{d0} , e_{c0} , and e_{i0} , 2) compressibility related parameters h_s , n , and β , and 3) shear related parameters ϕ_c and α . Detailed description and calibration of these parameters as well as the G-B hypoplastic model were reported in chapter 2 and the previous work [65]. In this chapter, the hypoplastic material parameters were calibrated from the min/max density tests, oedometer tests, angle of repose tests, and single element FEM simulations following a similar procedure

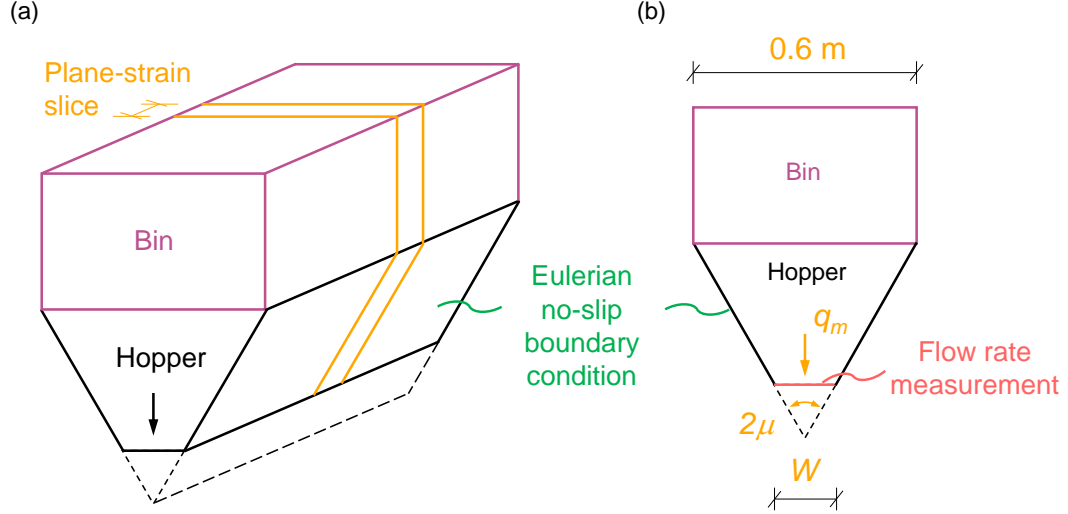


Figure 6.5: Numerical model of the hopper flow test. (a) A 3D wedge-shaped hopper with a cuboid bin above it. The numerical model simulated a plane-strain slice of 0.025 m thickness. (b) The 2D cross section of the model. No-slip boundary condition was applied on both hopper walls by fixing all 6 degrees of freedom of the boundary nodes. The flow rate was measured by extracting the density and flow velocity of the outlet elements and nodes, respectively.

Table 6.1: Calibrated G-B-hypoplastic model parameters of pine chips at different moisture contents.

MC	ρ_p [kg/m ³]	ϕ_c [°]	h_s [kPa]	n [-]	e_{d0} [-]	e_{c0} [-]	e_{i0} [-]	α [-]	β [-]
9.5%	430	44.09	138.6	0.48	0.78	0.95	1.05	0.1	0.5
30%	508.2	44.96	138.6	0.38	0.99	1.14	1.59	0.2	2.0
50%	586.4	47.02	119.7	0.39	1.19	1.32	1.84	0.2	2.0
80%	703.6	48.72	90.1	0.45	1.50	1.59	2.22	0.1	2.0

reported in Lu et. al [65] except that: 1) the critical state friction angle ϕ_c was determined by AoR tests, 2) α , β , and e_{i0} were determined by single-element FEM simulations of the oedometer tests. The calibrated parameters are listed in Table 6.1. A few assumptions were made during the calibration: 1) Particle density ρ_p were estimated by assuming fixed particle volume, and 2) water molecules were considered all filling in particles (i.e., no water exists outside particles). Note that the FSP ($\sim 37.5^\circ$) only measures the amount of bound water, which are trapped in cell walls, and there are still plenty of space inside each particle (bigger channels) that can host more water molecules.

Hopper flow affected by moisture content

Hopper flow simulations were conducted with a fixed hopper geometry (inclination angle $\mu = 45^\circ$, outlet width $W = 60$ mm), the same packing condition (i.e., the initial void ratio $e_{init} = 1/2(e_{d0} + e_{c0})$, which represents a relatively loose packing), and the same initial weight of material M . The results, with respect to both mass flow rate and volume flow rate, are presented in Figure 6.6 and Figure 6.7, respectively.

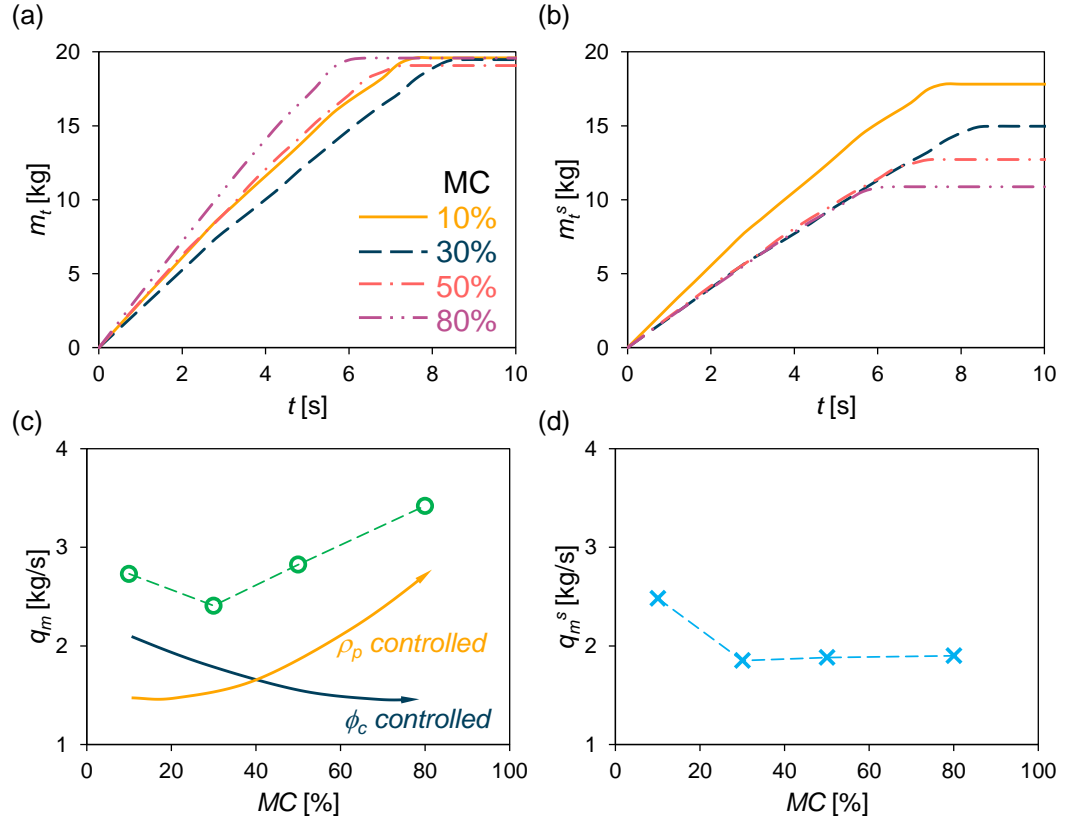


Figure 6.6: Hopper flow response with respect to discharged mass m_t and mass flow rate q_m . (a) Time lapse discharged mass m_t at different moisture contents, where the slope stands for the mass flow rate q_m , q_m is plotted in (c) against moisture content. (b) Effective discharged mass m_t^s , defined as the discharged total mass of solid (with water removed), changing with time. The effective mass flow rate q_m^s is plotted in (d) against moisture content.

Figure 6.6(a) plots the time lapse discharged mass m_t for pine chips with moisture content from 9.5% to 80%, where the slope measures the mass flow rate q_m . The q_m are also plotted as a function of moisture content in Figure 6.6(c). Both Figure 6.6(a,c) indicate

that the mass flow rate first decreases and then increases with a increasing moisture content. The effective discharged mass m_t^s is then defined to evaluate the amount of discharged biomass solids as:

$$m_t^s = m_t \times \frac{1}{1 + MC}. \quad (6.3)$$

The time lapse response of effective discharged mass m_t^s is presented in Figure 6.6(b) with the corresponding effective mass flow rate q_m^s plotted in Figure 6.6(d). With a higher moisture content, the effective mass flow rate decreases until reaching the FSP, after which the effective mass flow rate stays constant.

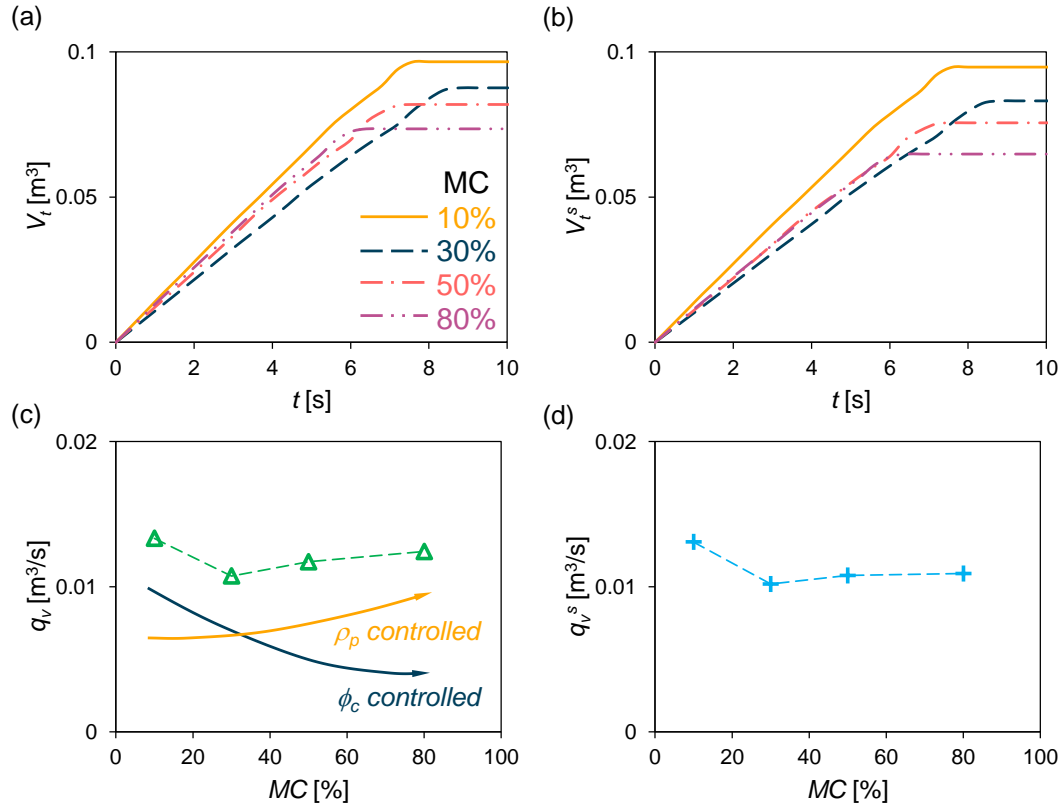


Figure 6.7: Hopper flow response with respect to discharged volume V_t and volumetric flow rate q_v . (a,b) Discharged volume V_t and effective discharged volume V_t^s , defined as the discharged total volume subtracting the volume of water, evolving with time t . (c,d) Volumetric flow rate q_v and effective volumetric flow rate q_v^s changing against moisture content.

Similar trend can be observed on the volumetric flow response in Figure 6.7. Figure 6.7(a,c) present the time lapse discharged volume V_t and the corresponding volumetric

flow rate q_V for different moisture contents. The volumetric flow rate is lower at intermediate moisture content. Figure 6.7(a,c) plot the time lapse effective discharged volume V_t^s , define as

$$V_t^s = V_t - (m_T \times \frac{MC}{1 + MC}) / \rho_w, \quad (6.4)$$

and the corresponding effective volumetric flow rate q_V^s , which describe the discharged volume of biomass solids. It can be found that the effective volumetric flow rate q_V^s also decreases until reaching the FSP and becomes relatively stable after passing FSP.

The physical process of hopper flow is determined by the competence of the discharge driven force, i.e., gravity, against the flow (shear) resistance (chapter 3). With the aforementioned knowledge learned from experiments, it can be inferred that the hopper discharge of wet biomass particles are governed by two competing mechanisms: 1) the growth of moisture content increases the shear (flow) resistance of material, which harms the flow and diminishes the flow rate (shown as the dark arrows in Figure 6.6(c) and Figure 6.7(c)), and 2) adding water into the sample increases the weight, i.e., the discharge driven force, so that facilitates the flow (shown as the orange arrows in Figure 6.6(c) and Figure 6.7(c)). Therefore, efficient hopper discharge can be achieved with a low moisture content while an intermediate moisture content will harm the flow process and should be avoided. With a high moisture content, though high flow rate can be achieved, the effective discharged biomass solids are still slow.

As mentioned in subsection 6.4.1, particle aggregation was observed when mixing biomass particles with water, indicating the existence of cohesion. The G-B hypoplastic model used in this chapter cannot capture the cohesion behavior, which may underestimate the flow resistance with intermediate and high moisture contents. Therefore, the flow rate for wet biomass with intermediate and high moisture content should be lower than what has been predicted here. An advanced constitutive model is in development to capture the flow behavior of wet biomass particles.

6.5 Conclusions

To improve the understanding of the flow behavior of milled biomass influenced by moisture content, particle-level experiments and hopper flow simulations using loblolly pine chips were conducted in this chapter. The key conclusions follow.

- The fiber saturation point of tested loblolly pine chips is 30% using differential scanning calorimetry. The moisture increase before the fiber saturation point ($MC < FSP$) results in particle swelling, which ceases and becomes independent of moisture content after the moisture content exceeds the fiber saturation point.
- Increased moisture content in pine chips also leads to higher particle compressibility and increased angle of repose. Particle aggregation at moisture content of 40%-60% is observed due to capillarity from small amounts of free water residing at particle contacts.
- The flow behavior of wet biomass particles in hoppers is governed by two competing forces with increased moisture content: increased internal friction that suppress the flow and increased bulk density that accelerates the gravity-induced flow. For a given hopper configuration, the total bulk flux of wet pine chips increases with moisture content; however, the net biomass flux, i.e., subtracting the water content from the bulk flow, decreases with increased moisture content, and the major decrease occurs before reaching the fiber saturation point.

CHAPTER 7

CONCLUSIONS AND FUTURE WORK

7.1 Conclusions

This study aims to enhance the scientific understanding of the flow physics of milled biomass materials from particle (micro-) to handling equipment (macro-) scale. The scope of this work includes: physical characterization and modeling of particulate biomass materials, granular flow behavior in wedge-shaped hoppers, flow behavior influenced by moisture content, and multi-regime flow behavior and constitutive modeling. The main conclusions and contributions are summarized as follows.

Physical characterization and modeling

- Comparing with conventional granular materials like sands, the pine chips have high aspect ratio, high angularity, pores inside particles, and considerable particle deformability at particle scale. At bulk scale, biomass samples have high compressibility and high shear resistance. The high shear resistance can be attributed to both the elongated particle shape, which results in a high coordination number of each particle, and the considerable particle deformability, which increases the area of particle contacts during compression.
- Traditional characterization methods suffer from either incomplete stress state measurement (e.g., ring shear tests) or limited strain range to reach the critical state shearing (e.g., triaxial shear tests) for soft granular materials like pine chips. The limitations can be addressed by combining laboratory tests and numerical simulations.
- The advanced FEM scheme (Coupled Eulerian lagrangian) with the G-B hypoplastic model can serve as a valid tool to predict the flow of pine chips in both quasi-static

regime (e.g., axial intruding test) and dense flow regime (e.g., hopper flow test). The discrepancy between experiments and simulations is attributed to the incapability of the G-B hypoplastic model to capture particle deformation. However, such discrepancy does not affect the successful capture of key metrics of the flow because the particle deformation becomes less significant during flow (critical state).

Flow behavior in wedge-shaped hoppers

- The hopper flow pattern of the compressible pine chips is closely related to the initial packing of the material. A loose packing mostly results in a smooth flow while a dense packing often results in surging flow, which harms the discharge and may cause hopper failure.
- Flow patterns like mass flow and funnel flow can be quantified by the Mass Flow Index (MFI) and are governed by the material internal friction angle, hopper inclination, and hopper wall friction. The design recommendation is $MFI > 0.3$, which will result in mass flow.
- Fundamentally, flow or jamming (arching) in a hopper is governed by the competence between the discharge driven force (gravity) and the “arching force” (shear or flow resistance). Therefore, hopper arching is primarily determined by the hopper inclination angle and the material-wall friction. A slender hopper, where gravity is converted more to the driven force, makes it easier to initiate the flow. However, a shallow hopper, where gravity is transferred more to wall pressure and then to wall friction, is more susceptible to arching.
- Surcharge influences the flow performance with two competing mechanisms: 1) flow facilitation by adding the discharge driven force with a larger weight, and 2) flow impedance by compaction of material. The mass flow rate of pine chips is primarily dominated by the compaction mechanism, so the mass flow rate decreases when

adding surcharge. The critical outlet width is controlled by both mechanisms depending on the hopper inclination angle.

- For a flat-bottom hopper (i.e., silo), wall friction becomes insignificant comparing with material internal friction because the material tends to shear against itself instead of against the wall near the boundary shear bands. A dense packing and a larger surcharge weight will also harm the flow for a flat-bottom hopper.
- The mass flow rate of woody biomass materials can be determined by a few material properties (particle density, mean particle size, and internal friction angle) and the geometry of the hopper (outlet length and width, and hopper inclination). A robust throughput prediction is provided as Equation 4.5.

Flow behavior affected by moisture content

- The compressibility and shear resistance of pine chips both increase with a higher moisture content, which contributes to the handling difficulties observed on wet biomass materials.
- When moisture content increases from the dry sample, particle swelling occurs with majority of swell happens before reaching the fiber saturation point, which is caused by water molecules gradually filling into cell walls.
- The flow behavior of wet biomass particles is governed by two competing mechanisms: 1) flowability decrease caused by the increase of moisture content which increases the shear resistance, and 2) flow facilitation because of the increase of the weight and the discharge driven force. Dry samples are still preferred for smooth hopper flow.

Multi-regime flow behavior and constitutive modeling

- For granular flow on an inclined plane with a highly shear-resistant material like pine chips, the plane flow only exists within a small range of plane inclination angle which is close to the material internal friction angle. A larger inclination causes accelerated flow while a small inclination results in attenuated flow (or heap flow). In heap flow, the angle between the material top surface and the horizontal direction is around the material angle of repose.
- The scaling law of pine chips with respect to the Froude number against normalized thickness forms a similar slope as glass beads. The turning point of the scaling curve is governed by the transition between dense flow and quasi-static dominant flow.
- The $DP-\mu(I)$ model has a better performance than G-B hypoplastic model on simulating dense granular flow with a high shear rate. However, the G-B hypoplastic model is more robust on modeling flow in quasi-static regime and in dense flow regime with a low shear rate.

7.2 Future work

This study can be improved by addressing some limitations of the numerical modeling and adding additional experimental investigations. The future work is summarized as follows:

- The current numerical model considers biomass materials with different moisture contents as different materials (with different sets of parameters), which is not straightforward for practical use. Future study will aim to develop a more advanced constitutive model that can capture the effects of moisture content.
- Physical experiment has identified that materials with different moisture contents result in different critical arching outlet widths. However, the current numerical model

cannot capture the effects of material attributes on the arching in hoppers. Future work needs to improve the numerical model to account for this.

- Creeping behavior is important to understand the “time effects” on hopper flow and arching. The current model needs to be improved to account for the creeping behavior for related applications. Moreover, the effects of creeping on K_0 of biomass samples and the flow behavior need to be experimentally evaluated.
- The boundary effects between hopper walls and the material, including the wall friction for different materials and at different shear rates, need to be investigated.
- Capillary force plays an important role in the granular flow of wet biomass materials. Experimental studies need to be conducted to find how and to what extent the capillary pressure influences the flow of wet biomass particles.
- When biomass materials with high moisture content are loaded in a hopper, the moisture content of the upper and the lower part of particles will be different and the moisture content distribution will evolve with time. The flow behavior with layered materials (with different moisture contents) needs to be studied.

REFERENCES

- [1] T. W. Crowther *et al.*, “Mapping tree density at a global scale,” *Nature*, vol. 525, no. 7568, pp. 201–205, 2015.
- [2] M. H. Langholtz, B. J. Stokes, and L. M. Eaton, “2016 billion-ton report: Advancing domestic resources for a thriving bioeconomy, volume 1: Economic availability of feedstock,” *U.S. Department of Energy, Oak Ridge National Laboratory, Oak Ridge, TN*, pp. 1–411, 2016.
- [3] “Monthly energy review april 2020,” Energy Information Administration, Office of Energy Statistics, U.S. Department of Energy, Washington, DC., Tech. Rep.
- [4] “Biorefinery optimization workshop summary report,” Bioenergy Technologies Office, Office of Energy Efficiency and Renewable Energy, U.S. Department of Energy, Tech. Rep., 2016.
- [5] J. Dai, S. Sokhansanj, J. R. Grace, X. Bi, C. J. Lim, and S. Melin, “Overview and some issues related to co-firing biomass and coal,” *The Canadian Journal of Chemical Engineering*, vol. 86, no. 3, pp. 367–386, 2008.
- [6] J. Falk, R. J. Berry, M. Broström, and S. H. Larsson, “Mass flow and variability in screw feeding of biomass powders—relations to particle and bulk properties,” *Powder technology*, vol. 276, pp. 80–88, 2015.
- [7] F. Miccio, D. Barletta, and M. Poletto, “Flow properties and arching behavior of biomass particulate solids,” *Powder technology*, vol. 235, pp. 312–321, 2013.
- [8] J. R. Hess, C. T. Wright, and K. L. Kenney, “Cellulosic biomass feedstocks and logistics for ethanol production,” *Biofuels, Bioproducts and Biorefining: Innovation for a sustainable economy*, vol. 1, no. 3, pp. 181–190, 2007.
- [9] D. Ilic, K. Williams, R. Farnish, E. Webb, and G. Liu, “On the challenges facing the handling of solid biomass feedstocks,” *Biofuels, Bioproducts and Biorefining*, vol. 12, no. 2, pp. 187–202, 2018.
- [10] B. Dale, “A sober view of the difficulties in scaling cellulosic biofuels,” *Biofuels, Bioproducts and Biorefining*, vol. 11, no. 1, pp. 5–7, 2017.
- [11] Á. Ramírez-Gómez, “Research needs on biomass characterization to prevent handling problems and hazards in industry,” *Particulate Science and Technology*, vol. 34, no. 4, pp. 432–441, 2016.

- [12] W. Jin, J. Klinger, T. Westover, and H. Huang, "A density dependent drucker-prager/cap model for ring shear simulation of ground loblolly pine," *Powder Technology*, vol. 368, pp. 45–58, 2020.
- [13] T. L. Westover, M. Phanphanich, and J. C. Ryan, "Comprehensive rheological characterization of chopped and ground switchgrass," *Biofuels*, vol. 6, no. 5-6, pp. 249–260, 2015.
- [14] M. Vaezi, V. Pandey, A. Kumar, and S. Bhattacharyya, "Lignocellulosic biomass particle shape and size distribution analysis using digital image processing for pipeline hydro-transportation," *Biosystems engineering*, vol. 114, no. 2, pp. 97–112, 2013.
- [15] Q. Guo, X. Chen, and H. Liu, "Experimental research on shape and size distribution of biomass particle," *Fuel*, vol. 94, pp. 551–555, 2012.
- [16] M. Gil, E. Teruel, and I. Arauzo, "Analysis of standard sieving method for milled biomass through image processing. effects of particle shape and size for poplar and corn stover," *Fuel*, vol. 116, pp. 328–340, 2014.
- [17] S. Hernandez, T. L. Westover, A. C. Matthews, J. C. B. Ryan, and C. L. Williams, "Feeding properties and behavior of hammer-and knife-milled pine," *Powder technology*, vol. 320, pp. 191–201, 2017.
- [18] M. Wu, D. Schott, and G. Lodewijks, "Physical properties of solid biomass," *Biomass and Bioenergy*, vol. 35, no. 5, pp. 2093–2105, 2011.
- [19] N. Chevanan, A. R. Womac, V. S. Bitra, D. C. Yoder, and S. Sokhansanj, "Flowability parameters for chopped switchgrass, wheat straw and corn stover," *Powder Technology*, vol. 193, no. 1, pp. 79–86, 2009.
- [20] N. Gasteyer, H. Yi, V. Puri, C. Wassgren, and M. Gonzalez, "The calibration of dem input parameters for biomass using a cubical triaxial tester," in *2019 AIChE Annual Meeting*, AIChE, 2019.
- [21] H. Yi, V. M. Puri, C. J. Lanning, and J. H. Dooley, "Computational modeling of continuum scale constitutive equations to improve biomass feedstock material handling and conveying systems," in *2019 ASABE Annual International Meeting*, American Society of Agricultural and Biological Engineers, 2019, p. 1.
- [22] C. J. Lanning, H. Yi, J. H. Dooley, V. M. Puri, and J. M. Whitt, "Design of a biomass scale cubical triaxial tester," in *2020 ASABE Annual International Virtual Meeting*, American Society of Agricultural and Biological Engineers, 2020, p. 1.

- [23] H. Salehi, M. Poletto, D. Barletta, and S. H. Larsson, "Predicting the silo discharge behavior of wood chips-a choice of method," *Biomass and bioenergy*, vol. 120, pp. 211–218, 2019.
- [24] D. Barletta, R. J. Berry, S. H. Larsson, T. A. Lestander, M. Poletto, and Á. Ramirez-Gómez, "Assessment on bulk solids best practice techniques for flow characterization and storage/handling equipment design for biomass materials of different classes," *Fuel Processing Technology*, vol. 138, pp. 540–554, 2015.
- [25] H. Rezaei, C. J. Lim, A. Lau, and S. Sokhansanj, "Size, shape and flow characterization of ground wood chip and ground wood pellet particles," *Powder Technology*, vol. 301, pp. 737–746, 2016.
- [26] A. W. Jenike, *Storage and flow of solids*. Bulletin of the University of Utah, 1964, vol. 53.
- [27] D. Barletta and M. Poletto, "An assessment on silo design procedures for granular woody biomass," *Chemical engineering transactions*, vol. 32, pp. 2209–2214, 2013.
- [28] Y. Xia, J. J. Stickel, W. Jin, and J. Klinger, "A review of computational models for the flow of milled biomass part i: Discrete-particle models," *ACS Sustainable Chemistry & Engineering*, vol. 8, no. 16, pp. 6142–6156, 2020.
- [29] Y. Xia, Z. Lai, T. Westover, J. Klinger, H. Huang, and Q. Chen, "Discrete element modeling of deformable pinewood chips in cyclic loading test," *Powder technology*, vol. 345, pp. 1–14, 2019.
- [30] J. Horabik and M. Molenda, "Parameters and contact models for dem simulations of agricultural granular materials: A review," *Biosystems Engineering*, vol. 147, pp. 206–225, 2016.
- [31] Y. Bommireddy, A. Agarwal, V. Yettella, V. Tomar, and M. Gonzalez, "Loading-unloading contact law for micro-crystalline cellulose particles under large deformations," *Mechanics Research Communications*, vol. 99, pp. 22–31, 2019.
- [32] W. Jin, J. J. Stickel, Y. Xia, and J. Klinger, "A review of computational models for the flow of milled biomass part ii: Continuum-mechanics models," *ACS Sustainable Chemistry & Engineering*, vol. 8, no. 16, pp. 6157–6172, 2020.
- [33] Y. Wang, Y. Lu, and J. Y. Ooi, "A numerical study of wall pressure and granular flow in a flat-bottomed silo," *Powder Technology*, vol. 282, pp. 43–54, 2015.

- [34] K. Pardikar and C. Wassgren, “Predicting the critical outlet width of a hopper using a continuum finite element method model,” *Powder Technology*, vol. 356, pp. 649–660, 2019.
- [35] Q. Zheng, B. Xia, R. Pan, and A. Yu, “Prediction of mass discharge rate in conical hoppers using elastoplastic model,” *Powder Technology*, vol. 307, pp. 63–72, 2017.
- [36] K. Pardikar, S. Zahid, and C. Wassgren, “Quantitative comparison of experimental and mohr-coulomb finite element method simulation flow characteristics from quasi two-dimensional flat-bottomed bins,” *Powder Technology*, 2020.
- [37] T. Tian, J. Su, J. Zhan, S. Geng, G. Xu, and X. Liu, “Discrete and continuum modeling of granular flow in silo discharge,” *Particuology*, vol. 36, pp. 127–138, 2018.
- [38] E. J. Fern and K. Soga, “The role of constitutive models in mpm simulations of granular column collapses,” *Acta Geotechnica*, vol. 11, no. 3, pp. 659–678, 2016.
- [39] C. Peng, X. Guo, W. Wu, and Y. Wang, “Unified modelling of granular media with smoothed particle hydrodynamics,” *Acta Geotechnica*, vol. 11, no. 6, pp. 1231–1247, 2016.
- [40] M. Wójcik and J. Tejchman, “Modeling of shear localization during confined granular flow in silos within non-local hypoplasticity,” *Powder Technology*, vol. 192, no. 3, pp. 298–310, 2009.
- [41] J. Tejchman, *Confined granular flow in silos: experimental and numerical investigations*. Springer Science & Business Media, 2013.
- [42] J. Tejchman and J. Górski, “Modeling of bearing capacity of footings on sand within stochastic micro-polar hypoplasticity,” *International Journal for Numerical and Analytical Methods in Geomechanics*, vol. 35, no. 2, pp. 226–243, 2011.
- [43] G. Qiu, S. Henke, and J. Grabe, “Application of a coupled eulerian–lagrangian approach on geomechanical problems involving large deformations,” *Computers and Geotechnics*, vol. 38, no. 1, pp. 30–39, 2011.
- [44] G. Qiu and J. Grabe, “Numerical investigation of bearing capacity due to spudcan penetration in sand overlying clay,” *Canadian Geotechnical Journal*, vol. 49, no. 12, pp. 1393–1407, 2012.
- [45] G. Gudehus, “A comprehensive constitutive equation for granular materials,” *Soils and foundations*, vol. 36, no. 1, pp. 1–12, 1996.
- [46] E. Bauer, “Calibration of a comprehensive hypoplastic model for granular materials,” *Soils and foundations*, vol. 36, no. 1, pp. 13–26, 1996.

- [47] A. Schofield and P. Wroth, *Critical state soil mechanics*. McGraw-Hill London, 1968, vol. 310.
- [48] I. Herle and G. Gudehus, “Determination of parameters of a hypoplastic constitutive model from properties of grain assemblies,” *Mechanics of Cohesive-frictional Materials: An International Journal on Experiments, Modelling and Computation of Materials and Structures*, vol. 4, no. 5, pp. 461–486, 1999.
- [49] R. P. Schultz, *Loblolly pine: the ecology and culture of the loblolly pine (Pinus taeda L.)* US Government Printing Office, 1997.
- [50] L. Jordan, A. Clark, L. R. Schimleck, D. B. Hall, and R. F. Daniels, “Regional variation in wood specific gravity of planted loblolly pine in the united states,” *Canadian journal of forest research*, vol. 38, no. 4, pp. 698–710, 2008.
- [51] A. Clark and J. R. Saucier, “Influence of initial planting density, geographic location, and species on juvenile wood formation in southern pine.,” *Forest Products Journal*, vol. 39, pp. 42–48, 1989.
- [52] C. R. Mora, H. L. Allen, R. F. Daniels, and A. Clark, “Modeling corewood–outerwood transition in loblolly pine using wood specific gravity,” *Canadian journal of forest research*, vol. 37, no. 6, pp. 999–1011, 2007.
- [53] “Astm standard d4253-16, standard test methods for maximum index density and unit weight of soils using a vibratory table,” ASTM International, West Conshohocken, PA, 2016, www.astm.org, Tech. Rep.
- [54] M. F. Riemer, R. B. Seed, P. G. Nicholson, and H.-L. Jong, “Steady state testing of loose sands: Limiting minimum density,” *Journal of Geotechnical engineering*, vol. 116, no. 2, pp. 332–337, 1990.
- [55] “Astm standard d4254-16, standard test methods for minimum index density and unit weight of soils and calculation of relative density,” ASTM International, West Conshohocken, PA, 2016, www.astm.org, Tech. Rep.
- [56] “Astm standard d6773-16, standard test method for bulk solids using schulze ring shear tester,” ASTM International, West Conshohocken, PA, 2016, www.astm.org, Tech. Rep.
- [57] M. Jefferies and D. Shuttle, “On the operating critical friction ratio in general stress states,” *Géotechnique*, vol. 61, no. 8, pp. 709–713, 2011.
- [58] M. Jefferies and K. Been, *Soil liquefaction: a critical state approach*. CRC press, 2015.

- [59] T. Youd, “Factors controlling maximum and minimum densities of sands,” in *Evaluation of relative density and its role in geotechnical projects involving cohesionless soils*, vol. 523, ASTM International, 1973, pp. 98–112.
- [60] C. S. Campbell, “Stress-controlled elastic granular shear flows,” *Journal of Fluid Mechanics*, vol. 539, pp. 273–297, 2005.
- [61] C. S. Campbell, “Granular material flows—an overview,” *Powder Technology*, vol. 162, no. 3, pp. 208–229, 2006.
- [62] J. Johanson, “The johanson indicizer [tm] system vs. the jenike shear tester,” *Bulk Solids Handling*, vol. 12, pp. 237–237, 1992.
- [63] Z. Cheng *et al.*, “Flow behavior characterization of biomass feedstocks,” *Powder Technology*, vol. 387, pp. 156–180, 2021.
- [64] J. H. Leal *et al.*, “Impacts of inorganic material (total ash) on surface energy, wettability, and cohesion of corn stover,” *ACS Sustainable Chemistry & Engineering*, vol. 8, no. 4, pp. 2061–2072, 2020.
- [65] Y. Lu, W. Jin, J. Klinger, T. L. Westover, and S. Dai, “Flow characterization of compressible biomass particles using multiscale experiments and a hypoplastic model,” *Powder Technology*, vol. 383, pp. 396–409, 2021.
- [66] A. W. Jenike, *Gravity flow of bulk solids*. Bulletin of the University of Utah, 1961, vol. 52.
- [67] G. Mehos, M. Eggleston, S. Grenier, C. Malanga, G. Shrestha, and T. Trautman, “Designing hoppers, bins, and silos for reliable flow,” *The Best of Equipment Series*, p. 33, 2018.
- [68] D. Walker, “A basis for bunker design,” *Powder Technology*, vol. 1, no. 4, pp. 228–236, 1967.
- [69] G. Enstad, “On the theory of arching in mass flow hoppers,” *Chemical Engineering Science*, vol. 30, no. 10, pp. 1273–1283, 1975.
- [70] A. Drescher, A. Waters, and C. Rhoades, “Arching in hoppers: Ii. arching theories and critical outlet size,” *Powder Technology*, vol. 84, no. 2, pp. 177–183, 1995.
- [71] J. Guo, A. W. Roberts, and J.-D. Prigge, “Experimental investigation of wall pressure and arching behavior under surcharge pressure in mass-flow hoppers,” *Powder technology*, vol. 258, pp. 272–284, 2014.

- [72] S. V. Sjøgaard *et al.*, “An experimental evaluation of powder flow predictions in small-scale process equipment based on Jenike’s hopper design methodology,” *Powder Technology*, vol. 321, pp. 523–532, 2017.
- [73] J. Xue, S. Schiano, W. Zhong, L. Chen, and C.-Y. Wu, “Determination of the flow/no-flow transition from a flat bottom hopper,” *Powder Technology*, vol. 358, pp. 55–61, 2019.
- [74] J. Li, P. A. Langston, C. Webb, and T. Dyakowski, “Flow of sphero-disc particles in rectangular hoppers—a DEM and experimental comparison in 3D,” *Chemical Engineering Science*, vol. 59, no. 24, pp. 5917–5929, 2004.
- [75] Y. Zhao, R. A. Cocco, S. Yang, and J. W. Chew, “DEM study on the effect of particle-size distribution on jamming in a 3D conical hopper,” *AIChE Journal*, vol. 65, no. 2, pp. 512–519, 2019.
- [76] Y. Xia *et al.*, “Assessment of a tomography-informed polyhedral discrete element modelling approach for complex-shaped granular woody biomass in stress consolidation,” *Biosystems Engineering*, vol. 205, pp. 187–211, 2021.
- [77] Y. Wang, Y. Lu, and J. Y. Ooi, “Finite element modelling of wall pressures in a cylindrical silo with conical hopper using an arbitrary Lagrangian–Eulerian formulation,” *Powder Technology*, vol. 257, pp. 181–190, 2014.
- [78] Q. Zheng and A. Yu, “Finite element investigation of the flow and stress patterns in conical hopper during discharge,” *Chemical Engineering Science*, vol. 129, pp. 49–57, 2015.
- [79] D. Cornforth, “Prediction of drained strength of sands from relative density measurements,” in *Evaluation of relative density and its role in geotechnical projects involving cohesionless soils*, ASTM International, 1973.
- [80] A. E. Ray *et al.*, “Multiscale characterization of lignocellulosic biomass variability and its implications to preprocessing and conversion: A case study for corn stover,” *ACS Sustainable Chemistry & Engineering*, vol. 8, no. 8, pp. 3218–3230, 2020.
- [81] K. L. Kenney, W. A. Smith, G. L. Gresham, and T. L. Westover, “Understanding biomass feedstock variability,” *Biofuels*, vol. 4, no. 1, pp. 111–127, 2013.
- [82] N. Saha, C. Goates, S. Hernandez, W. Jin, T. Westover, and J. Klinger, “Characterization of particle size and moisture content effects on mechanical and feeding behavior of milled corn (*Zea mays* L.) stover,” *Powder Technology*, p. 117 535, 2022.

- [83] A. Hamed, Y. Xia, N. Saha, J. Klinger, D. N. Lanning, and J. Dooley, “Flowability of crumbler rotary shear size-reduced granular biomass: An experiment-informed modeling study on the angle of repose,” *Frontiers in Energy Research*, p. 319, 2022.
- [84] J. Klinger *et al.*, “Multiscale shear properties and flow performance of milled woody biomass,” *Frontiers in Energy Research*, vol. 10, 2022.
- [85] H. Yi, C. J. Lanning, J. C. Slosson, M. J. Wamsley, V. M. Puri, and J. H. Dooley, “Determination of fundamental mechanical properties of biomass using the cubical triaxial tester to model biomass flow,” *Biofuels*, pp. 1–12, 2022.
- [86] E. A. Fakhrabadi, J. J. Stickel, and M. W. Liberatore, “Frictional contacts between individual woody biomass particles under wet and dry conditions,” *Powder Technology*, vol. 408, p. 117 719, 2022.
- [87] J. Pachón-Morales, J. Colin, F. Pierre, F. Puel, and P. Perré, “Effect of torrefaction intensity on the flow properties of lignocellulosic biomass powders,” *Biomass and Bioenergy*, vol. 120, pp. 301–312, 2019.
- [88] Y. Lu, W. Jin, J. Klinger, and S. Dai, “Flow and arching of biomass particles in wedge-shaped hoppers,” *ACS Sustainable Chemistry & Engineering*, vol. 9, no. 45, pp. 15 303–15 314, 2021.
- [89] W. Jin *et al.*, “On the Fidelity of Computational Models for the Flow of Milled Loblolly Pine: A Benchmark Study on Continuum-Mechanics Models and Discrete-Particle Models,” *Frontiers in Energy Research*, vol. 10, 2022.
- [90] D. Bertuola, S. Volpato, P. Canu, and A. C. Santomaso, “Prediction of segregation in funnel and mass flow discharge,” *Chemical Engineering Science*, vol. 150, pp. 16–25, 2016.
- [91] J. Johanson, “The placement of inserts to correct flow in bins,” *Powder Technology*, vol. 1, no. 6, pp. 328–333, 1968.
- [92] M. Wójcik, J. Härtl, J. Y. Ooi, M. Rotter, S. Ding, and G. G. Enstad, “Experimental investigation of the flow pattern and wall pressure distribution in a silo with a double-cone insert,” *Particle & Particle Systems Characterization*, vol. 24, no. 4-5, pp. 296–303, 2007.
- [93] J. Haertl, J. Y. Ooi, J. Rotter, M. Wójcik, S. Ding, and G. G. Enstad, “The influence of a cone-in-cone insert on flow pattern and wall pressure in a full-scale silo,” *Chemical engineering research and design*, vol. 86, no. 4, pp. 370–378, 2008.
- [94] S. Volpato, R. Artoni, and A. C. Santomaso, “Numerical study on the behavior of funnel flow silos with and without inserts through a continuum hydrodynamic

- approach,” *Chemical Engineering Research and Design*, vol. 92, no. 2, pp. 256–263, 2014.
- [95] A. W. Jenike, “A theory of flow of particulate solids in converging and diverging channels based on a conical yield function,” *Powder technology*, vol. 50, no. 3, pp. 229–236, 1987.
 - [96] A. Drescher, “On the criteria for mass flow in hoppers,” *Powder Technology*, vol. 73, no. 3, pp. 251–260, 1992.
 - [97] N. P. Kruijt, “Results of Jenike’s (1987) radial stress field theory for the flow of granular materials in conical hoppers: Flow regimes and flow factors,” *Powder technology*, vol. 76, no. 1, pp. 109–112, 1993.
 - [98] D. Walker, “An approximate theory for pressures and arching in hoppers,” *Chemical Engineering Science*, vol. 21, no. 11, pp. 975–997, 1966.
 - [99] J. Walters, “A theoretical analysis of stresses in axially-symmetric hoppers and bunkers,” *Chemical Engineering Science*, vol. 28, no. 3, pp. 779–789, 1973.
 - [100] G. Enstad, “A note on the stresses and dome formation in axially symmetric mass flow hoppers,” *Chemical Engineering Science*, vol. 32, no. 3, pp. 337–339, 1977.
 - [101] W. A. Beverloo, H. A. Leniger, and J. Van de Velde, “The flow of granular solids through orifices,” *Chemical engineering science*, vol. 15, no. 3-4, pp. 260–269, 1961.
 - [102] R. M. Nedderman *et al.*, *Statics and kinematics of granular materials*. Cambridge University Press Cambridge, 1992, vol. 352, pp. 301–306.
 - [103] D. Schulze, *Powders and bulk solids, 2nd edition*. Springer, 2021, vol. 22, pp. 435–437.
 - [104] H. Rose and T. Tanaka, “Rate of discharge of granular materials from bins and hoppers,” *The Engineer*, vol. 208, pp. 465–469, 1959.
 - [105] J. Brown and J. Richards, *Principles of Powder Mechanics (1970)*. Oxford: Pergamon, pp. 160–166.
 - [106] K. Kaza and R. Jackson, “The rate of discharge of coarse granular material from a wedge-shaped mass flow hopper,” *Powder Technology*, vol. 33, no. 2, pp. 223–237, 1982.

- [107] S. B. Savage and M. Sayed, “Gravity flow of coarse cohesionless granular materials in conical hoppers,” *Zeitschrift für angewandte Mathematik und Physik ZAMP*, vol. 32, no. 2, pp. 125–143, 1981.
- [108] J. Davidson, “The hourglass theory of hopper flow,” *Trans. Instn Chem. Engrs*, vol. 51, pp. 29–35, 1973.
- [109] B. Sharma, R. G. Ingalls, C. L. Jones, and A. Khanchi, “Biomass supply chain design and analysis: Basis, overview, modeling, challenges, and future,” *Renewable and Sustainable Energy Reviews*, vol. 24, pp. 608–627, 2013.
- [110] I. Dafnomilis, R. Hoefnagels, Y. W. Pratama, D. L. Schott, G. Lodewijks, and M. Junginger, “Review of solid and liquid biofuel demand and supply in northwest europe towards 2030—a comparison of national and regional projections,” *Renewable and Sustainable Energy Reviews*, vol. 78, pp. 31–45, 2017.
- [111] J. Yan *et al.*, “Characterizing variability in lignocellulosic biomass: A review,” *ACS Sustainable Chemistry & Engineering*, vol. 8, no. 22, pp. 8059–8085, 2020.
- [112] C. Li, P. Kerner, C. L. Williams, A. Hoover, and A. E. Ray, “Characterization and localization of dynamic cell wall structure and inorganic species variability in harvested and stored corn stover fractions as functions of biological degradation,” *ACS Sustainable Chemistry & Engineering*, vol. 8, no. 18, pp. 6924–6934, 2020.
- [113] Y. Guo, Q. Chen, Y. Xia, T. Westover, S. Eksioglu, and M. Roni, “Discrete element modeling of switchgrass particles under compression and rotational shear,” *Biomass and Bioenergy*, vol. 141, p. 105 649, 2020.
- [114] F. Chen, Y. Xia, J. L. Klinger, and Q. Chen, “A set of hysteretic nonlinear contact models for dem: Theory, formulation, and application for lignocellulosic biomass,” *Powder Technology*, vol. 399, p. 117 100, 2022.
- [115] Y. Guo, Q. Chen, Y. Xia, J. Klinger, and V. Thompson, “A nonlinear elasto-plastic bond model for the discrete element modeling of woody biomass particles,” *Powder Technology*, vol. 385, pp. 557–571, 2021.
- [116] J. W. Carson, “Preventing particle segregation: A review of the primary causes and some practical solutions can help,” *Chemical Engineering*, vol. 111, no. 2, pp. 29–32, 2004.
- [117] P. Tang and V. Puri, “Methods for minimizing segregation: A review,” *Particulate Science and Technology*, vol. 22, no. 4, pp. 321–337, 2004.

- [118] W. R. Ketterhagen, J. S. Curtis, C. R. Wassgren, and B. C. Hancock, “Predicting the flow mode from hoppers using the discrete element method,” *Powder technology*, vol. 195, no. 1, pp. 1–10, 2009.
- [119] T. Nguyen, C. Brennen, and R. Sabersky, “Funnel flow in hoppers,” *Journal of Applied Mechanics*, vol. 47, no. 4, pp. 729–735, 1980.
- [120] G. I. Tardos, S. McNamara, and I. Talu, “Slow and intermediate flow of a frictional bulk powder in the couette geometry,” *Powder Technology*, vol. 131, no. 1, pp. 23–39, 2003.
- [121] G. M. gdrmidi@ polytech. univ-mrs. fr <http://www.lmgc.univ-montp2.fr/MIDI/>, “On dense granular flows,” *The European Physical Journal E*, vol. 14, pp. 341–365, 2004.
- [122] K. Tannous, P. Lam, S. Sokhansanj, and J. Grace, “Physical properties for flow characterization of ground biomass from douglas fir wood,” *Particulate Science and Technology*, vol. 31, no. 3, pp. 291–300, 2013.
- [123] J. Dai and J. R. Grace, “A model for biomass screw feeding,” *Powder Technology*, vol. 186, no. 1, pp. 40–55, 2008.
- [124] J. Dai and J. R. Grace, “Biomass granular screw feeding: An experimental investigation,” *Biomass and Bioenergy*, vol. 35, no. 2, pp. 942–955, 2011.
- [125] O. Pouliquen, “Scaling laws in granular flows down rough inclined planes,” *Physics of fluids*, vol. 11, no. 3, pp. 542–548, 1999.
- [126] M. Tirapelle, L. Troncon, S. Volpato, and A. C. Santomaso, “Size segregation of ternary mixtures in inclined chute flows: An experimental study,” *Chemical Engineering Transactions*, vol. 86, pp. 823–828, 2021.
- [127] R. Artoni and A. Santomaso, “Effective wall slip in chutes and channels: Experiments and discrete element simulations,” *Granular Matter*, vol. 16, no. 3, pp. 377–382, 2014.
- [128] M. Cavinato, R. Artoni, M. Bresciani, P. Canu, and A. C. Santomaso, “Scale-up effects on flow patterns in the high shear mixing of cohesive powders,” *Chemical Engineering Science*, vol. 102, pp. 1–9, 2013.
- [129] O. Pouliquen, “On the shape of granular fronts down rough inclined planes,” *Physics of fluids*, vol. 11, no. 7, pp. 1956–1958, 1999.
- [130] Y. Forterre and O. Pouliquen, “Long-surface-wave instability in dense granular flows,” *Journal of Fluid Mechanics*, vol. 486, pp. 21–50, 2003.

- [131] P. Jop, Y. Forterre, and O. Pouliquen, “Crucial role of sidewalls in granular surface flows: Consequences for the rheology,” *Journal of Fluid Mechanics*, vol. 541, pp. 167–192, 2005.
- [132] Y. Forterre and O. Pouliquen, “Flows of dense granular media,” *Annual Review of Fluid Mechanics*, vol. 40, no. 1, pp. 1–24, 2008.
- [133] S. B. Savage, “Gravity flow of cohesionless granular materials in chutes and channels,” *Journal of Fluid Mechanics*, vol. 92, no. 1, pp. 53–96, 1979.
- [134] S. Savage and M. Sayed, “Stresses developed by dry cohesionless granular materials sheared in an annular shear cell,” *Journal of Fluid Mechanics*, vol. 142, pp. 391–430, 1984.
- [135] D. M. Hanes and D. L. Inman, “Observations of rapidly flowing granular-fluid materials,” *Journal of Fluid Mechanics*, vol. 150, pp. 357–380, 1985.
- [136] H. Yi, V. M. Puri, C. J. Lanning, and J. H. Dooley, “Finite element modeling of biomass hopper flow,” in *2020 ASABE Annual International Virtual Meeting*, American Society of Agricultural and Biological Engineers, 2020, p. 1.
- [137] P. Jop, Y. Forterre, and O. Pouliquen, “A constitutive law for dense granular flows,” *Nature*, vol. 441, no. 7094, pp. 727–730, 2006.
- [138] K. Kamrin and D. L. Henann, “Nonlocal modeling of granular flows down inclines,” *Soft matter*, vol. 11, no. 1, pp. 179–185, 2015.
- [139] D. L. Henann and K. Kamrin, “A predictive, size-dependent continuum model for dense granular flows,” *Proceedings of the National Academy of Sciences*, vol. 110, no. 17, pp. 6730–6735, 2013.
- [140] Z. Tang, T. A. Brzinski, M. Shearer, and K. E. Daniels, “Nonlocal rheology of dense granular flow in annular shear experiments,” *Soft matter*, vol. 14, no. 16, pp. 3040–3048, 2018.
- [141] M. Bouzid, M. Trulsson, P. Claudin, E. Clément, and B. Andreotti, “Nonlocal rheology of granular flows across yield conditions,” *Physical review letters*, vol. 111, no. 23, p. 238 301, 2013.
- [142] L. Staron, P.-Y. Lagrée, and S. Popinet, “Continuum simulation of the discharge of the granular silo,” *The European Physical Journal E*, vol. 37, no. 1, pp. 1–12, 2014.
- [143] L. Gesenhues, J. J. Camata, A. M. Côrtes, F. A. Rochinha, and A. L. Coutinho, “Finite element simulation of complex dense granular flows using a well-posed

- regularization of the μ (i)-rheology,” *Computers & Fluids*, vol. 188, pp. 102–113, 2019.
- [144] S. Dunatunga and K. Kamrin, “Continuum modelling and simulation of granular flows through their many phases,” *Journal of Fluid Mechanics*, vol. 779, pp. 483–513, 2015.
 - [145] S. Dunatunga and K. Kamrin, “Modelling silo clogging with non-local granular rheology,” *Journal of Fluid Mechanics*, vol. 940, 2022.
 - [146] J. D. Goddard, “Continuum modeling of granular media,” *Applied Mechanics Reviews*, vol. 66, no. 5, 2014.
 - [147] R. I. Borja and J. E. Andrade, “Critical state plasticity. part vi: Meso-scale finite element simulation of strain localization in discrete granular materials,” *Computer Methods in Applied Mechanics and Engineering*, vol. 195, no. 37-40, pp. 5115–5140, 2006.
 - [148] P. Rognon, “Ecoulements granulaires sur plan incliné: Étude expérimentale de la transition vers l’arrêt,” *Rapport de maîtrise, Université de Marne la Vallée*, 2002.
 - [149] M. Prochnow, “Ecoulements denses de grains secs,” Ph.D. dissertation, Ecole des Ponts ParisTech, 2002.
 - [150] S. Paulrud, J. E. Mattsson, and C. Nilsson, “Particle and handling characteristics of wood fuel powder: Effects of different mills,” *Fuel processing technology*, vol. 76, no. 1, pp. 23–39, 2002.
 - [151] J. E. Mattsson and P. D. Kofman, “Method and apparatus for measuring the tendency of solid biofuels to bridge over openings,” *Biomass and bioenergy*, vol. 22, no. 3, pp. 179–185, 2002.
 - [152] J. E. Mattsson and P. D. Kofman, “Influence of particle size and moisture content on tendency to bridge in biofuels made from willow shoots,” *Biomass and bioenergy*, vol. 24, no. 6, pp. 429–435, 2003.
 - [153] P. D. Jensen, J. E. Mattsson, P. D. Kofman, and A. Klausner, “Tendency of wood fuels from whole trees, logging residues and roundwood to bridge over openings,” *Biomass and bioenergy*, vol. 26, no. 2, pp. 107–113, 2004.
 - [154] Z. Miao, T. E. Grift, A. C. Hansen, and K. Ting, “Flow performance of ground biomass in a commercial auger,” *Powder technology*, vol. 267, pp. 354–361, 2014.

- [155] H. Zareiforush, M. H. Komarizadeh, M. R. Alizadeh, and M. Masoomi, "Screw conveyors power and throughput analysis during horizontal handling of paddy grains," *Journal of Agricultural science*, vol. 2, no. 2, p. 147, 2010.
- [156] N. C. Crawford, N. Nagle, D. A. Sievers, and J. J. Stickel, "The effects of physical and chemical preprocessing on the flowability of corn stover," *Biomass and Bioenergy*, vol. 85, pp. 126–134, 2016.
- [157] S. Mani, L. G. Tabil, S. Sokhansanj, and M. Roberge, "Mechanical properties of corn stover grind," in *2003 ASAE Annual Meeting*, American Society of Agricultural and Biological Engineers, 2003, p. 1.
- [158] M. Stasiak *et al.*, "Mechanical characteristics of pine biomass of different sizes and shapes," *European Journal of Wood and Wood Products*, pp. 1–16, 2019.
- [159] B. Littlefield, O. Fasina, J. Shaw, S. Adhikari, and B. Via, "Physical and flow properties of pecan shells—particle size and moisture effects," *Powder technology*, vol. 212, no. 1, pp. 173–180, 2011.
- [160] M. Stasiak, M. Molenda, M. Bańda, and E. Gondek, "Mechanical properties of sawdust and woodchips," *Fuel*, vol. 159, pp. 900–908, 2015.
- [161] K. Ileleji and B. Zhou, "The angle of repose of bulk corn stover particles," *Powder technology*, vol. 187, no. 2, pp. 110–118, 2008.
- [162] M. Stasiak, M. Molenda, M. Gancarz, J. Wiacek, P. Parafiniuk, and A. Lisowski, "Characterization of shear behaviour in consolidated granular biomass," *Powder Technology*, vol. 327, pp. 120–127, 2018.
- [163] S. H. Larsson, "Kinematic wall friction properties of reed canary grass powder at high and low normal stresses," *Powder Technology*, vol. 198, no. 1, pp. 108–113, 2010.
- [164] M. Gil, D. Schott, I. Arauzo, and E. Teruel, "Handling behavior of two milled biomass: Srf poplar and corn stover," *Fuel Processing Technology*, vol. 112, pp. 76–85, 2013.
- [165] P. N. Ciesielski *et al.*, "Biomass particle models with realistic morphology and resolved microstructure for simulations of intraparticle transport phenomena," *Energy & Fuels*, vol. 29, no. 1, pp. 242–254, 2015.
- [166] L. Passarini, S. L. Zelinka, S. V. Glass, and C. G. Hunt, "Effect of weight percent gain and experimental method on fiber saturation point of acetylated wood determined by differential scanning calorimetry," *Wood Science and Technology*, vol. 51, no. 6, pp. 1291–1305, 2017.

- [167] “Astm standard c1444-00, standard test method for measuring the angle of repose of free-flowing mold powders,” ASTM International, West Conshohocken, PA, 2022, www.astm.org, Tech. Rep.
- [168] P. C. Rousé, “Comparison of methods for the measurement of the angle of repose of granular materials,” *Geotechnical Testing Journal*, vol. 37, no. 1, pp. 164–168, 2014.
- [169] D. Díez, A. Urueña, R. Piñero, A. Barrio, and T. Tamminen, “Determination of hemicellulose, cellulose, and lignin content in different types of biomasses by thermogravimetric analysis and pseudocomponent kinetic model (tga-pkm method),” *Processes*, vol. 8, no. 9, p. 1048, 2020.
- [170] J. Cai *et al.*, “Review of physicochemical properties and analytical characterization of lignocellulosic biomass,” *Renewable and sustainable energy reviews*, vol. 76, pp. 309–322, 2017.
- [171] L. A. Simpson and A. Barton, “Determination of the fibre saturation point in whole wood using differential scanning calorimetry,” *Wood Science and Technology*, vol. 25, no. 4, pp. 301–308, 1991.
- [172] S. L. Zelinka, M. J. Lambrecht, S. V. Glass, A. C. Wiedenhoeft, and D. J. Yelle, “Examination of water phase transitions in loblolly pine and cell wall components by differential scanning calorimetry,” *Thermochimica acta*, vol. 533, pp. 39–45, 2012.